Dissertation

Submitted to the

Combined Faculty of Mathematics,

Engineering and Natural Sciences

Heidelberg University, Germany

for the degree of

Doctor of Natural Sciences (Dr. rer. nat.)

presented by

Peng Guo

Oral examination: 30. 06. 2023

Advanced Transition Metal-Based Anode Materials and their Composites for Lithium Ion Battery Application

Referee: Prof. Dr. Peter Comba

Referee: Prof. Dr. Rüdiger Klingeler

This thesis was accomplished at the Inorganic Chemistry Department and the Kirchhoff-Institute for Physics of the Ruprecht-Karls-University Heidelberg from January 2019 until April 2023 and was supervised by Prof. Dr. Peter Comba and Prof. Dr. Rüdiger Klingeler.

Publication:

Peng Guo, Lennart Singer, Zhiyong Zhao, Wojciech Kukułka, Finn Sebastian, Ewa Mijowska, Michael Zharnikov, Peter Comba, Rüdiger Klingeler. "*A facile preparation method and proof of cycle-stability of carbon-coated metal oxide and disulfide battery materials*". 2023, Electrochimica Acta.

Acknowledgments

More than four years have passed since I started my studies in Heidelberg. At the end of this unforgettable journey, I would like to give my thanks to all the people who have ever helped me in research and life.

First and foremost, I would like to express my deepest gratitude to my supervisors, Prof. Peter Comba and Prof. Rudiger Klingeler. They not only gave me patient guidance on how to become a qualified researcher but also helped me to solve various problems in my life. I have gained and grown a lot from their supervision. I am also grateful to all members of Prof. Peter Comba's group and Prof. Rudiger Klingeler's group for their generous help. Many thanks to Finn Sebastian, Felix Lulay, Yannis Riedel, and Hinz, Brian for their assistance with my research projects.

I thank Ilse Glass for her kindness in helping me with the XRD measurements and the use of the HF lab. I would like to thank Prof. Ewa Mijowska, Tomasz Kędzierski and Dr. Wojciech Kukułka for their help with the SEM, TEM measurements. I also thank Zhiyong Zhao for his help with XPS measurement and analysis. I would like to thank Prof. Michael Zharnikov for his guidance on the revision of the submitted paper and XPS data analysis. I am grateful to Lennart Singerr for the kind and generous help not only in the study but also in daily life. I would like to thank Ning Yuan, Bowen Dong, and Yuquan Wu for their generous help and company in daily life. I thank Beiping Miao, Chaoyang Zhang, Cuncai Guo, and Xingrong Huang for their help in life. I really enjoyed the leisure time with them. I would like to thank the China Scholarship Council for the generous financial support to undertake my PhD study. Without this grant from my country, I would not have had the opportunity to study here.

At last, I would like to thank my parents, my brother's family, and my girlfriend Meijun Wang for always being there and caring.

Abstract

In this thesis, conversion type anode materials including transition metal oxides (MoO_3, MoO_2, WO_x), disulfides (WS_2) and the insertion reaction-based carbides with MXene-structure (Ti_3C_2, Nb_2C, V_2C), as well as their composites, were investigated as potential anode materials for next-generation lithium ion batteries (LIBs).

MXenes were prepared by an selective etching-based process. When used as anode materials for LIBs, the synthesized MXenes electrodes exhibit excellent cycling stability due to their high electronic conductivity, layered structure as well as good mechanical properties. In order to improve the specific capacity (<300 mAh g^{-1}) of the MXenes, composites based on Nb_2C- and V_2C-MXenes and conversion-based high-capacity anode materials (MoO_2 and MoO_3) were produced. The here presented MoO_3/Nb_2C was synthesized by a ball-milling method and $MoO_2/C/V_2C$ by an electrostatically assisted hydrothermal method. Crucial experimental parameters for the ball-milled MoO_3/Nb_2C (ball-milling time, ball-milling speed, and mass ratio of components) were varied to optimize the morphology and thus the battery performance. The best properties are obtained for MoO_3/Nb_2C composite synthesized with a mass ratio of 1:1 where a capacity of 261 mAh g^{-1} is found after 300 cycles at a current density of 100 mA g^{-1}. The uniquely structured hydrothermally synthesized $MoO_2/C/V_2C$ composites consist of uniformly distributed MoO_2 in the hierarchical V_2C/C structure. When used as anode materials for LIBs, the composites show outstanding cycling stability and superior rate capability with, e.g., 96% capacity retention (605 mAh g^{-1}) at a high current density of 1000 mA g^{-1} after 400 cycles.

Lastly, carbon-coated tungsten oxides based on low-cost carbon sources (CTAB or PVP) were synthesized by a hydrothermal, carbonization process. An additional sulfurization process yielded carbon-coated disulfides. When used as anode materials for LIBs, the CTAB-assisted tungsten oxide carbon composite (c-WO_x/C), tungsten disulfide carbon composite (c-WS_2/C), and mixed-phase (c-WO_x/C-WS_2/C) electrodes show outstanding cycling stability and rate performance compared to pristine ones. Particularly, the c-WS_2/C electrode shows superior long-term cycle stability of 97% retention after 500 cycles at a high current density of 500 mA g^{-1}. Similarly, the PVP-assisted WS_2/C (p-WS_2/C) electrode displays a capacity retention of 80% after 500 cycles. This work, therefore, presents a scalable and low-cost route to prepare carbon-coated tungsten oxide and disulfide for high performance LIBs, which can be extended for the preparation of other carbon-coated metal-based materials.

Zusammenfassung

In der vorliegenden Arbeit wurden konversionsbasierte Anodenmaterialien am Beispiel der Übergangsmetalloxide MoO_3, MoO_2 und WO_x und des Disulfids WS_2 sowie Interkalationsmaterialien mit MXene-Struktur (Ti_3C_2, Nb_2C, V_2C) und deren Komposite als potenzielle Anodenmaterialien für Lithium-Ionen-Batterien (LIBs) der nächsten Generation untersucht.

MXene wurden durch einen selektiven Ätzprozess hergestellt. Bei der Verwendung als Anodenmaterialien für LIBs weisen die synthetisierten MXene-Elektroden aufgrund ihrer hohen elektronischen Leitfähigkeit, ihrer Schichtstruktur sowie ihrer guten mechanischen Eigenschaften eine ausgezeichnete Zyklenstabilität auf. Um die spezifische Kapazität (<300 mAh g^{-1}) der MXene zu verbessern, wurden Komposite auf der Basis von Nb_2C- und V_2C-MXenen und konversionsbasierten Hochkapazitätsanodenmaterialien (MoO_2 und MoO_3) hergestellt. MoO_3/Nb_2C wurde durch ein Kugelmahlverfahren und $MoO_2/C/V_2C$ durch ein elektrostatisch unterstütztes hydrothermales Verfahren synthetisiert. Dabei wurden entscheidende experimentelle Parameter für das kugelgemahlene MoO_3/Nb_2C (Mahldauer, Mahlgeschwindigkeit und Massenverhältnis der Komponenten) variiert, um die Morphologie und damit die elektrochemischen Eigenschaften zu optimieren. Mit einer Kapazität von 261 mAh g^{-1} nach 300 Zyklen bei einer Stromdichte von 100 mA g^{-1} zeigt das Komposit MoO_3/Nb_2C, welches mit einem Massenverhältnis von 1:1 hergestellt wurde, die beste Leistung. Die hydrothermal synthetisierten $MoO_2/C/V_2C$-Komposite besitzen eine besondere Struktur, die sich durch gleichmäßig in der hierarchischen V_2C/C-Struktur verteilte MoO_2-Partikel auszeichnet. Bei Verwendung als Anodenmaterial für LIBs zeigt das $MoO_2/C/V_2C$-Komposit eine hervorragende Zyklenstabilität und Ratenkapazität, z.B. eine verbleibende Kapazität von 96 % (605 mAh g^{-1}) bei einer hohen Stromdichte von 1000 mA g^{-1} nach 400 Zyklen.

Zudem wurden Kohlenstoff-ummantelte Wolframoxide mittels preiswerter Kohlenstoffquellen (CTAB oder PVP) durch einen hydrothermalen Karbonisierungsprozess synthetisiert. Ein zusätzlicher Schwefelungsprozess erlaubt die Umwandlung zu kohlenstoffbeschichteten Disulfiden. Bei der Verwendung als Anodenmaterialien für LIBs zeigen die mit CTAB hergestellten Materialien (Wolframoxid-Kohlenstoffkomposit: c-WO_x/C, Wolframdisulfid-Kohlenstoffkomposit: c-WS_2/C und das gemischtphasige Material c-WO_x/C-WS_2/C) im Vergleich zu den reinen Materialien eine hervorragende Zyklenstabilität und Ratenkapazität. Insbesondere die c-WS_2/C-Elektrode zeigt eine hervorragende Langzeit-Zyklenstabilität von 97 % nach 500 Zyklen bei einer hohen Stromdichte von 500 mA g^{-1}. Die mittels PVP hergestellte WS_2/C-Elektrode (p-WS_2/C) zeigt mit einer erhaltenen Kapazität von 80 % nach 500 Zyklen ebenfalls gute Ergebnisse. Insgesamt stellt die vorliegende Arbeit damit eine skalierbare und kostengünstige Methode zur Herstellung von Kohlenstoff-ummanteltem Wolframoxid und -disulfid für

Hochleistungs-LIBs vor, die auf die Herstellung weiter Kohlenstoff-ummantelter Materialien auf Metallbasis erweitert werden kann.

Table of Contents

1. State of the art

1.1. Introduction

The energy crisis arising from the depletion of fossil fuels such as coal, oil, and natural gas as well as environmental pollution force people to develop clean, renewable energy like solar and wind energy. To effectively use these energies, significant worldwide interest has been raised to have access to appropriate energy storage devices [1-3]. Among them, secondary batteries attracted much attention [4].

Lead acid batteries were first introduced for vehicle applications due to their low cost and high stability [5]. However, low energy density as well as lead pollution limit their further application. Nickel-cadmium (Ni-Cd) batteries used to be popular in mobile devices but serious memory effects result in a rather short service life. In addition, their attraction is diminished by the toxicity of cadmium [6]. The nickel-metal hydride (Ni-MH) batteries although have low-temperature performance, however, the high cost for the precious metal as catalyst makes them of little use [7]. By comparison, lithium ion batteries (LIBs) are more promising energy storage devices. Since the development of lithium ion batteries, more and more interest has been placed on them due to their low memory effect, high energy density, high working voltage, and environmental friendliness [8, 9]. Nowadays, LIBs are used in various fields, especially in portable electronics, electric vehicles (hybrid, plug-in hybrid, or pure EVs), and the smart grid [10, 11].

Although the manufacturing technologies of LIBs is rapidly improved in the last two decades, the pace of energy density increase of LIBs has slowed down due to the approach to the theoretical limits [12]. Therefore, efforts should be taken to find alternative materials for next-generation LIBs. Recently, various battery technology roadmaps have been released from different countries such as China (Made in China 2025), the United States (DOE Battery 500), Europe (BATTERY 2030+), and Japan (NEDO RISING II) [13-16], which reflects the global urgent demands and exploitation determinations for future high energy density rechargeable batteries.

To meet these demands, the development of advanced cathode and anode materials for LIBs is considered the most effective way. In particular, the anode, as an indispensable component of LIBs, plays an important role in the improvement of energy density. Lithium metal was first used as the anode material for commercial LIBs but big problems like dendrites growth during cycling severely hinder its practical application [17]. Instead, Sony company first introduced graphite as the anode material LIB, which successfully realized the commercialization of LIBs [18]. However, the low capacity and poor rate performance of graphite electrodes could not meet the growth demands for high-performance LIBs. Therefore, many endeavors have been made to handle these problems [19-21].

So far, numerous kinds of advanced anode materials have been proposed for LIBs. Some of them, such as silicon; phosphorus; and transition-based materials possess high theoretical capacities but inferior cycling stability and poor rate capability due to their low electronic conductivity and large volume expansion during cycling [22-24]. By contrast, other anode materials such as carbon-based materials could present better structure stability during cycling as well as high electronic conductivity, leading to outstanding rate performance and cyclability, while the specific capacities they could approach are relatively low [25]. Strategies including morphology control, downsizing, and construction of composites are promising to obtain ideal anode materials for next-generation LIBs. In many works, the desired structures like nanowires, nanorods, and core-shell particles which could have high specific areas and short lithium diffusion paths were designed by adjusting the morphology and size of anode materials, resulting in significant improvement in lithium storage performance [26]. Additionally, forming composites of two or more kinds of anode material was also shown to enhance the lithium ion battery performance by combining the advantages of various components [27]. In the composites, materials such as graphene and carbon nanotubes could work as substrates to support other anode materials, which could not only improve the conductivity but also accommodate the volume changes during cycling [28].

The work shown in this thesis focuses on transition metal-based materials including transition metal oxides ($WO_{2.72}$, MoO_3, and MoO_2), transition metal sulfide (WS_2), and transition metal carbides (Ti_3C_2, Nb_2C, and V_2C) for lithium ion battery applications. Moreover, to achieve enhanced lithium storage performance, several useful strategies were developed to prepare composites of these materials.

In the first approach, various kinds of pristine MXenes (Ti_3C_2, Nb_2C, and V_2C) were synthesized and applied to lithium ion batteries. In particular, in order to optimize the synthesis conditions, the most frequently studied MXene (Ti_3C_2) was prepared via two types of etching agents (48wt% HF and LiF+HCl mixture) to compare their purity, morphology, and lithium storage performance. On this basis, as a simple route, the ball-milling method was introduced to prepare MoO_3/Nb_2C MXene composites for the first time. In order to achieve a good combination of two components, various synthesis conditions including ball-milling times, ball-milling speeds, and mass ratios of components were optimized. Consequently, the mass ratio plays the most role in the combination, and the composite with a mass ratio of 1:1 (MoO_3:Nb_2C) shows the MoO_3 microplates are uniformly embedded in the layered structure of Nb_2C. Moreover, the electrode of this composite exhibits two times higher specific capacity and better cyclicality than pristine MoO_3 and Nb_2C electrodes, benefiting from the synergistic effect of the two components that the Nb_2C layered structure could accommodate the volume expansion of MoO_3 and improve the electrical conductivity. This work gives people an easy and effective way to utilize the layered structure of MXenes for improved battery performance.

Secondly, $MoO_2/C/V_2C$ composites were synthesized by an electrostatic interaction-assisted hydrothermal method and an annealing process for the first time. A positively-charge polymer (PDDA) was adopted to stabilize the V_2C dispersion in water and modify it to positively-charged V_2C/PDDA. The molybdenum source was combined with V_2C/PDDA via electrostatic force and converted to MoO_2 during the hydrothermal process. After a one-step annealing process, PDDA was carbonized and converted to amorphous carbon. As a result, $MoO_2/C/V_2C$ composites with the hierarchical structure were successfully prepared in which MoO_2 nanoparticles were uniformly confined in the V_2C/C layered structure. When used as anode materials for lithium ion batteries, the $MoO_2/C/V_2C$ composites exhibited outstanding battery performance including high capacity, excellent long-term cyclability at a high current density of 1 A as well as superior rate capability. These could be ascribed to several reasons. The unique hierarchical structure could not only provide a short lithium diffusion path but also buffer the volume changes of MoO_2 by the confinement effect. The combination of nanoscale MoO_2 and V_2C/C also offers large specific area and high conductivity for sufficient contact between electrode materials and electrolytes and fast charge transfer. Thus, this work provides a way to effectively utilize the layered structure of unexfoliated multilayer MXene for constructing hierarchical composites of MXenes and other anode materials. Furthermore, the prepared composites could exhibit competitive lithium storage performance compared to other reports.

Thirdly, a facile and simple hydrothermal process followed by a carbonization and sulfurization process is prompted to fabricate carbon-coated tungsten oxides and sulfides as well as their mixed phase. Particularly, low-cost carbon sources were used. As a result, these carbon-coated composites present better battery performance including higher specific capacity, better cycling stability, and rate capability than that pristine ones. In addition, the carbon-coated tungsten disulfide electrode exhibits outstanding long-term cycling stability. This work not only provides new insight to researchers about the effective utilization of a simple and low-cost preparation method for carbon-coated composites for high-performance LIBs but also makes the metal oxides and disulfides more accessible to the industry for the next generation LIBs.

1.1.1. Working principle of LIBs

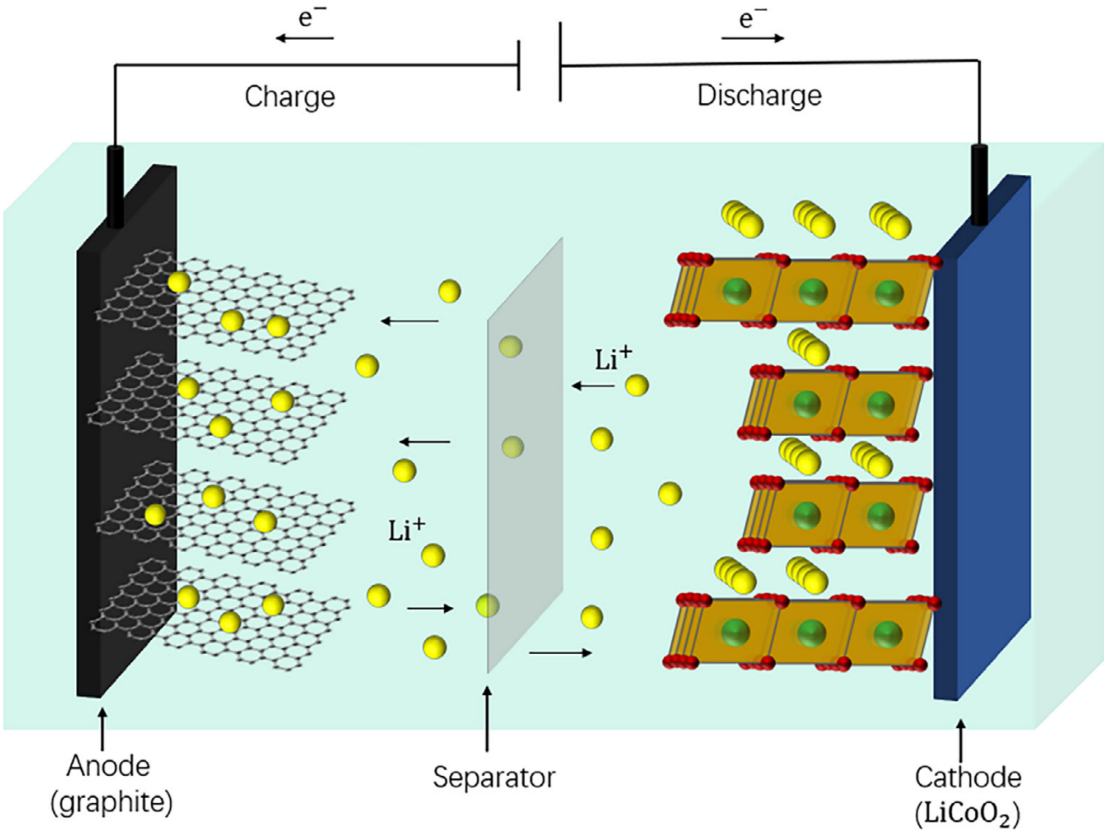

Figure 1. Schematic illustration of the working principle of LIBs. Reproduced with permission from Ref. [7].

As an example, commercial LIB, is introduced here to explain its working principle. Figure 1 shows the schematic illustration of a LIB. For commercial batteries, cathode material (e.g. $LiCoO_2$) and anode material (graphite) are separated by the electrolyte-soaked separator. When the battery is charged, lithium ions are extracted from the cathode material (e.g. $LiCoO_2$) and embedded into the anode material (graphite) after passing through the electrolyte and separator. At the same time, electrons pass from the cathode to the anode through the external circuit to maintain overall neutrality. Lithium ions and electrons flow in the opposite direction when the battery is discharged. The conversion between chemical energy and electric energy is realized in the discharging and charging process. The electrode reaction equations are described as follows [7]:

Cathode $$\mathrm{LiCoO_2 \rightleftharpoons Li_{1-x}CoO_2 + xLi^+ + xe^-} \quad (1)$$

Anode $$\mathrm{6C + xLi^+ \rightleftharpoons Li}_x\mathrm{C_6} \quad (2)$$

Total $$\mathrm{LiCoO_2 + 6C \rightleftharpoons Li_{1-x}CoO_2 + Li_xC_6} \quad (3)$$

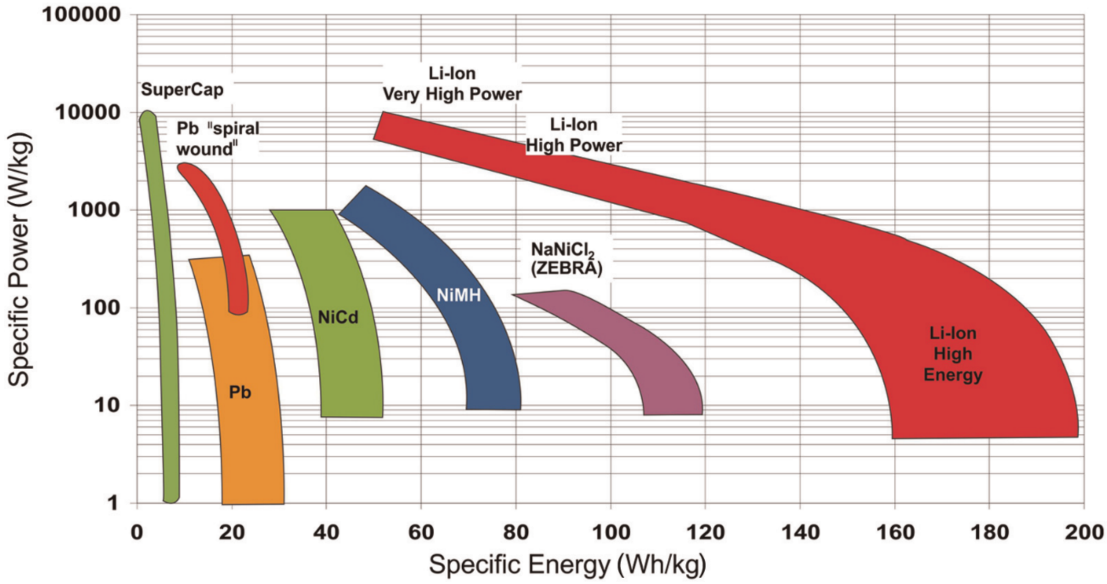

Figure 2. The Ragone plot of various energy storage devices. Here, SuperCap stands for the supercapacitors, Pb stands for the lead acid batteries, Li-ion means the lithium-ion batteries, NiCd stands for the nickel–cadmium batteries, NiMH means the nickel–metal hydride batteries, $NaNiCl_2$ stands for the sodium–nickel chloride batteries, and ZEBRA represents Zero Emission Battery Research Activities. Reproduced with permission from Ref. [29].

For LIBs, certain parameters are used to evaluate the battery performance.

The *Gravimetric power density* (also called the *specific power density*) and the *volumetric power density* refer to the amount of power per mass or volume of batteries with a unit of W/kg or W/L, respectively.

The *Gravimetric energy density* (also called *the specific energy density*) and the *volumetric energy density* are the amount of energy that can be stored or released per mass or volume of batteries with a unit of Wh/kg or Wh/L respectively.

Therefore, power density describes how fast energy is stored or released, while energy density tells the maximum energy that can be stored or released. Figure 2 depicts a Ragone plot (a chart being used to compare the performance of energy storage devices by plotting the specific capacity versus the specific power) of various energy storage devices with specifications at the cell level for automotive applications. Among them, LIBs show the highest energy density and high power density, therefore attracting increasing interest [29].

The *Coulombic efficiency* is the ratio of the discharge capacity to the charge capacity in the same cycle. This can be used for judging the possible occurrence of irreversible reactions, which is the internal consumption of the quantity of electric charge.

The *specific capacity* and *volumetric capacity* are the amounts of electric charge that can be stored or released per mass or per volume of active materials with a unit of mAh g^{-1} or mAh cm^{-3}, respectively.

The *cycle life* generally refers to the cycle number of times that the battery can be charged and discharged with up to 80% of its maximum capacity. For research, the term *cycling performance* can also be used to describe the stability of batteries after specific cycle numbers.

The *rate performance*/*rate capability* describes the ability of electrodes to charge/discharge at various current densities. It is associated with charge/ionic motion in both electrodes and electrolytes [30].

1.1.2. The design of anode materials

Graphite is the most widely used anode material because of its low working potential, low cost, and good cycle life. However, it can only deliver a relatively low theoretical specific capacity of 372 mAh g^{-1}. Moreover, the slow diffusion rate of lithium ions into graphite brings about poor rate performance. Therefore, it is necessary to find alternative anode materials with high capacity and high lithium ion diffusion rate in order to enhance the energy density and power density of the full cell [7].

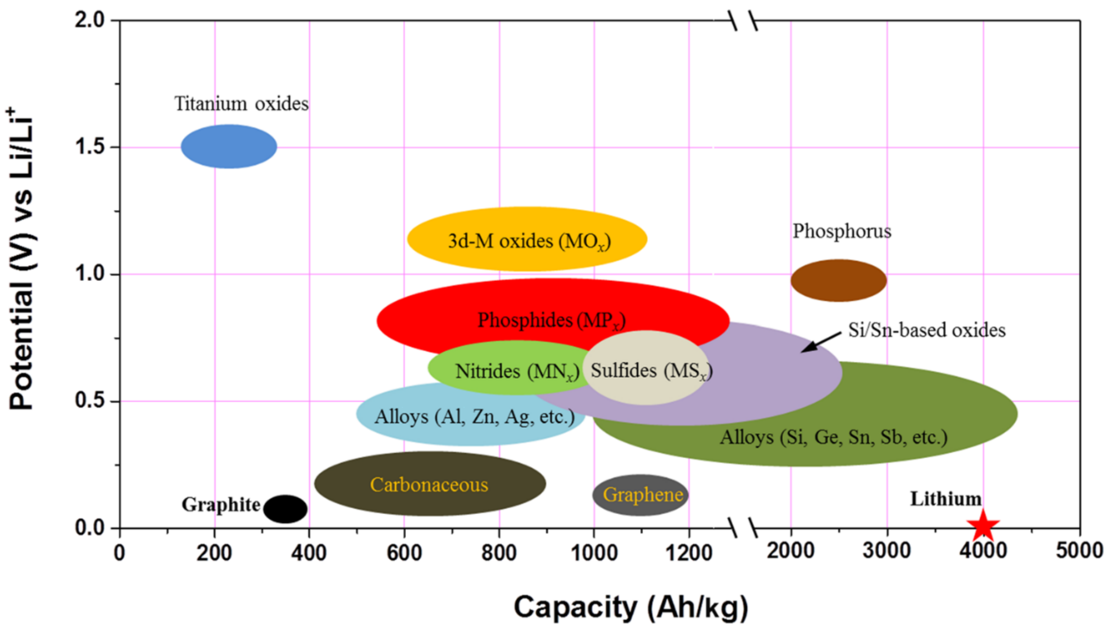

Figure 3. Schematic illustration of working potential (vs. Li/Li^+) of various anode materials and their specific capacities for lithium-ion batteries. Reproduced with permission from Ref. [31].

To design an ideal anode material, some requirements including a low potential against cathode materials, high capacity (gravimetric capacity and volumetric capacity), high rate capability, low cost, long cycle life, and environmental compatibility should be fulfilled. In the last decades, numerous efforts have been devoted to finding suitable anode materials. Carbon materials like carbon nanotubes, carbon nanofiber, graphene, and non-carbon materials like silicon, tin, metal oxides, and metal sulfides have been intensively investigated. Figure 3 shows the redox potential versus Li/Li^+ and the corresponding specific capacity of these materials [31]. As presented in Figure 4, these advanced anode materials can be divided into three categories according to different lithium ion storage mechanisms, i.e., insertion anode materials, alloy anode materials, and conversion anode materials [31].

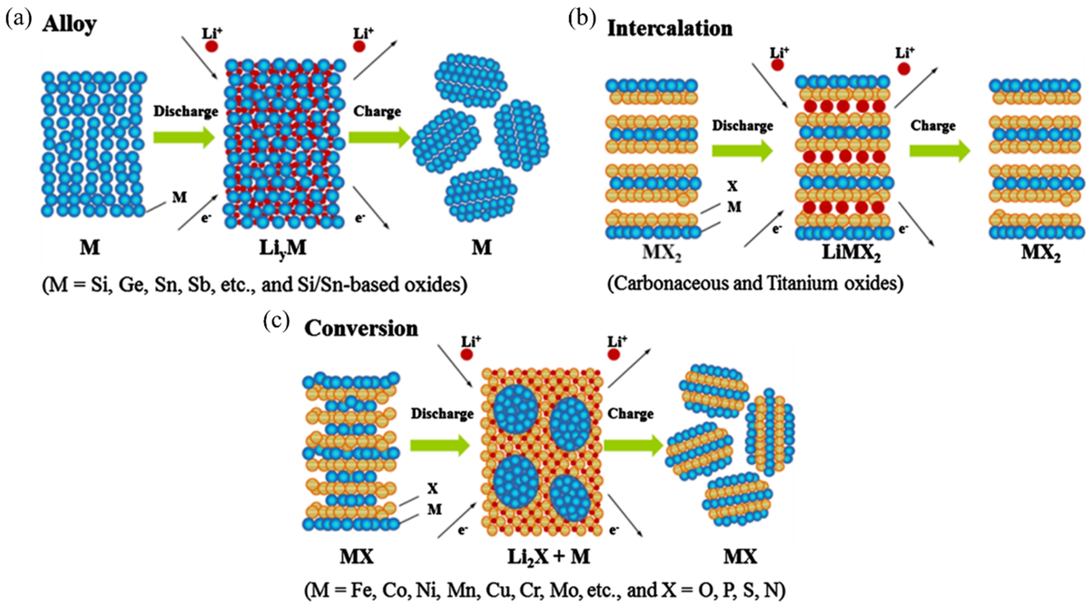

Figure 4. Schematic illustration of lithium storage mechanism of three types of anode materials: alloy anode materials (a), insertion/intercalation anode materials (b), and conversion anode materials (c). Adapted with permission from Ref. [31].

Each type of these proposed anode materials possesses various limitations and advantages when used for LIBs. One can design a suitable anode material by combining some of them to form composites for high lithium storage performance. In the following part, the background and recent progress of insertion anode materials and conversion anode materials, related to the research projects of this thesis, will be introduced.

1.2 Insertion anode materials

The reaction mechanism of the insertion anode materials is that lithium ions intercalate/deintercalate reversibly in anode materials. The commercial anode material graphite and lithium titanate are typical insertion anode materials. Other carbon-based materials like soft carbon, carbon nanotubes, and the new group of layered materials, transition metal carbides and/or nitrides (MXenes) also share this mechanism. The electrodes of insertion anode materials normally exhibit excellent cycling stability due to the comparatively small volume change during lithium intercalation/deintercalation. Moreover, they can also avoid the rupture of solid-electrolyte interphase (SEI) caused by the cracking of the anode material and therefore reduce the consumption of electrolytes and further extend the life of the battery [32]. However, low specific capacities are inevitably achieved due to the limited number of electrons transferred in the redox reactions of insertion materials.

1.2.1. Background and research progress of MXenes for LIBs

In the following, an overview of the background and research progress of MXenes, an insertion anode material relevant to the thesis, in terms of synthesis and lithium ion storage performance is given.

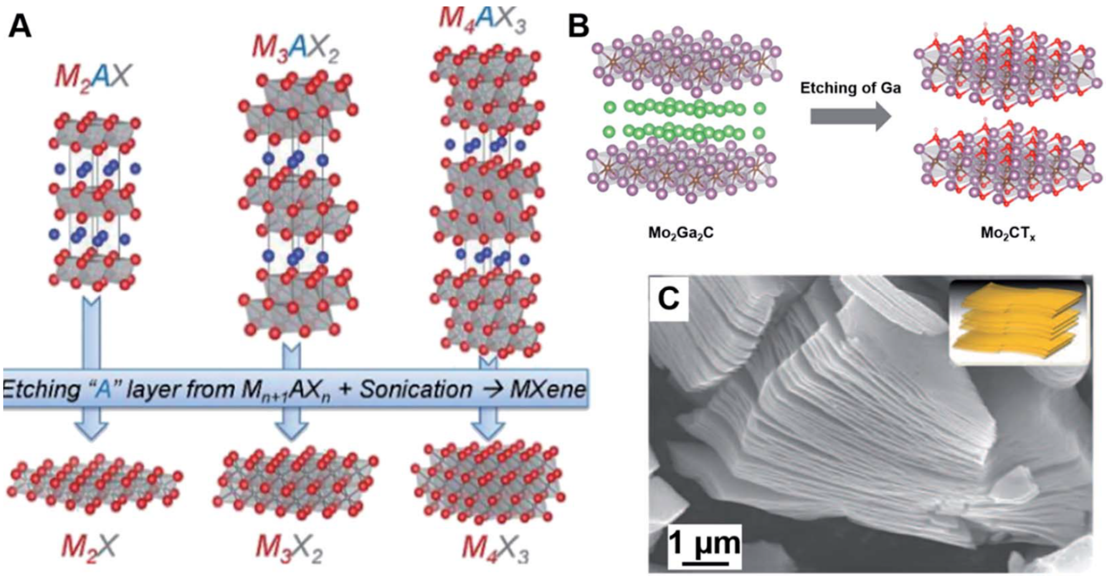

Figure 5. Examples of the current research on MXene-based materials: (a) Schematic illustration of the synthesis of MXenes from the precursors MAXs by the etching process. Reproduced with permission from Ref. [34]. (b) Schematic example of the preparation process of Mo_2CT_x via selective etching of the two Ga layers from Mo_2Ga_2C. Purple, green, brown, red, and white balls stand for Mo, Ga, C, O, and H atoms, respectively. Reproduced with permission from Ref. [35]. (c) The typical accordion-like structure of the $Ti_3C_2T_x$MXene from an SEM image. The inset presents the 2D nature of MXenes. Reproduced with permission from Ref. [36].

Transition metal carbides and/or nitrides (MXenes) are a group of layered materials. The first MXene, Ti_3C_2, was developed by researchers from Drexel University in 2011 [33]. So far, there is a big family with over 30 kinds of MXenes successfully synthesized and more are predicted to exist according to theoretical calculations. Generally, MXenes have the chemical formula of $M_{n+1}X_nT_x$ (n=1-3), where M is a transition metal, X is carbon and/or nitrogen and T_x stands for the surface functional groups (such as F, Cl, OH), which are introduced during the etching process. MXenes are synthesized by selective etching of their precursor MAX which is made of layers of

MXenes that are interleaved with layers of an A element (Where A is Si, Al, or Ga) (Figure 5a-c) [34-36]. Since the M-A bond is metallic, it is impossible to remove A by mechanic force, which is often used to obtain other 2D materials such as graphene and MoS_2. However, the M-A bond is more chemically active than the stronger M-X bond, which makes it possible to selectively remove A layers [37]. Accordingly, two methods are most common to use for the preparation, i.e. the wet chemical method and the bottom-up method.

In the wet chemical synthesis process, an etching agent such as HF (50wt %) is employed. The chemical reactions in this process are listed in equations 4-6 [33]. The type of MXene decides on the different requirements for etching, including etching temperature and etching time. For example, Ti-based MXenes can be obtained from the corresponding MAX phase after being immersed in HF solution for 10-30 h at room temperature, while V-based MXenes require more aggressive conditions (90 h and 90 °C) [38].

The most commonly adopted selective etching and surface functionalization process using HF can be described by the following equations [33]:

$$\mathrm{M_{n+1}AX_n + 3HF \rightarrow AF_3 + \frac{3}{2}H_2 + M_{n+1}X_n} \quad (4)$$

$$\mathrm{M_{n+1}X_n + 2H_2O \rightarrow M_{n+1}X_n(OH)_2 + H_2} \quad (5)$$

$$\mathrm{M_{n+1}X_n + 2HF \rightarrow M_{n+1}X_nF_2 + H_2} \quad (6)$$

Besides, the in-situ formation of HF by mixing hydrochloric acid and alkaline metal fluorides like LiF, or NaF is also an effective and safe way to prepare MXenes. Moreover, the alkaline metal ions could simultaneously intercalate MXene, which causes larger interlayer spacing/enlarged c-lattice constants compared to those of HF-etched MXenes. Few layers or monolayer MXenes can be obtained by a further exfoliation process using sonication or even handshaking [39]. In addition, the organic base tetramethylammonium hydroxide (TMAOH) and alkali base (NaOH) have also been demonstrated to be effective for the synthesis of Ti_3C_2 from Ti_3AlC_2. Geng and coworkers reported that TMAOH can attack Al in Ti_3AlC_2 and lead to the formation of $[Al(OH)_4]^-$. At the same time, TMA^+ can intercalate the synthesized MXene, which facilitates delamination [40]. However, diluted HF is still needed for the removal of the oxidation layer (passivation of $[Al(OH)_4]^-$ and oxidation of Ti_3C_2 to TiO_2) on the MAX phase in this method. Li et al. have developed a fluorine-free method to fabricate Ti_3C_2 [41]. In this route, concentrated NaOH solution (27.5 M NaOH) and high temperature (270°C) were employed to remove the Al layer from Ti_3AlC_2. As a result, Ti_3C_2 with only surface groups of -OH and O was successfully synthesized.

Hence, the wet chemical method provides a versatile way to prepare various kinds of MXene. However, low crystallinity and many defects of the obtained MXenes could hardly satisfy its physical applications. Moreover, the existence of various kinds of surface groups on the prepared MXenes could cause inferior electrochemical performance when used for LIBs.

So far, the bottom-up method has only been used for the preparation of a very limited number of MXenes. In particular, Mo_2C and Mo_2N were produced by chemical vapor deposition, which ensures low defects and a high crystallinity of these MXenes [42, 43].

As a new family of 2D materials, MXenes have attracted considerable attention for LIBs due to high electric conductivity, large specific area, outstanding mechanical properties as well as low lithium diffusion barriers [44, 45]. Naguib et al. reported Ti_2CO_x MXene as an anode material for LIBs for the first time [46]. The Ti_2CO_x MXene electrode exhibited a five times higher reversible capacity than that of the parent Ti_2AlC MAX phase at a current density of 0.1 C. It was concluded that compared with Ti_2AlC MAX, the layered structure and higher surface area of Ti_2CO_x MXene are the main reasons for its higher capacity. Li et al. reported the lithium ion storage of $Ti_3C_2T_x$ [47]. The $Ti_3C_2T_x$ electrode showed initial discharge/charge capacities of 450/250 mAh g^{-1} at 0.1C and a capacity of 119 mAh g^{-1} after 1600 cycles at 5C. It was also found that preparation parameters, functional groups, heating treatment, and chemical oxidation are the main parameters affecting the electrochemical behavior of MXene electrodes. The change in the surface functional groups of MXenes, which was introduced based on synthesis conditions, were found to greatly affect their physical and chemical properties and further result in different lithium ion storage performances. The functional surface groups are mainly Cl, F, O, and OH. The obtained MXenes might have some or all of them according to the used etching agents. However, the performed studies have indicated that the MXenes without surface groups have higher capacity compared with the other terminated [48]. Therefore, several strategies have been used to remove the functional groups of MXenes. For example, Xue et al. prepared fluorine-free Ti_3C_2 MXene by a chemical reactions combined ball-milling method [49]. When used as anode materials, the fluorine-free Ti_3C_2 electrode exhibited a capacity of 310 mAh g^{-1} after 600 cycles at a current density of 100 mA g^{-1}, which is three times higher than that of Ti_3C_2 prepared by HF etching. In addition, altering the surface groups by post-synthesis heat treatments or oxidation methods is also an effective way to improve the electrochemical properties of MXenes. Kong et al. calcined $Ti_3C_2T_x$ at different temperatures in vaccum and studied their lithium storage performance. The electrodes of pristine $Ti_3C_2T_x$ and $Ti_3C_2T_x$ calcined at 400 °C delivered specific capacities of 87 and 126 mAh g^{-1}, respectively after 100 cycles at 1C [50]. The higher capacity value of the $Ti_3C_2T_x$ calcined at 400 °C is ascribed to the removal of the –OH functional groups, compared with pristine $Ti_3C_2T_x$. Likewise, Lu et al. prepared $Ti_3C_2T_x$ with lower amounts of –F groups by a hydrogen annealing process. The electrode from obtained $Ti_3C_2T_x$ with lower amounts of –F exhibited higher capacities and better rate capability than that of as-prepared $Ti_3C_2T_x$ [51].

In addition to titanium-based MXene (Ti_3C_2 and Ti_2C), other types of MXenes such as vanadium-based and niobium-based MXenes were also developed for the lithium storage application. Naguib et al. first used Nb_2CT_x and V_2CT_x as anode materials for LIBs [52]. The Nb_2CT_x and V_2CT_x electrodes exhibited a reversible capacity of 170 mAh g^{-1} after 100 cycles at 1C and a reversible capacity of 288 mAh g^{-1} after 150 cycles at 1C, respectively. Moreover, both of these two electrodes showed excellent capability at high cycling rates (10 C), indicating fast Li diffusion between Nb_2CT_x and V_2CT_x layers.

Although outstanding rate capability and cycling stability have been achieved for MXene electrodes, comparatively lower specific capacity even compared with graphite (372 mAh g^{-1}) still hinders their application for LIBs. Hence, constructing composites of MXenes with high-capacity anode materials (conversion anode materials, alloy anode materials), which generally show issues of cyclability mostly related to volume expansion during cycling and rate capability is a promising way for enhanced lithium storage performance.

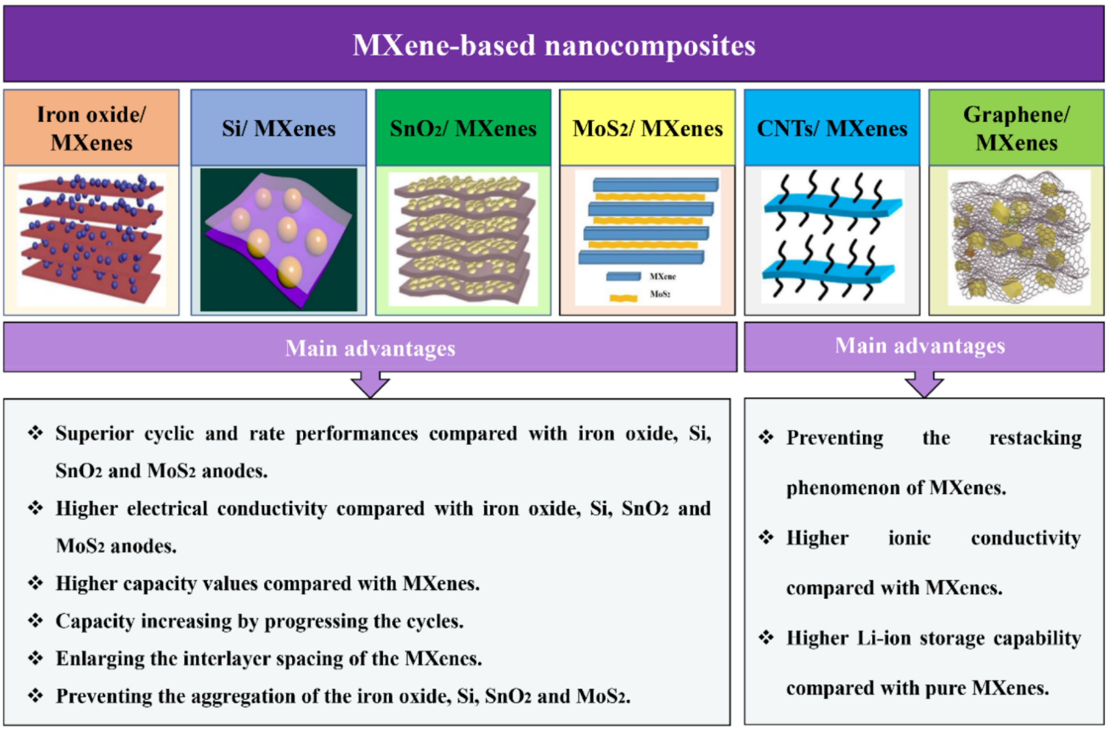

Figure 6. Summary of the most important MXene-based nanocomposites. Reproduced with permission from Ref. [53].

Figure 6 summarizes several types of MXene composites, which have been investigated and lists the main advantages of these composites when used as anode materials for LIBs [53]. Wang et al. prepared $Fe_3O_4/Ti_3C_2T_x$ composites with different ratios by the liquid assembly method [54]. The electrodes of $Fe_3O_4/Ti_3C_2T_x$ composites with ratios of 1:5, 1:2.5, and 1:1 exhibited specific capacities of 355.7, 747.4, and 173.8 mAh g^{-1}, respectively, at 1 C after 1000 cycles. They concluded that the excessive content of Fe_3O_4 (1:1) in the composite could not be efficiently accommodated into the $Ti_3C_2T_x$, resulting in fast capacity fading of the electrode. While the low capacity for the composite with a mass ratio of 1:5 can be ascribed to the low content of Fe_3O_4. By comparison, the composite with a suitable mass ratio of 1:2.5 (Fe_3O_4:$Ti_3C_2T_x$) showed the best cycling stability and highest specific capacity among composites, demonstrating a significant improvement in lithium storage after the construction of $Fe_3O_4/Ti_3C_2T_x$ composites. Other publications also report the preparation and lithium storage performance of $Fe_2O_3/Ti_3C_2T_x$, Fe_2O_3/nitrogen-doped $Ti_3C_2T_x$, and Fe_2O_3/few-layer Ti_3C_2 composites [55-57]. Additionally, Li et al. synthesized the carbon-coated Fe_3O_4 composites (C-Fe_3O_4)/$Ti_3C_2T_x$ by a hydrothermal method and liquid assembly process [58]. They demonstrated that the presence of carbon coating on the Fe_3O_4 could act as an adhesive between Fe_3O_4 and $Ti_3C_2T_x$. When used as anode material for LIBs, the C-$Fe_3O_4/Ti_3C_2T_x$ electrode exhibited better cyclic performance than that of both carbon-coated Fe_3O_4 and $Ti_3C_2T_x$ at current densities of 200 and 1000 mA g^{-1} and superior rate capability that presented a reversible capacity of 340 mAh g^{-1} after 200 cycles at a high current density of 7 A g^{-1}.

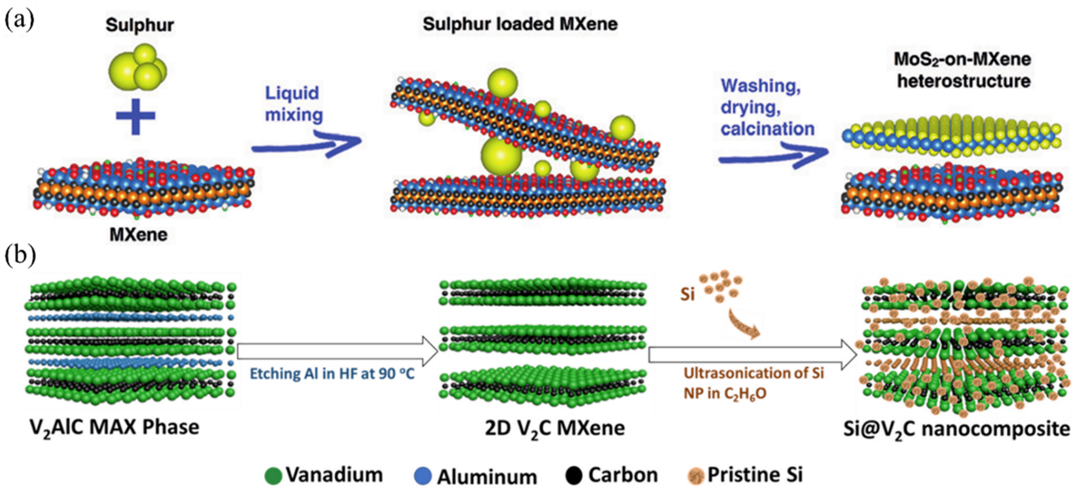

Figure 7. Examples of the current research on MXene-based composites for LIBs: (a) Schematic illustration of the preparation of MoS_2 on $Mo_2TiC_2T_x$ MXene heterostructures. Reproduced with permission from Ref. [60]. (b) Schematic illustration of the synthesis process of Si@V_2C nanocomposite. Reproduced with permission from Ref. [61].

In addition, other conversion anode materials like MoS_2 were integrated with MXenes for enhanced lithium storage performance. Zheng et al. synthesized the partially oxidized MXene/MoS_2 composite (p-Ti_3C_2/MoS_2) via a one-step hydrothermal process [59]. The p-Ti_3C_2/MoS_2 electrode with theoretical MoS_2 content of 10% exhibited a reversible capacity of 230 mAh g^{-1} after 50 cycles at a current density of 500 mA g^{-1}. Interestingly, Chen and coworkers prepared few-layered MoS_2 on $Mo_2TiC_2T_x$ MXene heterostructures by an in situ sulfidation method (Figure 7a) [60]. When used as anode material for LIBs, the as-prepared heterostructures exhibited high specific capacities and Coulombic efficiencies, promising rate capability, and excellent cycling stability.

As potential alloy anode material, silicon (theoretical capacity of 4200 mAh g^{-1} [27]) was also used to form composites with MXenes. Bashir et al. prepared Si@V_2C composite via the sonication-assisted liquid assembly method (Figure 7b) [61]. The electrode of this Si@V_2C composite exhibited significant improved cyclic stability and rate capability for lithium storage in comparison to that of pristine Si and V_2C anodes, resulting in a retained capacity of 430 mAh g^{-1} after 150 cycles at 200 mA g^{-1}. Zhang and coworkers reported the MXene/Si@SiO_x@C composite via integrating the Stöber method, magnesiothermic reduction, and carbonation [62]. When used for LIBs, this composite electrode displayed a stable capacity of 1547 mAh g^{-1} after 200 cycles at a current density of 0.2 C.

1.3 Conversion anode materials

Conversion anode materials, represented by transition metal oxides and sulfides, share the conversion mechanism:

$$\mathrm{M_xR_y + 2yLi^+ + 2ye^- \rightarrow yLi_2R + xM}$$

Here M is a transition metal, and R is O, S, or Se.

During conversion reactions, the lithium ions first intercalate into the anode materials, and the intercalated materials are further lithiated to metallic phases dispersed in amorphous Li_2O [63]. Conversion anode materials can deliver high specific capacities of 500-1200 mAh g^{-1} [31]. Besides, their production costs will be on the low side when compared with alloy anode materials. However, they have the issues of material pulverization, resulting from large volume expansion during cycling and poor rate performance caused by low electric conductivity and sluggish lithium movement in conversion anode materials [64, 65]. In order to address these problems, nanoscale materials design and the combination of carbonaceous materials and the conversion anode materials are effective ways [64, 65].

In the following chapter, a review of the research progress on conversion anode materials related to the thesis and their composites for LIB application is presented.

1.3.1 The research progress of transition metal oxides and their composites for LIBs

Transition metal oxides (MO_x, where M is a transition metal including iron, cobalt, nickel, copper, zinc, molybdenum, and tungsten) attract a lot of interest as candidates for LIB anode materials due to toxicity, and high specific capacity. In this part, the progress on the tungsten oxides and molybdenum oxides and their composites with carbonaceous materials for lithium ion storage is discussed.

WO_3: Based on the conversion reaction of WO_3, the theoretical specific capacity of WO_3 is calculated to be 693 mAh g^{-1} [66]. Although a high specific capacity can be achieved for a WO_3 electrode, fast capacity fading is inevitable because of the large volume expansion during discharging (the theoretical volume expansion is about 66%) [67]. The design of nanoscale electrode material has been widely studied to improve its cycling stability. Nanostructured materials can not only increase the contact area between electrodes and electrolytes but also shorten the lithium diffusion path. In addition, the nanostructure could also accommodate the volume expansion during cycling [67]. Yin et al. synthesize a hierarchical structure r-WO_3 by using a simple amino-

acid-assisted hydrothermal method [68]. The electrode of the obtained sample exhibited an initial discharge capacity of 515.1 mAh g^{-1} at 200 mA g^{-1}. The discharge capacity of 270 mAh g^{-1} was retained after 60 cycles at 200 mA g^{-1}. Qiu et al. fabricated hierarchical porous r-WO_3 micro flowers through a morphology-conserved transformation method [69]. The porous flower-like WO_3 delivers a reversible specific capacity of about 470 mAh g^{-1} after 25 cycles and also exhibited comparative rate capability. Sim et al. prepared yolk-shell hollow spheres of r-WO_3 via a spray pyrolysis approach [70]. The electrode showed a higher discharge capacity of 523 mAh g^{-1} and better cycling performance than WO_3 powder after 120 cycles at 300 mA g^{-1}.

Besides, Tong et al. fabricated hierarchical hollow microspheres r-WO_3 by developing a one-pot and template-free solvothermal method [71]. The electrode of the synthesized sample exhibited a high initial specific capacity of 1700 mAh g^{-1} and good cycling stability with a specific capacity of 700 mAh g^{-1} left after 100 cycles at 100 mAh g^{-1}. In addition, the electrode could still show a specific capacity of 213 mAh g^{-1} at a large current density of 1600 mA g^{-1}.

Nonstoichiometric tungsten oxide: Defect engineering has been shown to be an effective way to improve the electrochemical properties of electrode materials [72]. In the case of WO_3, its lattice can withstand many oxygen vacancies causing the production of nonstoichimetric WO_{3-x} ($0<x<1$). The existence of oxygen vacancies in WO_{3-x} does not destroy the WO_3 framework but enhance the conductivity [73]. Numerous oxyen deficient WO_{3-x} materials, such as $WO_{2.92}$, $WO_{2.9}$, $WO_{2.83}$, $WO_{2.8}$, $WO_{2.77}$, $WO_{2.72}$, $WO_{2.67}$, and $WO_{2.63}$, have been reported [74, 75].

Sun et al. reported the synthesis and battery performance of mesoporous $W_{18}O_{49}$ nanobelts (m-$W_{18}O_{49}$ NB or m-$WO_{2.72}$ NB) with abundant oxygen vacancies [76]. The preparation process included a simple solvothermal process and a calcination treatment. The m-$W_{18}O_{49}$ NB electrode exhibited a high initial discharge specific capacity of about 1320 mAh g^{-1} and a discharge capacity of 1284.8 mAh g^{-1} at 100 mA g^{-1} after 120 cycles. The m-$W_{18}O_{49}$ NB electrodes show much higher specific capacities and better cycling stability than the mesoporous WO_3 nanobelts (m-WO_3 NB) and bulk $W_{18}O_{49}$ (b-$W_{18}O_{49}$). The superior lithium storage performance of m-$W_{18}O_{49}$ NB electrodes might be ascribed to two aspects: (1) enhanced electronic conductivity and more active sites for conversion reactions provided by the abundant oxygen vacancies. (2) Short diffusion path for lithium ions and larger contact area between the electrode and electrolyte derived from the mesoporous structure.

Tungsten oxide composites: Besides downsizing or the design of unique structure of tungsten oxides, integrating carbonaceous materials with it is also a commonly used way to improve the electronic conductivity and the cyclic stability of electrodes. Zeng and coworkers prepared a 3D hierarchical sandwich-like nanocomposite of tungsten oxide nanoplates and graphene (TTNPs-GS) [77]. The obtained TTNPs-GS electrode exhibited a high initial discharge capacity of 1261 mAh g^{-1} at 72 mA g^{-1} and delivered a specific capacity of 792 mAh g^{-1} at 180 mA g^{-1} after 50 cycles. In addition, the TTNPs-GS electrode also showed excellent rate capability and long cycle life (615 mAh g^{-1} after 1000 cycles at 1080 mA g^{-1}). Gu et al. synthesized a composite of bamboo-like WO_3 nanorods anchored on three-dimensional nitrogen-doped graphene frameworks (r-WO_3/3DNGF) via a hydrothermal process and a post-heating treatment [78]. Compared with the pristine WO_3 electrode, the r-WO_3/3DNGF-20 electrode (20 wt% 3DNGF in the composite) exhibited better cyclic stability, and a reversible capacity of 828 mAh g^{-1} is maintained after 100 cycles at 100 mA g^{-1}. A good rate capability of r-WO_3/3DNGF-x electrodes (x=30, 20, 10, and 5) could also be observed. Gu and coworkers believed the synergistic effects of n-doped graphene and WO_3 help improve the lithium storage performance of the r-WO_3/3DNGF composites [78]. Park et al. reported a similar composite of WO_3 and reduced graphene oxide (WO_3/RGO) [79]. The WO_3/RGO composite delivered a reversible capacity of 487 mAh g^{-1} at 150 mA g^{-1} over 100 cycles, which shows a clear enhancement in capacity compared with pristine WO_3 and RGO.

Molybdenum oxides including molybdenum trioxide (MoO_3), molybdenum dioxide (MoO_2), and MoO_{3-x} ($0<x<1$) have been extensively considered due to high theoretical capacities (MoO_3 1117 mAh g^{-1}, MoO_2 838 mAh g^{-1}), low cost, chemical stability, and the environmentally friendly nature [80].

MoO_3: Among several MoO_3 polymorphs, orthorhombic MoO_3 (α-MoO_3) and hexagonal MoO_3 (h-MoO_3) are mostly investigated as anode materials for LIBs. Zakharova et al. develop a microwave-assisted hydrothermal route to prepare both α-MoO_3 and h-MoO_3 [81]. They found that when the voltage range is limited to 1.5-3.5 V, the α-MoO_3 electrode exhibited better cycling stability than that at the voltage range of 0.1-3.0 V due to the disappearance of the irreversible conversion reaction at low voltage (around 0.4 V). In addition, α-MoO_3 is more suitable for reversible electrochemical Li^+ storage than h-MoO_3, which can be ascribed to the inferior structural stability of h-MoO_3. In order to improve the cycling stability and rate capability of MoO_3, special structure designs like nanostructure and composite construction with carbonaceous materials were reported. Xia and coworkers fabricated a MoO_3/carbon nanocomposite by using a facile one-pot route [82]. The MoO_3/C electrode showed a high discharge capacity of 1260 mAh g^{-1} at 100 mA g^{-1}, the capacity decreased very fast in the first 20 cycles and keep stable in the following 80 cycles. The good cycling performance was explained with the fact that the uniformly dispersed carbon accommodates the volume change during cycling. Nadimicherla et al. prepared single crystalline flower like α-MoO_3 nanorods (α-MoO_3 NR) via a simple solvothermal approach [83]. The α-MoO_3 NR electrode exhibited a high initial specific discharge capacity of 1182 mAh g^{-1} and capacity retention of 55% after 189 cycles at 30 mA g^{-1}. Zhang et al. prepared a nanocomposite composed of nitrogen-doped carbon nanotubes with α-MoO_3 (α-MoO_3/N-CNTs) [84]. The α-MoO_3/N-CNTs electrode showed improvement in the cycling performance and rate capability in comparison with pristine MoO_3, attributed to the structural integrity and good conductivity derived from the interconnected α-MoO_3 and N-CNT framework.

MoO_2: MoO_2 has been suggested as a promising anode material for LIBs owing to its relatively high electrical conductivity, high reversible capacity, and good chemical stability [85]. Fast capacity

fading and poor rate performance of the pristine MoO_2 electrode, however, hinder its further application for LIBs. Therefore, a number of nanostructured MoO_2 like MoO_2 nanoparticles, nanorods, nanotubes as well as composites of MoO_2 and carbon-based materials have been reported with enhanced electrochemical properties [86, 87]. Wang et al. developed a facile synthesis method to prepare triple-shelled MoO_2/C composited hollow spheres [88]. The MoO_2/C electrode exhibited an initial discharge capacity of 1139 mAh g^{-1} with a Coulombic efficiency of 67% and a reversible capacity of about 580 mAh g^{-1} at 500 mA g^{-1} after 200 cycles. Zhang and coworkers designed 3D hierarchical MoO_2/C composites (MoO_2/CF), where MoO_2 nanoparticles were embedded in the carbon microflowers via a facile self-assembly method [89]. Thanks to the synergistic effect of MoO_2 and carbon, the MoO_2/CF electrode showed a high reversible capacity of 690 mAh g^{-1} after 200 cycles at 500 mA g^{-1} and a specific capacity of 576 mAh g^{-1} over 200 cycles at a high current density of 1000 mA g^{-1}. Sun and coworkers fabricated a hierarchical MoO_2/graphene hybrid by sonication and a calcination process. This hybrid electrode showed the typical electrochemical behavior of MoO_2 and excellent rate performance at high current densities [90]. Yang et al. synthesized hierarchical MoO_2/N-doped hetero-nanowires (MoO_2/N-C H-NW) by simple calcination using organic–inorganic hybrid nanowires as a precursor and self-template [91]. In this unique structure, the MoO_2 nanoparticles were embedded in the one-dimensional N-doped carbon matrix, promoting the pseudocapacitance, decreasing the charge resistance, and buffering the volume change of MoO_2 during cycling. As a result, the MoO_2/N-C H-NW electrode exhibited a reversible capacity of 700 mAh g^{-1} after 400 cycles at 2000 mA g^{-1}, which still remained 570 mAh g^{-1} after 1500 cycles.

1.3.2 The research progress of tungsten disulfides and their composites for LIBs

Tungsten disulfide (WS_2) also attracted considerable attention due to its comparatively high conductivity and layered structure for lithium ion battery applications. Similar to other conversion anode materials, nanostructured WS_2 was also widely synthesized to improve the battery performance. Liu et al. fabricated an ordered mesoporous WS_2 via a vaccum impregnation route [92]. The mesoporous WS_2 electrode exhibited a higher initial efficiency (79.8%) than the bulk material (74.1%), demonstrating a lower irreversible capacity of 264 mAh g^{-1} for the mesoporous WS_2 electrode compared to the bulk counterpart (325 mAh g^{-1}). Moreover, compared with the bulk WS_2, better cyclic stability over 100 cycles and rate capability were achieved for the mesoporous WS_2 electrode.

Likewise, carbon-based materials like graphene and carbon nanofiber were adopted to form composites with WS_2. Kim et al. prepared onion-liked WS_2 on graphene nanosheets (WS_2@G) by ball-milling and a sulfidation treatment [93]. Compared with the pristine WS_2 electrode, although a similar initial specific capacity was achieved, the WS_2@G electrode exhibited a reversible capacity of about 385 mAh g^{-1} after 150 cycles at 100 mA g^{-1}, indicating a big improvement in capacity retention. In addition, in order to obtain better cyclic stability, the carbon-coated WS_2@G (C@WS_2@G) was prepared. The synthesized C@WS_2@G electrode showed a high capacity retention of 61.9% after 500 cycles at a high current density of 1000 mA g^{-1}. Wang and coworkers prepared aerogels of WS_2, carbon nanotube, and reduced graphene (WS_2/CNT-rGO) with an ordered microchannel 2D structure through a simple solvothermal method and an ice-template assisted post-freeze-drying process. Benefiting from the obtained unique structure, the WS_2/CNT-rGO electrode showed capacity retention of 99% after 100 cycles at 100 mA g^{-1}, implying the synergistic effect between WS_2 nanosheets and CNT-rGO networks.

Zhang et al. developed a novel and efficient method to prepare a hierarchical WS_2/graphene-carbon nanofiber (WS_2/GCNF) hybrid, which the uniform growth of WS_2 nanosheets on a GCNF membrane [94]. The WS_2/GCNF electrode delivered a high capacity of 1128.2 mAh g^{-1} at 100 mA g^{-1}, and excellent capacity retention of 95% after 100 cycles. In addition, outstanding rate performance was also obtained for the WS_2/GCNF electrode. Zhang and coworkers concluded that the 3D porous nanofiber networks of WS_2/GCNF could not only effectively facilitate the transport of electrons for the fast reaction of WS_2, but also maintain the structural integrity by mitigating volume expansion during cycling [95].

1.4 Aims

As presented above, many efforts have been taken to improve the lithium ion battery performance of these advanced metal-based anode materials. However, there are still some urgent issues that need to be solved.

First, for transition metal oxides and sulfides, most studies integrated them with high-cost carbonaceous materials like graphene, and carbon nanofibers. Although enhanced battery performance could be obtained for these composites, the complicated preparation route as well as the expensive carbon source make it hardly applicable for industry application. Therefore, a simple and low-cost strategy should be developed to prepare composites of transition metal oxides and sulfides with carbonaceous materials for high-performance lithium ion batteries.

Next, for transition metal carbides (MXenes), so far, most studies focused on the standard MXene, Ti_3C_2, and its composites for lithium ion battery application, while little attention was paid to investigating the electrochemical behavior of other two important MXenes (Nb_2C and V_2C). Besides, similar to the case of graphene, exfoliated few layers MXenes are widely used to support other anode materials to construct composites, however, the layered structures of unexfoliated multilayer MXenes, which are generated from the preparation process are rarely studied. This is because the multilayer MXenes dispersion in water is quite unstable, which could hardly combine with other materials in further processes like liquid assembly and hydrothermal process. Additionally, there are only few investigations on the composites of MXene with other anode materials and the improvement of lithium storage performance in these composites is also unsatisfactory due to limited preparation routes and inappropriate structure design of composites.

Hence, the studies in this thesis adopt several useful and facile routes to overcome the above issues, which are shown in the following chapters.

2. Experimental methods

2.1. X-ray diffraction

Powder X-ray Diffraction (PXRD) is a technique to determine the crystallographic structure of materials. In PXRD, the generated monochromatic X-rays interact with samples. The interaction of the incident rays with the sample produces constructive interference (and a diffracted ray) when conditions satisfy Bragg's Law [96]:

$$2d \sin \theta = n\lambda \qquad (7)$$

Here d is the spacing of the crystal layers, θ is the incident angle (the angle between the incident ray and scattering plane), λ is the wavelength of the X-rays, and n is an integer. These diffracted X-rays are then detected, processed, and counted. Since the powdered material has random orientation, all possible diffraction directions of the lattice should be collected by scanning through a range of 2θ angles.

Owing to the finite volume of the sample, broadening of the observed peaks in the diffraction pattern may occur. The size of crystallites up to 100 – 200 nm can be estimated from this broadening using the Scherrer equation [96]:

$$D = \frac{K\lambda}{\beta\cos\theta} \qquad (8)$$

Where D is the mean size of the ordered crystallite domains, K is the Scherrer constant, λ is the wavelength of the X-ray, β is the full width at half maximum of the peak, and θ is the Bragg angle.

XRD data in this thesis were measured by I. Glass at the Institute of Earth Sciences at Heidelberg University by using a Bruker D8 Advance ECO X-ray diffractometer with Bragg-Brentano geometry and a SSD160 detector. The X-ray tube with a copper anode was operated at 30 kV and 33 mA, generating characteristic Cu-K$\alpha_{1,2}$ radiation with wavelengths of λ_1 = 1.540562 Å and λ_2 = 1.544390 Å.

2.2. Thermogravimetric analysis (TGA)

Thermogravimetric analysis is a method of thermal analysis. In this technique, the mass of a substance is monitored as a function of temperature or time, when the specimen is subjected to a controlled temperature in a controlled atmosphere. One can obtain the TGA curve by plotting the weight or weight percent versus time or temperature. This measurement provides some information about the physical and chemical phenomena of a specimen like phase transitions, adsorption/desorption, and thermal decomposition. Before starting TGA measurements, the experimental conditions including temperature range, temperature scanning rate, and sample atmosphere are chosen based on the expected result and the information of samples.

TGA can be used for the thermal stability assessment of substances, the decomposition mechanism of inorganic salts, and the compositional analysis of samples. In the battery field, TGA is usually used for the analysis of electrode materials, especially, the carbon content in active materials. In this thesis, chapter 4 gives an example of determining the carbon content in carbon-coated tungsten oxides and disulfides.

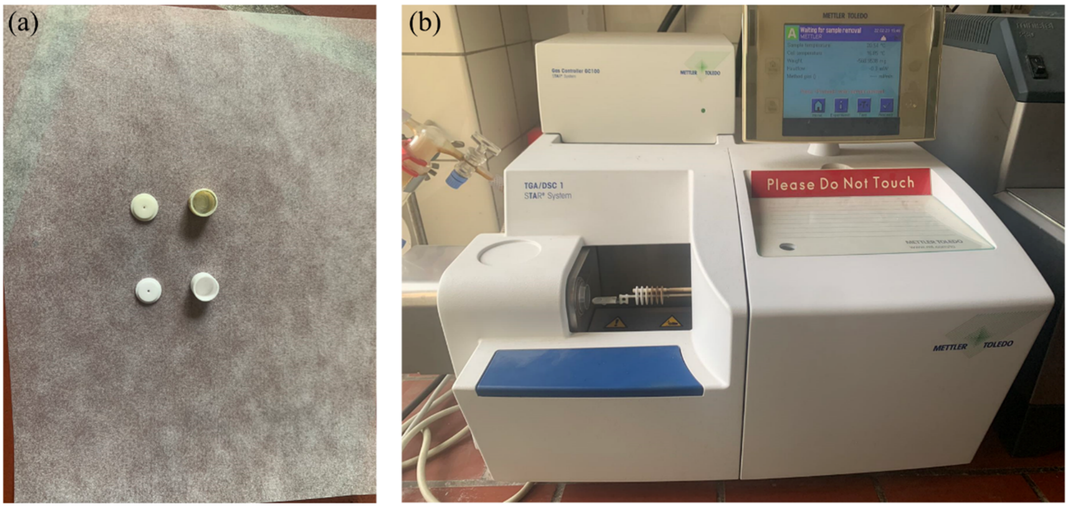

Figure 8. Photographs of crucibles (a) and the TGA device (b).

TGA measurements were conduct with Mettler Toledo TGA/SDTA 851e device at the Organisch-Chemisches Institut, Heidelberg University (Bunz group). The device mainly includes the furnace, gas, system, and software system. In this thesis, the measurements were all performed under air. For the measurement, firstly, several mg of powdered samples were added to a crucible (Figure 8a). The sample crucible and a reference crucible were then transferred to the holder which is attached to the end of the TGA sensor and bears the reference and sample crucibles, acting as a weighting pan (Figure 8b). A protocol including the temperature range, gas flow rate, and temperature gradient for the TGA measurement was set in the STAR^e software. After sending the protocol to the other systems in the TGA device, the measurement would run automatically. The crucibles were taken out of the furnace after cooling to room temperature and cleaned by a burner. Before starting the measurement for samples, a blank experiment with an empty crucible was conducted. The TGA data were collected and analyzed by subtracting the blank.

2.3. Scanning electron microscopy (SEM)

SEM generates various signals, which contain information about the surface topography and composition of samples by using a focused beam of high-energy electrons interacting with the sample. Various signals produced from SEM by interactions of the electron beam with the sample include secondary electrons, back-scattered electrons, diffracted backscattered electrons that are used to determine crystal structures and orientations of minerals, as well as photons (characteristic X-rays that are used for elemental analysis), visible light (cathodoluminescence), and heat [97]. Among them, backscattered electrons and secondary electrons are commonly used as two modes of electron detection that allow for different types of imaging and analysis. Backscattered electrons can be detected to show contrast based on different chemical compositions across an image, while secondary electrons give information about the surface topography. Besides, the generated characteristic X-ray with a fixed wavelength unique to its atomic number can be detected in an energy-dispersive X-ray spectrum (EDX or EDS). This measurement gives information about the elemental composition of samples at one point by line scanning, or the elemental distribution at a large region by the mapping mode [98].

SEM is operated at a high vacuum and it normally achieves a resolution of tens of nanometers. During the SEM measurement, a charging effect will occur if the sample is non-conductive or low-conductive. This phenomenon is derived from the accumulation of negative charges on the sample with low conductivity when irradiated by the electron beam. The charging effect could cause image distortion and contrast irregularities. Therefore, for non-conductive or low-conductive samples, methods are adopted to obtain high-quality SEM images like gold coating on samples, operating at an environmental SEM (ESEM) or low-voltage mode.

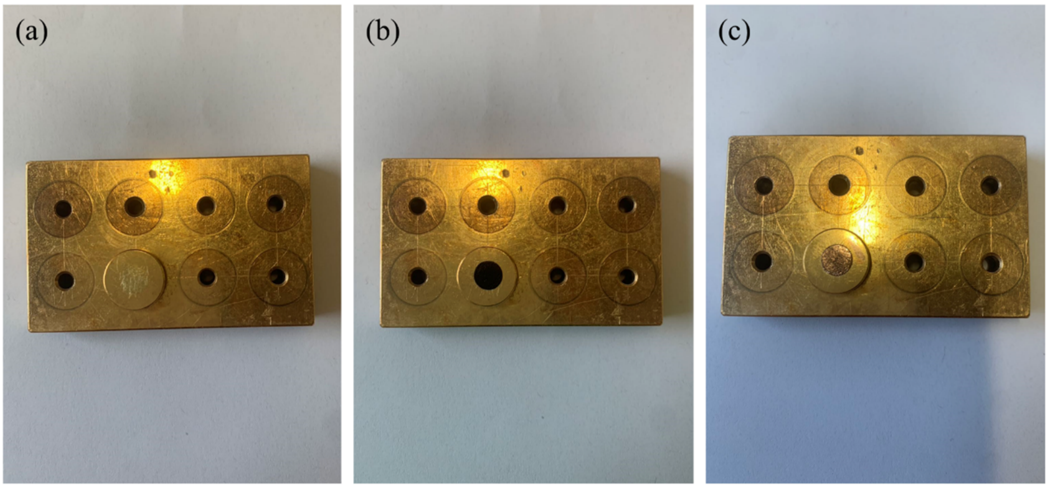

Figure 9. Photographs of the sample preparation process for SEM measurements: pictures of a stub on panel (a), the carbon tab dispersed with the sampled glued on the stub before (b), and after gold coating (c).

Figure 9 shows the sample preparation process for SEM measurements. The carbon tab (EM-Tec CT6 Conductive double-sided adhesive carbon tabs, 6mm in thickness) is firstly glued to a stub, which is fixed on a panel. Next, the powdered sample is dispersed on the carbon tab. The sample is coated with gold if it is non-conductive or poorly conductive. The measurements were performed on a ZEISS Leo 1530 scanning electron microscope. The main chamber of the SEM device was first vented with nitrogen flow until the chamber pressure approaches atmospheric pressure. Afterward, the holder containing several stubs was transferred to the main chamber and pumped until the chamber pressure is below 2×10^{-5} mbar. Next, stage navigation was used to set the position of the holder. The electron gun and Electron High Tension mode were turned on sequentially to produce and accelerate electrons. After changing the detection mode, the SEM images could be observed and recorded.

2.4. Transmission electron microscope (TEM)

Different from SEM, the transmitted electrons are collected after passing through the sample and the image is formed on the fluorescent screen, either by using the transmitted beam or by using the diffracted beam of the TEM measurement. Consequently, TEM provides invaluable information on the inner structure of the sample, While SEM offers information on the surface and composition of samples. TEM normally requires a sample thickness of less than 100 nm. In addition, High-Resolution TEM (HRTEM) and TEM-energy dispersive spectroscopy (TEM-EDS) help to identify the crystal structure and element composition of samples. TEM measurement require thin and flat samples on dedicated grids (e.g. copper grids).

TEM data including TEM images, HRTEM images, and TEM-EDS were measured by Wojciech Kukułka and Tomasz Kędzierski from the West Pomeranian University of Technology, Poland. The measurements were conducted on a Tecnai F30 transmission electron microscope (FEI Corporation, USA) at an acceleration voltage of 200 kV. The elemental mapping was performed on a scanning transmission electron microscope unit (STEM) with a high-angle annular dark-field detector (HAADF) (FEI, Tecnai F30) operating at an acceleration voltage of 200 kV.

2.5. X-ray photoelectron spectroscopy (XPS)

X-ray photoelectron spectroscopy (XPS) is a technique for the compositional and chemical state analysis of the surface of a sample. The basic principle of XPS is the photoelectric effect described by Einstein (1905), in which electrons are emitted from atoms in response to impinging electromagnetic radiation [99]. In XPS, the photoelectrons are produced when the sample is irradiated with X-rays. The kinetic energy of emitted electrons is analyzed to obtain the binding energy of electrons based on the following equation [99]:

$$E_{binding} = h\nu - (E_{kinetic} + \Phi) \qquad (9)$$

Here $E_{binding}$ is the binding energy of the electron measured relative to chemical potential, hν is the energy of the X-ray photons being used, $E_{kinetic}$ is the kinetic energy of electrons measured in the experiment and the work function Φ is a correction factor for the instrument and correlates to the minimum energy required to eject an electron from an atom.

Figure 10. Photographs of the sample preparation process for XPS measurements. Pictures of (a) copper pads before (top) and after polishing (bottom). (b) indium foil on the copper pad before (top) and after polishing (bottom). (c) sample dispersed on indium foil.

The sample preparationfor XPS measurement is presented in Figure 10. In the first step, the copper pad is polished with sandpaper. The indium foil is then pressed on the polished copper pad and the indium oxide on the surface of the indium foil is also removed. The sample powder is pressed into the indium foil, a brush is used to remove the loose powder. The prepared sample is used for the XPS measurement.

XPS data were measured by Zhiyong Zhao at the institute of Angewandte Physikalische Chemie, Universität Heidelberg (Zharnikov group). The measurements were conducted using a MAX 200 (Leybold-Heraeus) spectrometer equipped with a hemispherical analyzer (EA 200; Leybold-Heraeus) and an Mg Kα X-ray source. The XP spectra were acquired in normal emission geometry with an energy resolution of ~0.9 eV. The binding energy scale of the spectra was referenced to the Au $4f_{7/2}$ peak at 84.0 eV.

2.6. Cyclic voltammetry (CV)

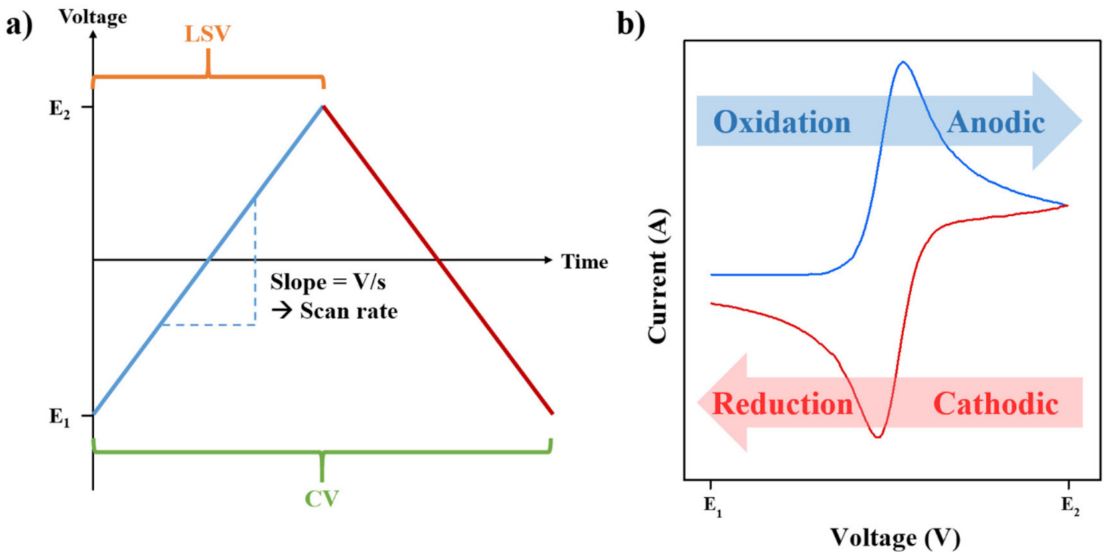

Figure 11. Voltage vs. time profile for the linear sweep and cyclic voltammetry (a). Typical cyclic voltammogram plotting (b). (a, b) Reproduced with permission from Ref. [100].

Cyclic voltammetry is a powerful electrochemical technique to investigate the oxidation and reduction processes of molecular species [100]. As shown in Figure 11a, the process is called Linear Sweep Voltammetry (LSV) if the current response is recorded by sweeping the potential linearly as a function of time. Similarly, CV measures the current response while the potential is swept linearly back and forth (from E1 to E2 and from E2 to E1) between the chosen limits. Figure 11b shows a typical CV plotting in which the blue peak represents the oxidation reaction at an anodic sweep and the red peak corresponds to the oxidation reaction at a cathodic scan.

CV curves can give information about the thermodynamics and kinetics of the electrode which is very useful for energy storage systems, especially the lithium ion battery. With CV measurements, one can know whether there are electrochemical reactions for an electrode at a given voltage range. One can further determine the potential at which an oxidation or reduction reaction occurs if there exist electrochemical reactions. In addition, information about the reversibility of electrochemical reactions is possible. Also, one can change testing conditions like scan rate, and temperature to understand the kinetic behavior of an electrode [100].

In this thesis, we mainly use the CV technique to investigate the electrochemical behavior of anode materials. The CV measurements were conducted on the electrochemical workstations Biologic BCS805 battery cycler series and Biologic VMP3 potentiostat. For our anode materials, the voltage range and scan rate were set as 0.01V-3V and 0.1 mV s^{-1}, respectively.

2.7. Galvanostatic cycling with potential limitation (GCPL)

Galvanostatic cycling with potential limitation (GCPL) is a technique to measure the charge-discharge curve of a cell at a constant current in a given potential range. This technique can give information about the discharge/charge capacities, cycling performance, and rate performance of a cell. During the measurement, the potential of the cell is recorded as a function of time. The specific capacity Q_m can be calculated by the Equation (10):

$$Q_m = \frac{1}{m}\int_{t_1}^{t_2} I(t)\,dt \qquad (10)$$

Here, Q_m is the specific capacity of the electrode, m is the mass of active materials in the electrode, t_1 and t_2 are the beginning time and ending time of discharging or charging respectively, and I(t) is the current applied on the cell.

For the GCPL measurement, the equation can be further simplified as $\Delta Q_m = I\Delta t$, which can easily give the value of the specific capacity. One will also obtain the cycling performance by plotting the specific capacity versus the cycle number. Similarly, the rate performance can be measured by using various current densities for specific cycle numbers.

Figure 12. Photographs of the VMP3 potentiostat (left) and the BCS805 battery cycler series (right) used in this thesis.

In this thesis, the GCPL measurements were performed by the electrochemical workstations Biologic BCS805 battery cycler series and Biologic VMP3 potentiostat (Figure 12). In addition, a current density of 100 mA g^{-1} was adopted for most measurements. A large current density of 500 mA g^{-1} or 1000 mA g^{-1} was used for long-term cycling stability measurements. During the GCPL measurements, the E vs t curve was recorded and can be converted to E vs capacity. The data was collected and analyzed by the software (Origin) to produce the charge/discharge curves as well as cycling performance.

2.8. Synthesis methods

In order to obtain different kinds of samples, various synthesis methods were used in this thesis. The transition metal carbides (Ti_3C_2, V_2C, and Nb_2C) and transition metal oxides including molybdenum oxides (MoO_3 and MoO_2) and tungsten oxides (WO_3 and WO_2) were synthesized by the hydrothermal method. For the preparation of the composites of transition metal oxides and carbon as well as metal disulfides, the solid state method was adopted after the hydrothermal. In addition, synthesis in the ball-milling method was developed to provide a simple and facile way to prepare MoO_3/Nb_2C composites.

2.8.1 Hydrothermal method

Figure 13. Photographs of a hydrothermal reactor.

The hydrothermal method is a way to use an aqueous solution in a special closed reaction vessel to create a high-temperature (above 100 ℃) and high-pressure (over 1 bar) reaction environment for sample synthesis.

The photographs of hydrothermal equipment in our lab are shown in Figure 13. It consists of an outer stainless steel reactor and an inner Teflon liner (white). Before starting the reaction, the raw materials are dissolved in water and transferred to the inner Teflon liner. The reactor is then sealed by screwing the cap and put in the heating chamber (Binder World ED023UL). The growth temperature and growth time are set according to different sample growth requirements.

The hydrothermal reactor should not be taken out until it cools to room temperature. After the disassembling process, the poorly water-soluble or insoluble sediments are collected and washed. A centrifuge (Hettich Mikro 22R) is used in the collection step. The centrifugation speed and centrifugation time are normally set to 6000 rpm and 5 minutes, respectively. Water washing is then the following step to remove impurities that can easily dissolve in water. After several times performing the above steps, the sediment can be sent to a vacuum oven for drying.

Advantages of the hydrothermal synthesis method include size and morphology control and the simple operation process. The hydrothermal synthesis method is simple to operate and can be easily scale-up to the industrial demand. Besides, one could control the crystal size and morphology by varying the hydrothermal conditions (reaction time, temperature, pH values, and capping agents). The capping agents are materials which used as stabilizing agent and provide colloidal stability, resulting in the controlled growth of crystal. Other methods like liquid assembly can be combined with the hydrothermal synthesis method to obtain the expected structure (see the $MoO_2/C/V_2C$ part for details). However, there are still some limitations to this method. Due to its aqueous environment, only oxides and some metal sulfides could be prepared. For air or water-sensitive samples, the synthesis is also difficult to realize. In addition, restricted by the Teflon liner, hydrothermal temperatures over 200 ℃ can not be applied, which restricts the temperature requirement for some materials.

Figure 14. Pictures of the ball-milling device

2.8.2 Ball-milling method

Ball milling is a mechanical technique that is used to grind powders to fine particles or prepare composites. Especially, this method, dominated by the shear force, provides a simple and low-cost way for the synthesis of composites. Figure 14 presents pictures of the ball milling device (Retsch Planetary Ball Mill PM 100). It mainly includes the rotating shell which creates centrifugal force, the grinding jar with different volumes, and the grinding balls. Both dry grinding and wet grinding can be applied to the synthesis process based on the requirement of final products. Besides, a suitable ball size is also important for the process. In our experiment, ZrO_2 balls with a diameter of 1mm were adopted.

The raw materials and balls are slowly added to the grinding jars during preparation. The solvent is added if the wet grinding method is used. The grinding jar is then transferred to the rotating shell and fixed. The parameters should be set carefully like the ball milling time, and the ball milling speed. After the ball milling process, the sample is collected by washing it with solvents and dried.

For battery research, the balling-milling method is normally developed for the preparation of cathode materials in combination with a solid-state reaction [101]. Additionally, it is also an effective way to prepare carbon-coated materials and nanosized materials for enhanced lithium storage materials [102, 103].

2.8.3 Solid state synthesis method

The solid state synthesis method is a process that does not include any solvent. In our case, it includes the carbonization process, sulfurization process, and annealing process. This device used for the method in this thesis consists of a tube furnace and a gas control system which can maintain the pressure value in the tube by adjusting the rate of gas flow. Inert gases like argon or nitrogen is used as a protective atmosphere and for transporting flow during the solid state reaction.

For the preparation process, the raw material in a crucible boat is put in the center of the tube. The tube is then sealed, pumped for 20 minutes, and flushed to atmospheric pressure with the inert gas. After three times pumping and flushing, the temperature program, time program, and gas flow rate are set. For the sulfurization process, an extra crucible boat containing a sulfur source is also required.

2.8.4 Etching method

The etching method is a way to prepare samples by etching precursors using various etching agents. In this thesis, HF etching and LiF+HCl mixed solution etching methods were used for the preparation of MXenes. Since hydrofluoric acid is highly toxic and corrosive, which is dangerous to operate in general chemistry labs, the HF etching experiments thus were conducted in HF-lab at the Institute of Earth Sciences, Heidelberg University (Pross group). Before starting the experiment, one must wear protective clothing including a lab coat, acid-resistant apron, close-toed shoes, long pants, and full-face goggles with side protection. HF should be handled inside of a fume hood and an HF spill kit should be nearby. After the etching reaction, $CaCl_2$ is used to react with residual HF in solution, resulting in the production of CaF_2 (insoluble in water) as well as HCl which was neutralized by a strong base e.g. NaOH.

2.9. Lithium ion battery preparation

2.9.1 Electrode preparation

The working electrode is prepared from a slurry, which is a mixture of active material, conductive additive, and the binder in the solvent. In our experiment, the synthesized material, carbon black (TIMCAL Graphite & Carbon, C-NERGY™ SUPER C65), and polyvinylidene difluoride (PVDF, Solvay Plastics) are used as active material, conductive addictive, and binder respectively. The synthesized material, carbon black, and PVDF are first added stepwise with a mass ratio of 7:2:1 to a 2 mL glass vial. N-methyl-2-pyrrolidone (NMP, Alfa Aesar, ⩾ 99.5%) is added as a solvent to immerse the above mixture. The obtained slurry is then stirred for 24 h and evaporated in a vacuum oven at 65°C and 11 mbar for 1-2 h until the dispersion has reached the right texture for further processing.

The slurry is pasted on current collectors when its viscosity reaches a status that the slurry can bind well with the current collectors. We used copper meshes with a diameter of 10 mm (Goodfellow Cambridge Ltd., Cu foil, thickness 0.25mm, 40x40wires/cm) as the current collector since all active materials worked as anode materials. In detail, several copper meshes are weighted first. After pasting, the electrode is dried in a vacuum oven for 24 h to remove residual solvent. The electrode is taken out and pressed at 10 Mpa for 10 seconds in a hydraulic press (RIKEN CD-10-10) before being used for further battery assembly.

2.9.2 Battery assembly

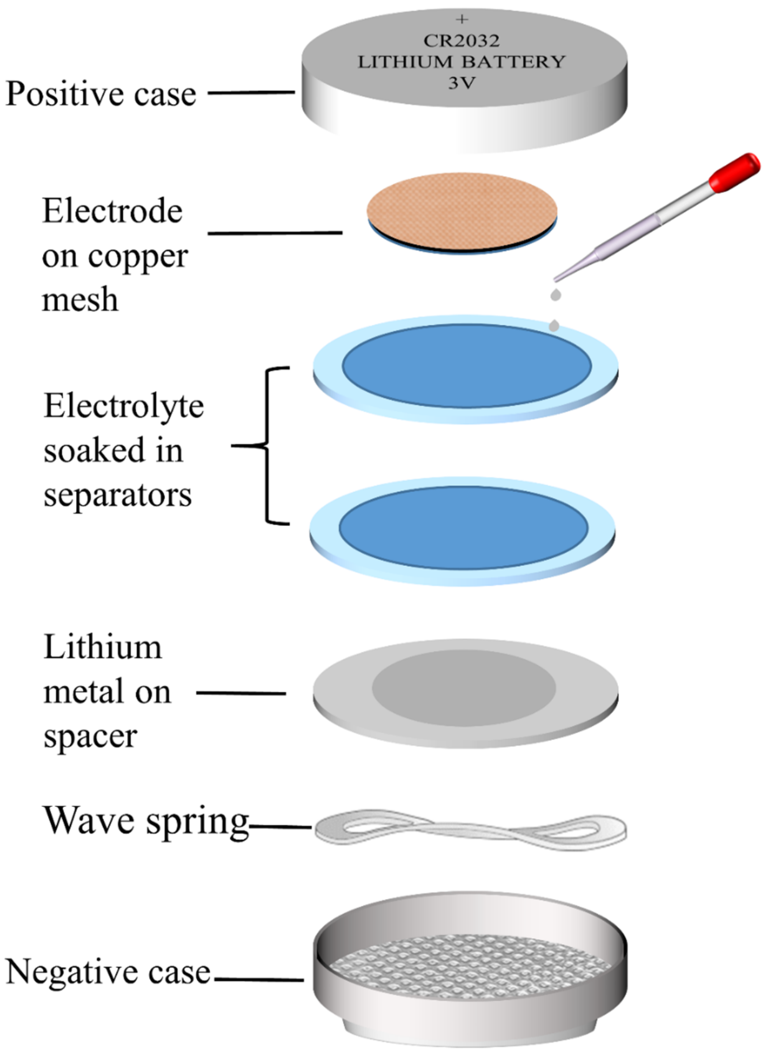

Figure 15. Illustration of a coin cell component.

The electrochemical measurements are performed using coin cells (CR2032) from which half cells with lithium metal as the counter electrode and the prepared electrode as the working electrode were built. The geometry and composition of these cells are depicted in Figure 15. A half cell consists of the working electrode, a counter electrode, electrolytes on two pieces of separators, coin cell cases, and a wave spring. For the assembly process, the working electrode (prepared electrode) is first transferred to the argon-filled glove box (O_2 < 0.1 ppm, H_2O < 0.1 ppm). A lithium foil (Sigma Aldrich) pressed on a nickel plate and two layers of glass microfiber separator (Whatman GF/D 70mm, GE Healthcare Life Sciences) soaked with 65µl of a 1 M solution of $LiPF_6$ in ethylene carbonate/dimethyl carbonate (EC/DMC 1:1 by volume) (LP30, Merck) are sequentially placed on a negative case. Followed by the electrode on a copper mesh and the positive case, the coin cell was sealed air-tight by pressing with 31.2MPa in a LITH-SF120 crimping machine (TMAX) with an MSK 640-G crimper (TMAX).

3. MXenes and their composite for battery application

3.1. Introduction

To meet the rapid development demand for next-generation LIBs with high energy density and long cycling life, enormous efforts were taken to find alternative anode materials such as transition metal oxides [104], transition metal sulfides [105-107], and silicon [108]. Among them, molybdenum oxides (MoO_2 and MoO_3) are potential candidates due to their high theoretical capacity (838 mAh g^{-1} for MoO_2 and 1117 mAh g^{-1} for MoO_3), the abundance, low cost, and environmentally friendly nature [109-112]. Unfortunately, the phase transformation and volume expansion occurring during the cycling process result in the pulverization of active materials and thereafter rapid capacity degradation. Moreover, their electrodes inevitably show inferior rate performance because of their poor electric conductivity [89,113-115]. To address these issues, constructing composites of molybdenum oxides and conductive carbon-based materials such as graphene or carbon nanotubes (CNTs) has been widely studied [116-118].

MXenes, a new class of layered materials, first reported by Gogotsi's group [33], have attracted widespread interest in multiple fields because of their excellent physical and chemical properties [37, 119]. As transition metal nitrides, carbides, and carbonitrides, MXenes are normally denoted as $M_{n+1}X_nT$, where M is an early transition metal, X is carbon and/or nitrogen, and T is surface functional groups. MXene nanosheets can be obtained by intercalation and sonication process [120]. Due to their high conductivity, excellent mechanical properties, and large surface area, a number of MXene nanosheets like Ti_3C_2 and Nb_2C were used to form composites with other high-capacity anode materials for lithium ion storage applications [121-123]. Bashir et al. prepared an MXene-supported Si@V_2C composite by a sonication-assisted method [61]. When used for lithium ion battery, the Si@V_2C composite anode exhibits a reversible capacity of 430 mAh g^{-1} after 150 cycles at 200 mA g^{-1}. Ai and coworkers synthesized SnS nanoparticles anchored in Ti_3C_2 nanosheet matrix composites via an electrostatic attraction method [124]. The composite electrode shows an impressive specific capacity of 646 mAh g^{-1} at the current density of 100 mAg^{-1} after 100 cycles.

However, the utility of unexfoliated multilayer MXene with the unique accordion-like structure for composite construction has not yet been realized. The unique 'open structure', generated during the etching process by the production of H_2 [33], could provide a framework to accommodate other anode materials and finally produce the hierarchical structure composites, which allows fast electron and ion transfer during cycling and full contact between electrolyte and electrode. Moreover, the volume expansion that happens to materials like molybdenum oxides can be buffered since the confinement effect from the hierarchical structure.

Here, pristine MXenes e.g. Ti_3C_2, V_2C, and Nb_2C, as fundamental materials were firstly prepared to investigate their lithium ion storage performance. The multilayer MXenes V_2C and Nb_2C were integrated with molybdenum dioxide and molybdenum trioxide via the electrostatic force-assisted hydrothermal method and the ball-milling method, respectively. When used as anode materials for LIBs, the obtained composites exhibits excellent battery performance.

3.2. MXenes for lithium ion battery application

For a better understanding and use of MXenes for lithium ion battery applications, in this chapter, pristine MXenes including Ti_3C_2 and V_2C were synthesized and investigated physically and electrochemically. Two preparation routes (HF etching process and HCl+LiF etching process) were adopted to compare the differences in morphology, crystal structure, and electrochemical behavior of the obtained products. Part of the electrochemical data was measured by Felix Lulay under the supervision of the author [125].

3.2.1. Synthesis of MXenes

Two kinds of etching procedures with HF solution or HCl+LiF mixed solution, were adopted to prepare MXenes.

(1) HF etching process: Here, firstly, the precursor MAX was immersed in HF (48 wt%) at 60 °C for 48h. The sample was washed with deionized water and centrifuged several times until the pH value was above 5. The powder was collected and dried in vacuum at 60 °C for 12h. In this thesis, the Ti_3C_2 MXene was prepared by this method from Ti_3AlC_2.

(2) HCl+LiF etching process: 1g LiF powder was dissolved in 9M HCl solution and magnetically stirred for 2h. The precursor MAX was then immersed into the above solution and the mixture was transferred to a 50 ml stainless steel autoclave lined with PTFE and heated at 90°C for 72h. The precipitate was collected after centrifugation, washed several times with water and ethanol until the pH value of the solution is above 5, and dried in an oven at 60 °C for 24 h. The obtained MXenes are denoted as m-MXenes. Here, m-Ti_3C_2, m-Nb_2C, and V_2C were prepared.

3.2.2. Ti_3C_2 for lithium ion battery application

3.2.2.1. Physical characterization

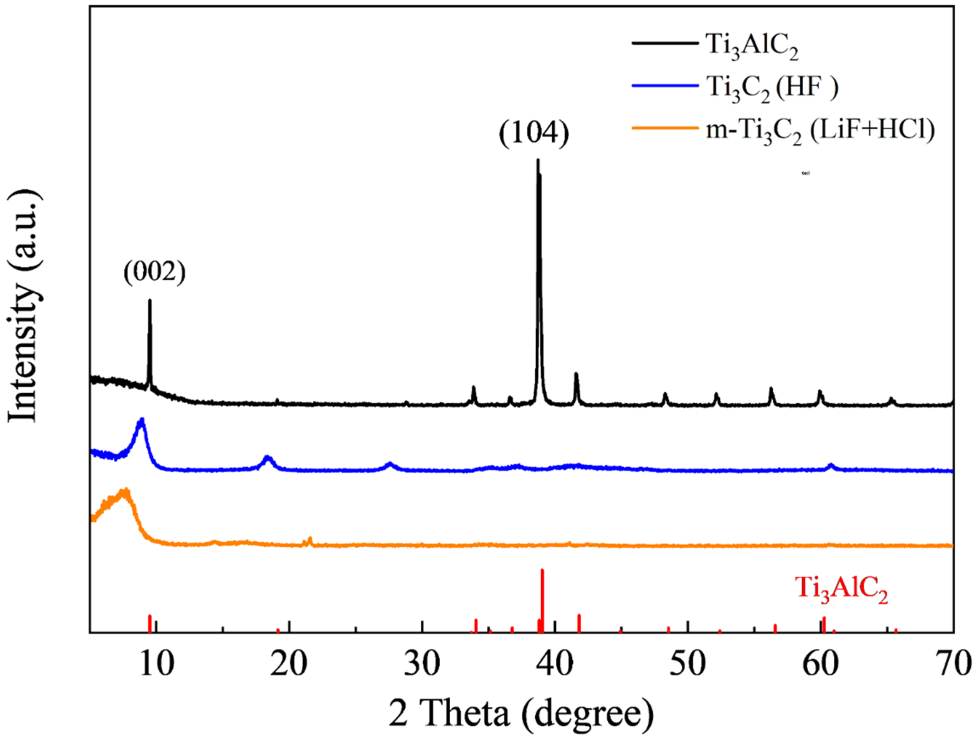

Figure 16. XRD patterns of Ti_3AlC_2, Ti_3C_2 made by the synthesis method (1), and m-Ti_3C_2 made by the synthesis method (2). Vertical ticks show the reference pattern of Ti_3AlC_2 according to ICSD code 153266 [126].

Ti_3C_2 has been prepared by the synthesis methods (1) and (2) using Ti_3AlC_2 as the precursor. Figure 16 shows the XRD patterns of the precursor Ti_3AlC_2 and synthesized Ti_3C_2 made by different etching agents. The XRD pattern of the precursor shows sharp diffraction peaks with the (002) and (104) peaks as the most prominent ones, in accordance with the reference diffraction pattern. After synthesis, the diffraction peak at 39° corresponding to the (104) plane of Ti_3AlC_2 strongly reduced for both Ti_3C_2 materials. Besides, the (002) peak of Ti_3C_2 shifts from 9.5° to a lower angle (8.7°) after the etching process. Both observations indicate the successful preparation of Ti_3C_2 [127]. For m-Ti_3C_2, a similar pattern can be observed, but the (002) peak of m-Ti_3C_2 displays a larger shift compared with Ti_3C_2 synthesized by HF solution, reflecting an increased interlayer distance due to the intercalation of Li ion during the etching process [123]. Furthermore, the absence of the (104) peak of Ti_3AlC_2 with LiF+HCl etching indicates better removal of Al in this product benefitting from the unique preparation method.

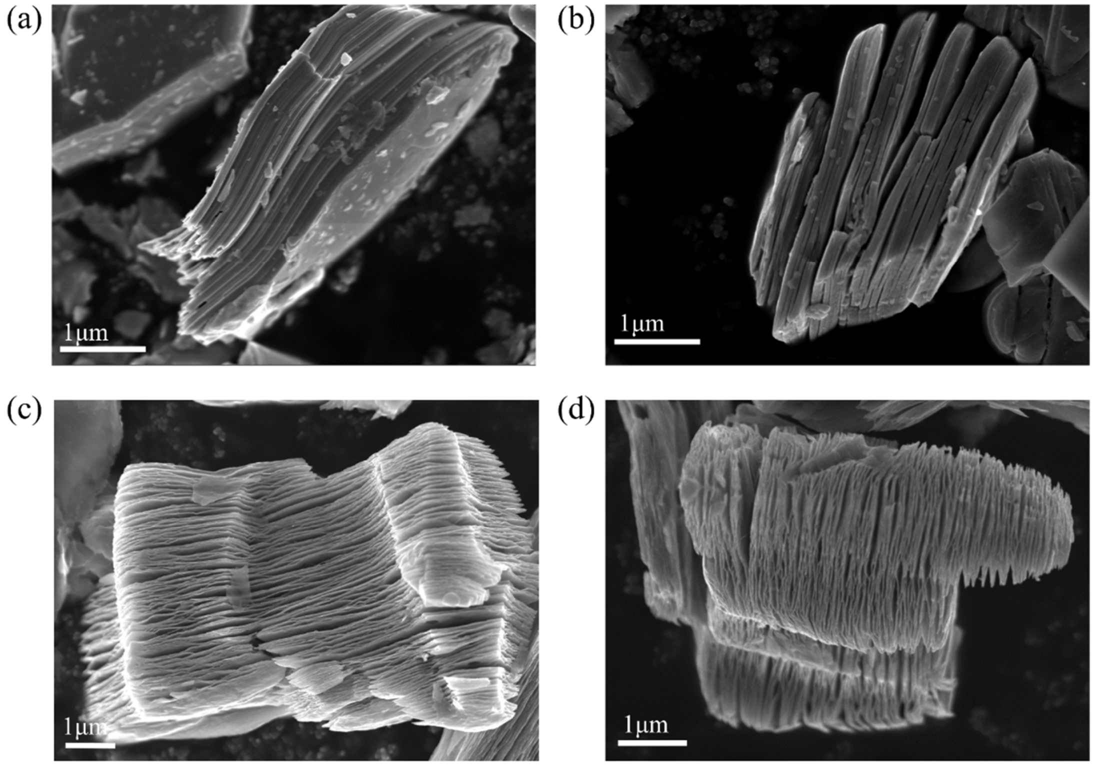

Figure 17. SEM images of Ti_3AlC_2 (a), Ti_3C_2 (b), and m-Ti_3C_2 (c, d). The SEM images were measured by Lennart Singer.

The morphology and element compositions of the precursor Ti_3AlC_2 and synthesized Ti_3C_2 were investigated by SEM and SEM-EDS. As shown in Figure 17a, Ti_3AlC_2 exhibits a compact bulky structure. After the removal of the Al layers, Ti_3C_2 (Figure 17b) shows an accordion-like morphology with some open structure which might be made due to the generation of H_2 during the etching process [33]. By comparison, the m-Ti_3C_2 (Figure 17c, d) displays a more open structure, which could be ascribed to the unique hydrothermal environment as well as the mixture of (LiF+HCl). Therefore, the occurrence of an accordion-like morphology is not the only indication for the successful synthesis of MXenes. Other results from XRD and EDS measurements are necessary to combine with SEM images of products to confirm the successful synthesis [128].

The ED spectra in Figure 18a, b show the existing elements in Ti_3C_2 and m-Ti_3C_2. After the etching process, there is still some Al left in both samples, indicating the only partial removal of Al. Similar results have been reported in many other studies [129, 130]. Interestingly, different surface functional groups were observed, F in Ti_3C_2 and Cl as well as F in m-Ti_3C_2, which could change the physical and chemical properties of the synthesized Ti_3C_2. According to theoretical calculations [48], these surface groups could change the electronic structure of MXene and therefore affect their electrochemical properties.

(a)

(b)

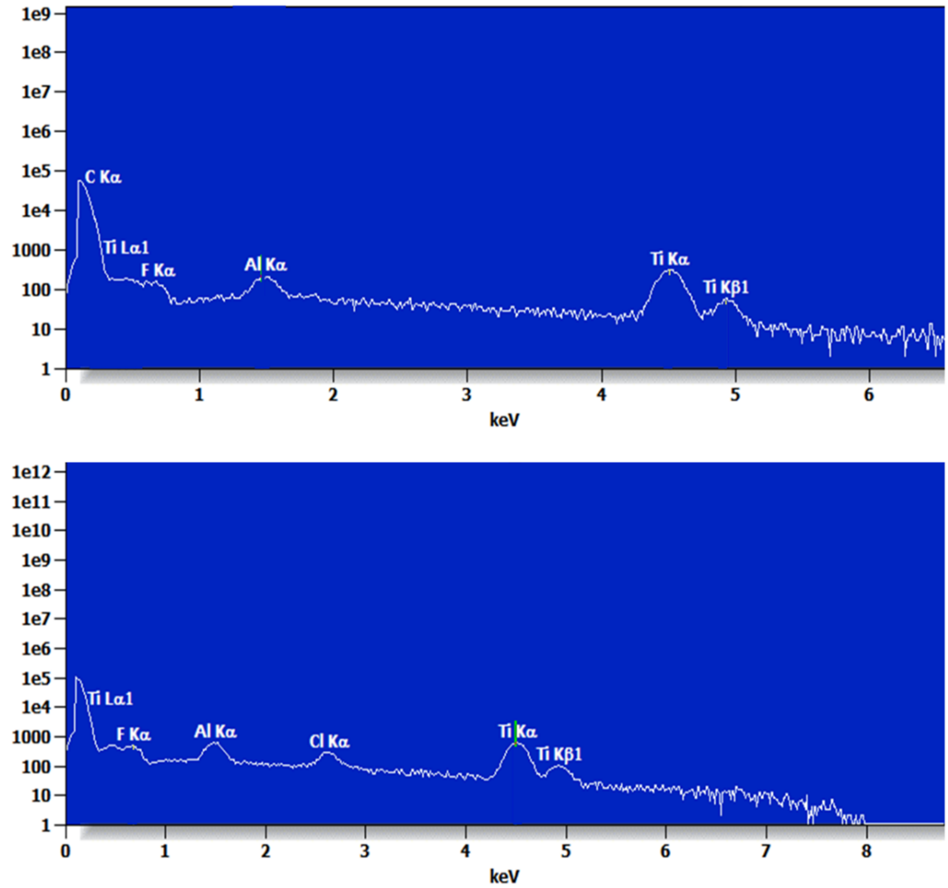

Figure 18. SEM-ED spectra of Ti_3C_2 (a) and m-Ti_3C_2 (b). The SEM-ED spectra were measured by Lennart Singer.

3.2.2.2. Electrochemical characterization

CV and GCPL were conducted to study the lithium storage performance of Ti_3C_2 and m-Ti_3C_2-based electrodes. CV curves at a scan rate of 0.1 mV s^{-1} and in a potential range of 0.01–3 V vs. Li/Li^+ for Ti_3C_2 and m-Ti_3C_2 are presented in Figures 19a, b, respectively. In the CV curve of Ti_3C_2, there are four reduction peaks during the first cathodic sweep. The reduction peaks at 1.6 and 0.9 V can be ascribed to the lithiation of Ti_3C_2 [131, 132]. The reduction peaks at 0.7 V and 0.3 V which disappear in the subsequent cycles correspond to the formation of the solid electrolyte interphase (SEI) and irreversible electrochemical reactions, which might arise from impurities e.g. Ti_3AlC_2. In the first anodic sweep, two oxidation peaks at 1.0 and 2.3 V can be observed, which are related to the delithiation process of Ti_3C_2 [131, 132]. However, reduction peaks ascribed to lithium insertion into Ti_3C_2 in the second cycle do not match well with that in the fifth cycle, which might be due to the incomplete exfoliation and the existence of multiple surface groups.

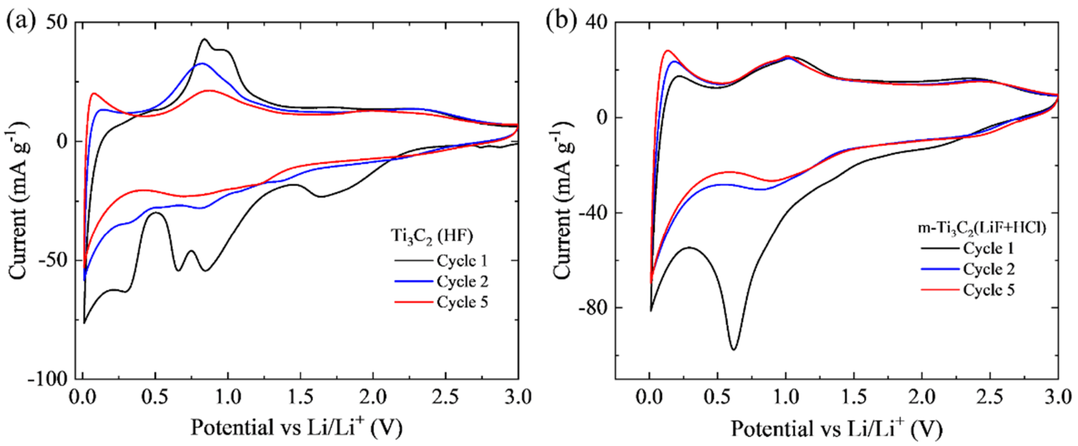

Figure 19. CV curves of Ti_3C_2 (a) and m-Ti_3C_2 (b) electrodes for the first, second, and fifth cycles at a scan rate of 0.1 mV s^{-1} and in a potential range of 0.01–3 V vs. Li/Li^+ [125].

For the m-Ti_3C_2 electrode, two broad reduction peaks at 1.4 and 2.1 V, corresponding to the lithium ions insertion into Ti_3C_2, and one sharp reduction peak at 0.6 V, which is attributed to the formation of SEI, can be observed in the first cathodic sweep [131, 132]. There are two oxidation peaks at 1.0 and 2.4 V ascribed to the extraction of lithium ions from Ti_3C_2 during the first anodic scan [131, 132]. The second and fifth CV profiles are mostly overlapping, implying high reversibility of Li ion storage in the m-Ti_3C_2 electrode. The difference between the CV curves of Ti_3C_2 and m-Ti_3C_2 can be explained by several reasons: 1) m-Ti_3C_2 and Ti_3C_2 have different surface functional groups which might change their electrochemical behavior [48]. 2) The better exfoliation of m-Ti_3C_2 causes fewer precursor Ti_3AlC_2 left and more open structure, which might introduce less irreversible electrochemical reactions and therefore active sites change of lithiation and delithiation of Ti_3C_2.

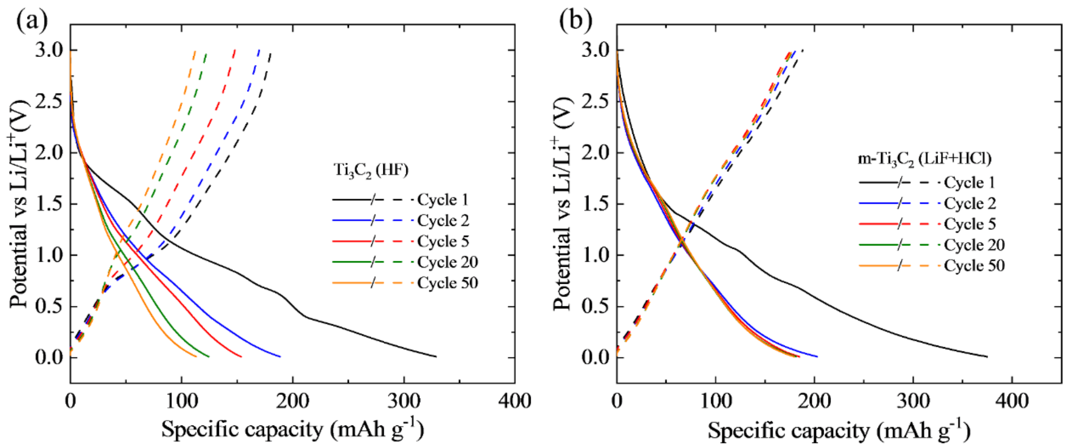

Figure 20. Galvanostatic charge/discharge curves of the Ti_3C_2 (a) and m-Ti_3C_2 (b) electrodes at a current density of 100 mA g^{-1} for the specific cycles [125].

Figure 20 shows the charge/discharge curves of the synthesized Ti_3C_2. The Ti_3C_2 and m-Ti_3C_2 electrodes deliver an initial discharge/charge capacity of 325/172 mAh g^{-1} and 372/188 mAh g^{-1}, respectively.

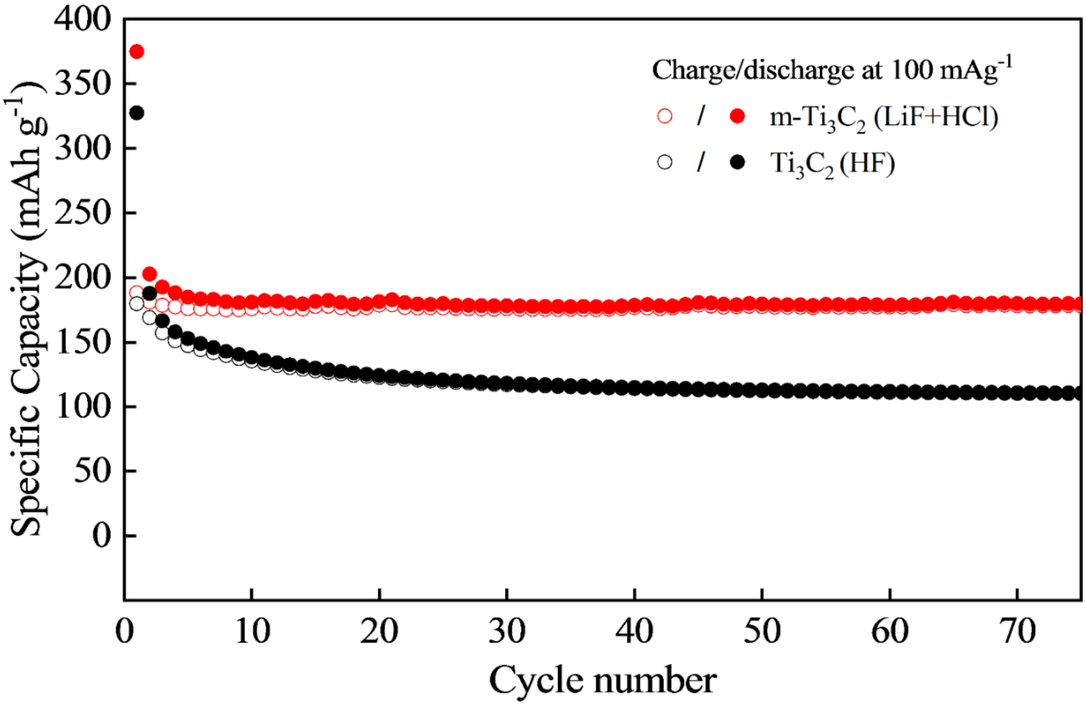

Figure 21. Cycling performance of Ti_3C_2 and m-Ti_3C_2 electrodes at a current density of 100 mA g^{-1} in the range of 0.01-3.00 vs. Li/Li^+ [125]. Hollow and solid circles stand for charge and discharge capacities, respectively.

The cycling performances of Ti_3C_2 and m-Ti_3C_2 are presented in Figure 21 and have been measured at a current density of 100 mA g^{-1}. The Ti_3C_2 electrode exhibits a significant capacity decrease in the first 30 cycles and remains stable in the following 40 cycles, exhibiting a specific discharge capacity of 112 mAh g^{-1}. By comparison, the m-Ti_3C_2 electrode shows excellent cycling stability (98% capacity retention) after 70 cycles which still exhibits a reversible capacity of 185 mAh g^{-1}.

3.2.2.3. Discussion

In the context of the above results, it is worth noting that the m-Ti_3C_2 electrode exhibits higher specific capacity and better cyclability than the Ti_3C_2 electrode. It can have several reasons. Compared with Ti_3C_2, the larger interlayer distance of m-Ti_3C_2 can ensure easier lithium ion transport, which benefits the reversible lithiation and delithiation of Ti_3C_2, leading to better cycling stability. According to other reports, the presence of F surface group in Ti_3C_2 could cause low capacity [130, 48]. For m-Ti_3C_2, there are two kinds of groups on the surface, F and Cl. The existence of Cl might lead to the observed enhanced capacity. Furthermore, better exfoliation and fewer impurities in m-Ti_3C_2 could also be a possible reason for the higher capacity of the m-Ti_3C_2 electrode.

In summary, compared with the conventional method (HF solution), the mixed solution (LiF+HCl) and hydrothermal environment process can produce a higher-quality MXene with better battery performance. Besides, more work might be done to investigate the effects of specific experimental conditions like hydrothermal temperature, hydrothermal time, and different intercalated agents on the battery performance of final products.

3.2.3. V_2C for lithium ion battery application

3.2.3.1. Physical characterization

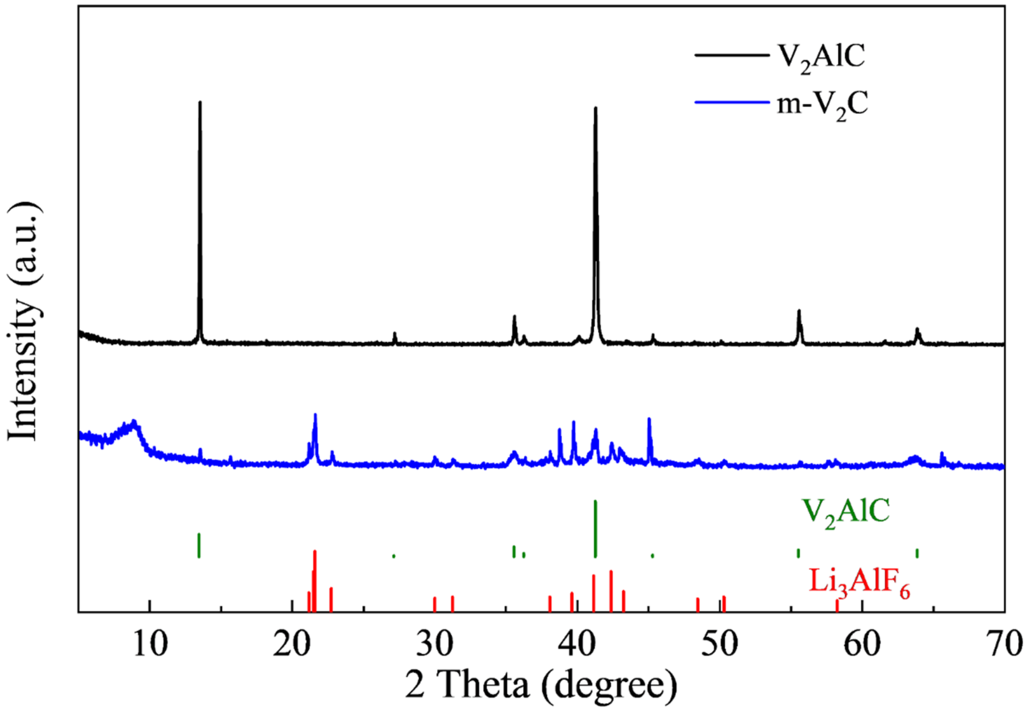

Figure 22. XRD patterns of V_2AlC and m-V_2C. Vertical ticks show the reference pattern of V_2AlC and Li_3AlF_6 according to ICSD code 606283 [133] and ICSD code 85171 [134], respectively.

Inspired by the results of Ti_3C_2 part, a HCl+LiF mixed solution was used to prepare m-V_2C MXene. Figure 22 shows the XRD patterns of the precursor V_2AlC and of m-V_2C. After the synthesis process, the diffraction peaks corresponding to V_2AlC significantly weaken and the peak at 8.7° ascribed to the (002) peak of V_2C occurs, suggesting the successful preparation of V_2C [121]. The appearance of extra diffraction peaks is associated with the impurity phase of Li_3AlF_6, which formed during the etching process [135]. Moreover, the typical accordion-like multilayered structure of V_2C MXene could be observed in the SEM images presented in Figures 23b, c, which is in accordance with that of Ti_3C_2 MXene.

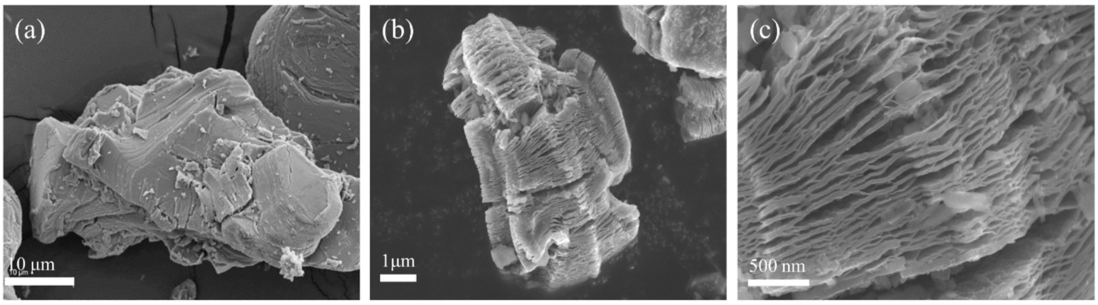

Figure 23. SEM images of V_2AlC (a) and V_2C (b, c).

3.2.3.2. Electrochemical characterization

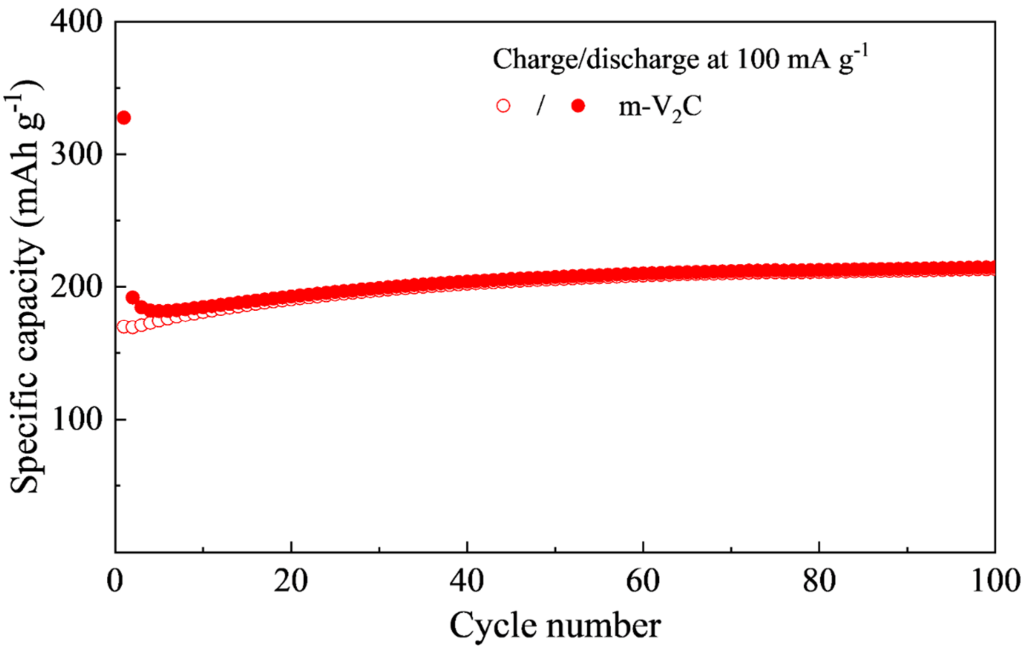

Figure 24. Cycling performance of m-V_2C electrode at a current density of 100 mA g^{-1} in the range of 0.01-3.00 V vs. Li/Li^+. Hollow and solid circles stand for charge and discharge capacities, respectively.

Figure 24 presents the cycling performance of the m-V_2C electrode at a current density of 100 mA g^{-1} in the range of 0.01-3.00 V vs. Li/Li^+. The m-V_2C electrode delivers an initial discharge/charge capacity of 327/168 mAh g^{-1} and exhibits superior cycling stability and higher specific capacity compared to that of Ti_3C_2 MXene with a reversible capacity of 212 mAh g^{-1} is attained after 100 cycles.

3.2.4. Discussion

From the above results, one can observe that both electrodes m-V_2C and m-Ti_3C_2 synthesized with a HCl+LiF mixed solution show excellent cyclability due to a good exfoliation of precursors and a large layer distance. Moreover, the m-V_2C electrode shows a higher specific capacity than that of m-Ti_3C_2 one because of more lithium insertion/extraction per unit of V_2C. However, the practically achieved capacity values are still far from their theoretical capacity (940 mAh g^{-1} for V_2C and 320 mAh g^{-1} for Ti_3C_2).

This might be explained by the existence of surface functional groups. As discussed in Tang's work, the surface group functionalized Ti_3C_2 electrode exhibits inferior battery performance compared to that of bare Ti_3C_2 because the surface group functionalization tends to degrade the Li diffusion and decrease the Li storage capacity [136]. Moreover, terminated MXenes exhibit quite different lithium storage performance i.e. the MXenes with a surface group of O and Cl can deliver higher capacity compared to that with F and OH [51, 137]. Hence, several routes have been developed to obtain MXenes with low F surface and convert the surface group of OH to O. For example, one can adopt a fluorine-free method to prepare MXenes and use the annealing process to remove the surface group of OH [49, 51]. However, the extent of improvement of surface modifications in lithium storage is still not enough. Thus, constructing composite MXenes with high-capacity anode materials is still necessary for its further battery applications.

3.2.5 Conclusion

In summary, two types of MXenes were fabricated via HF and mixed HCl+LiF solution etching. Both synthesized Ti_3C_2 MXene and V_2C MXene show the accordion-like structures. Particularly, the m-Ti_3C_2 derived from the mixed HCl+LiF solution method exhibits more open structures and fewer impurities compared with the counterpart obtained from the HF etching method. When used as anode materials for LIB, both Ti_3C_2 MXene and V_2C MXene exhibit outstanding cycling stability and the V_2C MXene shows a higher specific capacity.

3.3. Nb_2C and MoO_3/Nb_2C composites for lithium ion battery application

This chapter reports on the physical and electrochemical properties of commercial MoO_3 and synthesized Nb_2C. In addition, a ball-milling method was applied to prepare MoO_3/Nb_2C composites. In order to realize better lithium storage performance of these composites, key synthesis conditions (ball-milling speed, ball-milling time, and the mass ratio of both components) were optimized. The electrochemical characterizations were done by Yannis Riedel under the supervision of the author [138].

3.3.1. Synthesis of MoO_3/Nb_2C composites

Firstly, m-Nb_2C was synthesized by the LiF+HCl-assisted etching method (see 3.1.1 for details). Synthesized m-Nb_2C (200, 100, and 50 mg) and 100 mg of commercial MoO_3 (Sigma Aldrich, 99.5% purity) were added to a 50 ml grinding jar with grinding balls (ZrO_2, Φ1mm). Afterward, 30 ml of isopropanol was slowly added to the grinding jar. The grinding jar is then transferred to the rotating shell and fixed. The parameters including the ball milling time (6, 24h), the ball milling speed (200, 300, and 400 rpm), and the mass ratio of MoO_3 to Nb_2C (2:1, 1:1, 1:2) were set according to distinct synthesis requirements. After the ball milling process, the sample is collected by washing it with solvents and dried in vacuum at 60 °C for 12h. For the ball-milled MoO_3 and ball-milled Nb_2C, either pristine MoO_3 or pristine Nb_2C were used under the same synthesis conditions.

3.3.2. Nb_2C for lithium ion battery application

3.3.2.1. Physical characterization

Figure 25 displays the XRD patterns of Nb_2AlC, m-Nb_2C, and ball-milled Nb_2C. The diffraction pattern of Nb_2AlC shows two prominent peaks at 12.8° and 38.9°, ascribed to the (002) and (104) crystal planes of Nb_2AlC. After synthesis, the (104) peak of Nb_2AlC almost vanishes and a significant shift of the (002) peak can be observed due to the removal of Al and cation intercalation, implying the successful synthesis of Nb_2C [52]. The small peak (marked with a green circle) can be attributed to the presence of AlF_3 which was produced during the etching process. Weak peaks belonging to Nb_2AlC indicate the residue of Al atoms in the obtained Nb_2C, which is inevitable and common to see during the preparation of MXenes [139]. For the case of ball-milled Nb_2C, the XRD pattern is very similar to that of pristine Nb_2C. It can be concluded that the ball-milling process has no effect on the crystal structure of Nb_2C. In addition, the peaks of the Nb_2C and ball-milled Nb_2C patterns have broadened and the intensity has decreased, suggesting a reduction of crystallinity after the synthesis process.

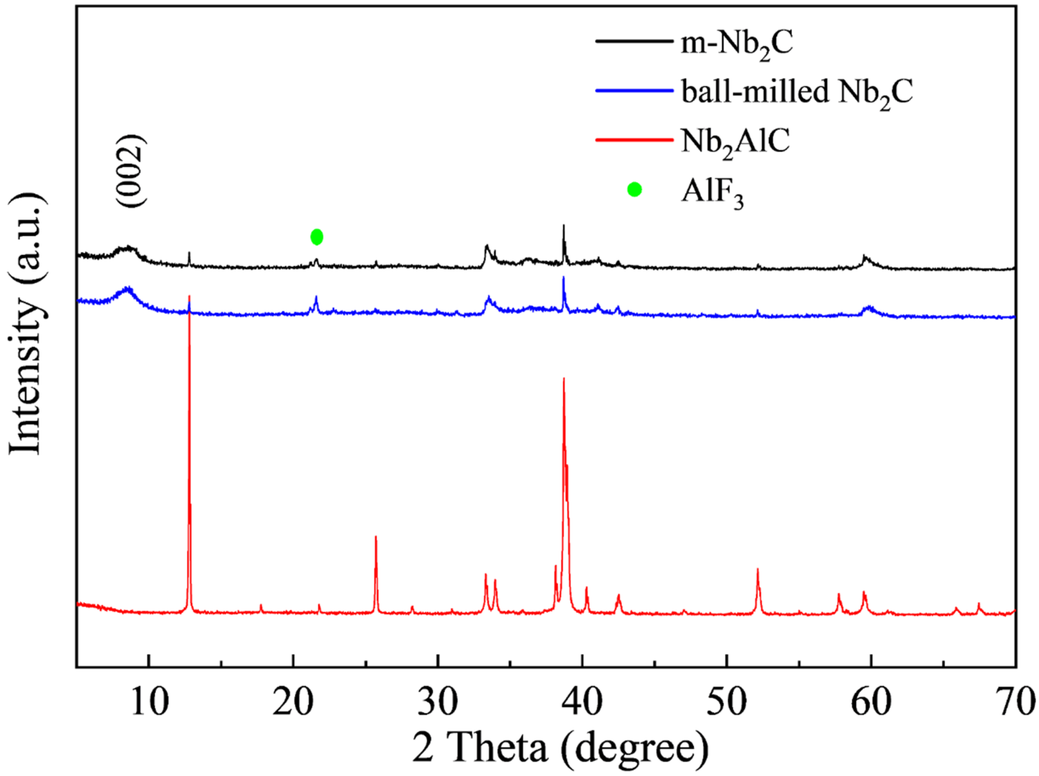

Figure 25. XRD patterns of Nb_2AlC, m-Nb_2C, and ball-milled Nb_2C. Green markers show diffraction peaks associated with an AlF_3 impurity phase.

The morphology of the Nb_2AlC, m-Nb_2C, and ball-milled Nb_2C was studied by SEM. Similar to the case of Ti_3C_2, the morphology changes from a compact structure to an accordion-like structure after the etching process (Figures 26a and 26b). Besides, the ball-milling process does not significantly affect the final morphology of Nb_2C (Figure 26c).

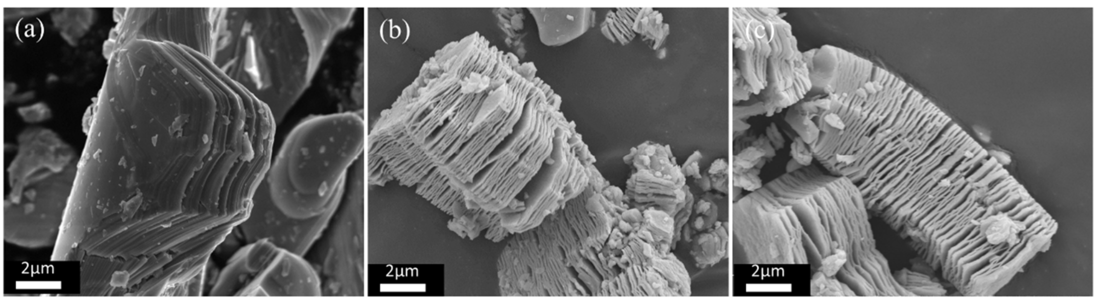

Figure 26. SEM images of Nb_2AlC (a), m-Nb_2C (b), and ball-milled Nb_2C (c).

3.3.2.2. Electrochemical characterization

In order to investigate the electrochemical behavior of m-Nb_2C, CV, and GCPL measurements were performed. Figure 27 shows the CV curve of m-Nb_2C at a scan rate of 0.1 mV s^{-1} in a potential range of 0.01V-3.00 V. In the initial cathodic scan, two reduction peaks can be observed. The reduction peak at 1.22 V corresponds to the lithiation of Nb_2C, while the peak at 0.64 V can be attributed to the formation of SEI. During the first anodic sweep, the two oxidation peaks located at 1.23 and 2.71 V are related to the delithiation of Nb_2C [140, 141]. The reduction peak in the second cathodic sweep becomes broad and shifts to 0.96V, which might arise from the structural changes due to the lithium insertion to Nb_2C in the first discharge process. The CV curves in the second and fifth cycles are mainly overlapped, indicating the reversible lithiation/delithiation of Nb_2C.

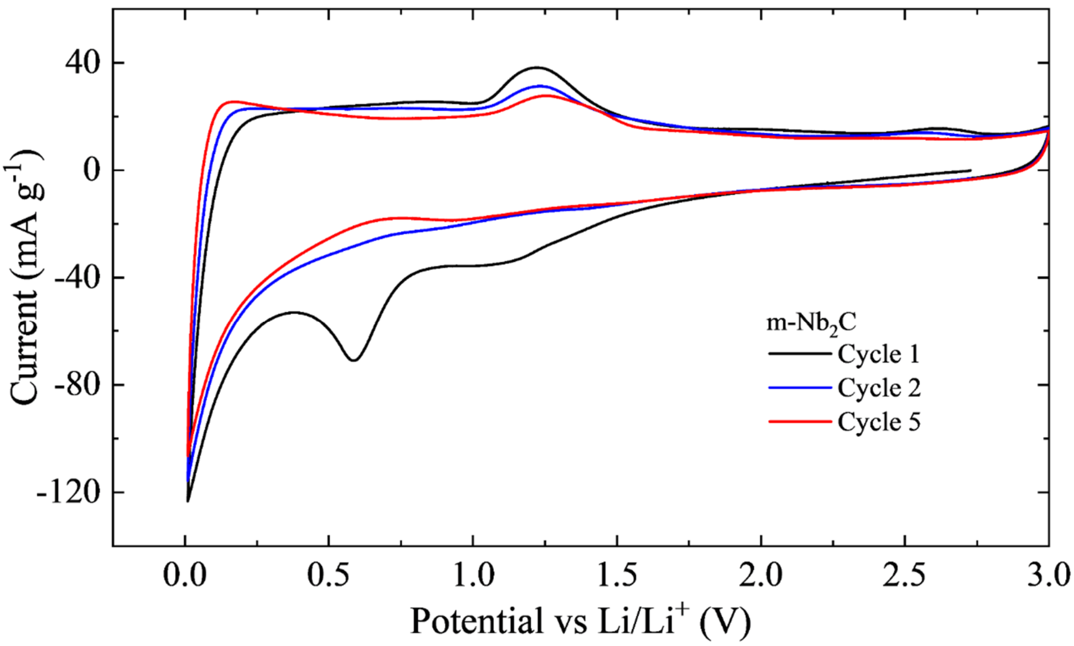

Figure 27. CV curves of m-Nb_2C at a scan rate of 0.1 mV s^{-1} and in a potential range of 0.01–3 V vs. Li/Li^+ [138].

Figure 28a shows the charge/discharge curves of the m-Nb_2C electrode at a current density of 100 mA g^{-1} for the specific cycles. The electrode exhibits initial discharge/charge capacities of 346/216 mAh g^{-1}, which brings about an initial coulombic efficiency of 62%. The voltage plateaus in the profile are also consistent with the CV results. For the cycling performance of the m-Nb_2C electrode shown in Figure 28b, a significant capacity drop in the first 15 cycles can be observed. Afterward, the capacity is maintained and shows a slight increase in the following cycles, and a discharge capacity of 162 mAh g^{-1} are achieved after 120 cycles.

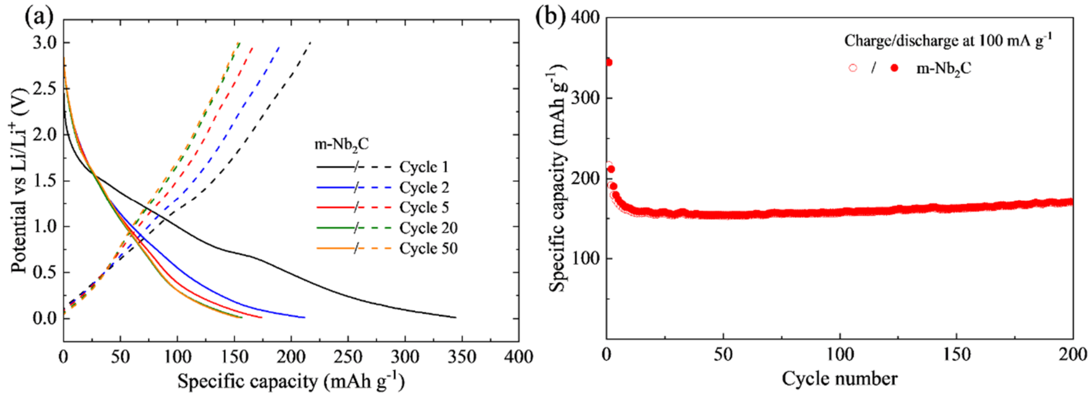

Figure 28. (a) Galvanostatic charge/discharge curves of the m-Nb_2C electrode at a current density of 100 mA g^{-1} for the specific cycles, (b) and corresponding cycling performance of the m-Nb_2C electrode [138]. Hollow and solid circles stand for charge and discharge capacities, respectively.

3.3.2.3. Discussion

The XRD pattern of Nb_2C shows the incomplete removal of Al layers after the etching process, while few Al residues were observed for the case of Ti_3C_2. It can be concluded that similar synthesis conditions adopted with different kinds of precursors (MAXs) cause MXenes with quite distinct qualities. This was also explained by studies which show that more strict conditions are required for the preparation of other MXenes than that for Ti_3C_2 due to the higher formation energies [142, 143]. Therefore, more attempts of the synthesis process might be necessary to obtain higher-quality Nb_2C. In addition, the observation that there is no effect of the ball-milling process on the crystal structure and morphology of Nb_2C makes it possible to form composites with other anode materials via the ball-milling method. The electrochemical behavior shown in the CV curves of pristine Nb_2C are consistent with other reports, in which lithiation and delithiation of Nb_2C is the main mechanism during cycling. Besides, the low capacity and excellent cycling stability of Nb_2C confirm it as a promising candidate as a substrate to support other anode materials for high-performance lithium ion storage.

3.3.3. MoO_3 for lithium ion battery application

Prior to the investigation of the composite, the following part focuses on the characterization of the commercial MoO_3 powder (Sigma Aldrich, 99.5% purity). The physical characterization starts with a comparison of the pristine MoO_3 and ball-milled MoO_3 in order to study the influence of the mechanical stress by the ball-milling on the MoO_3 crystallites. Furthermore, the ball-milled sample was investigated electrochemically.

3.3.3.1. Physical characterization

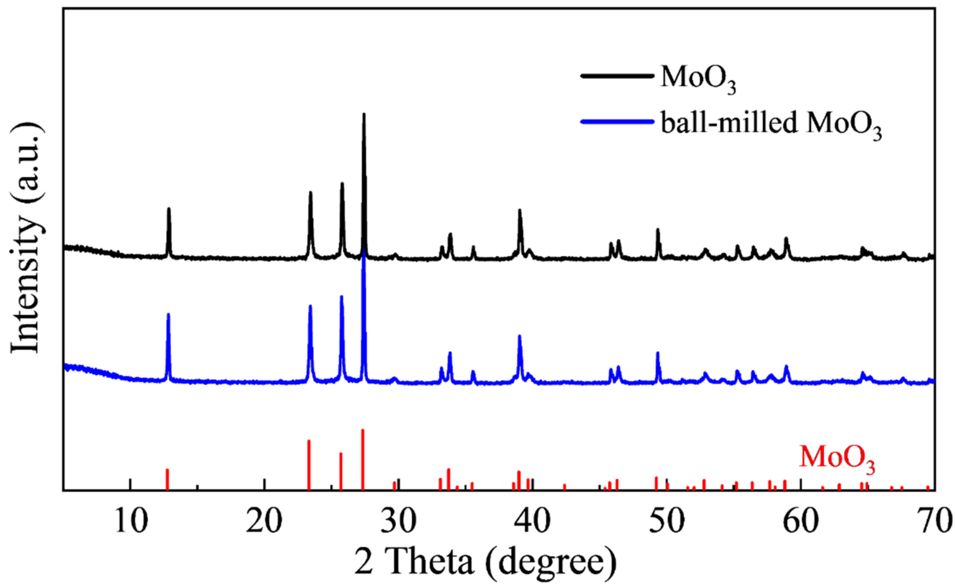

Figure 29. XRD patterns of commercial MoO_3 and ball-milled MoO_3. The vertical ticks show the reference pattern of α-MoO_3 according to ICSD code 166363 [144].

Figure 29 shows the XRD patterns of commercial MoO_3 and ball-milled MoO_3. Both patterns match well with the reference data of α-MoO_3. No extra peaks derived from impurities can be observed. Moreover, after the ball-milling process, there are no detectable peak shifts, peak broadening, or the emergence of new peaks, implying that the mechanical stress has no effect on the structure of the MoO_3 sample. The morphology of both samples was investigated by SEM (Figure 30). The commercial MoO_3 shows a structure of aggregation of microplates with sizes up to 1 µm (Figure 30a). For the ball-milled MoO_3, no obvious difference can be observed regarding the morphology after the ball-milling treatment (Figure 30b).

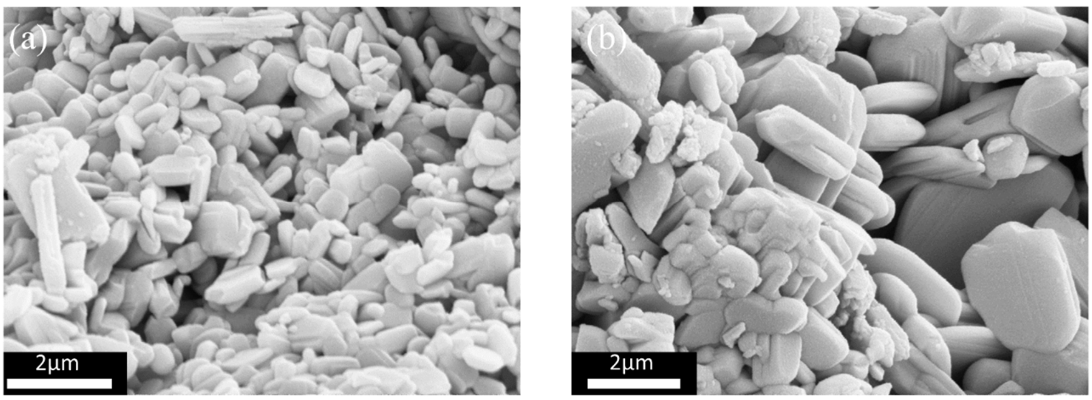

Figure 30. SEM images of commercial MoO_3 (a) and ball-milled MoO_3 (b).

3.3.3.2. Electrochemical characterization

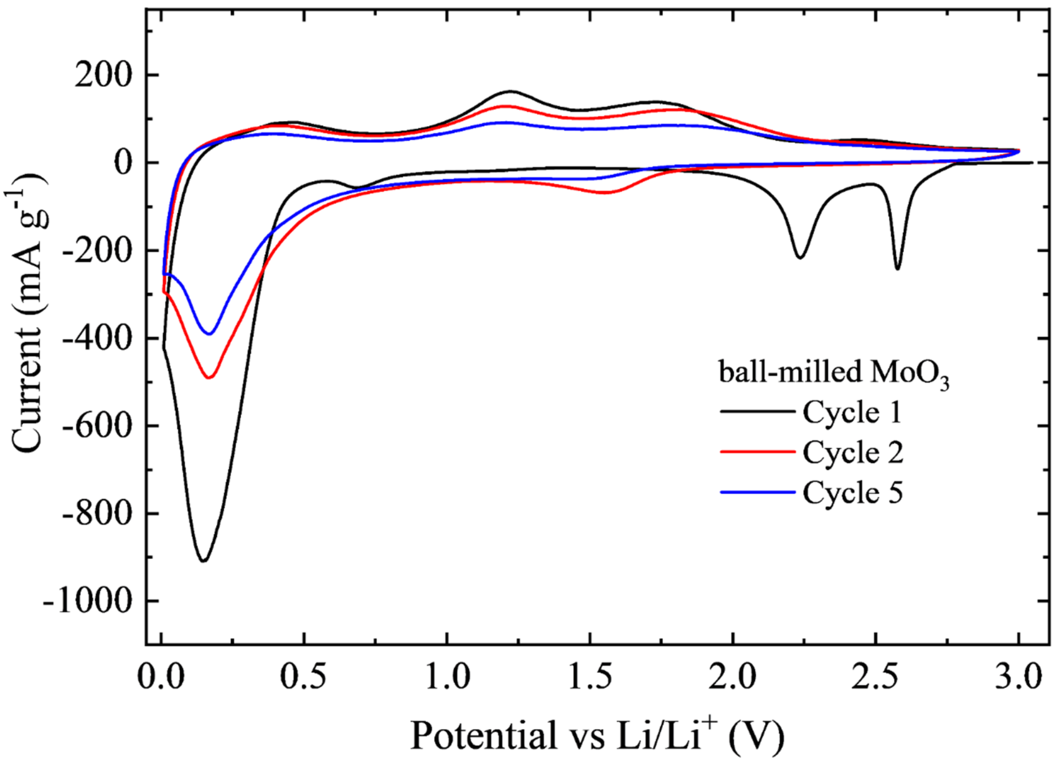

Figure 31. CV curves of ball-milled MoO_3 at a scan rate of 0.1 mV s^{-1} and in a potential range of 0.01–3 V vs. Li/Li^+ [138].

To explore the lithium storage performance of the ball-milled MoO_3, CV and GCPL measurements were carried out. The battery performance of pristine MoO_3 i.e. commercial MoO_3 is shown in Appendix. Figure 31 shows the CV curves of the ball-milled Nb_2C electrode at a scan rate of 0.1 mV s^{-1} in a potential range of 0.01–3 V vs. Li/Li^+. At the first cathodic scan, four reduction peaks could be observed. The distinct two peaks at 2.6 V and 2.25V are attributed to two steps of lithiation of MoO_3 to Li_xMoO_3 [145]. The weak reduction peak at 0.68 V, which disappears in the following cycles, corresponds to the formation of SEI [146]. The most dominant peak at 0.2 V can be ascribed to the conversion reaction of Li_xMoO_3 to metallic Mo and Li_2O [147]. In the first anodic sweep, two oxidation peaks at 1.27 V and 1.78 V could be observed, corresponding to the delithiation of Li_xMoO_3 and the formation of amorphous MoO_x. The reduction peak at 1.62 V in the second cathodic scan can be attributed to the lithiation of amorphous MoO_x [148]. The reduction peak position changes in the second cycle might be due to the different available Li sites in amorphous MoO_x. The peak current decrease in the subsequent cycle indicates the capacity drop, which might be caused by the large volume changes of MoO_3 during lithiation and delithiation.

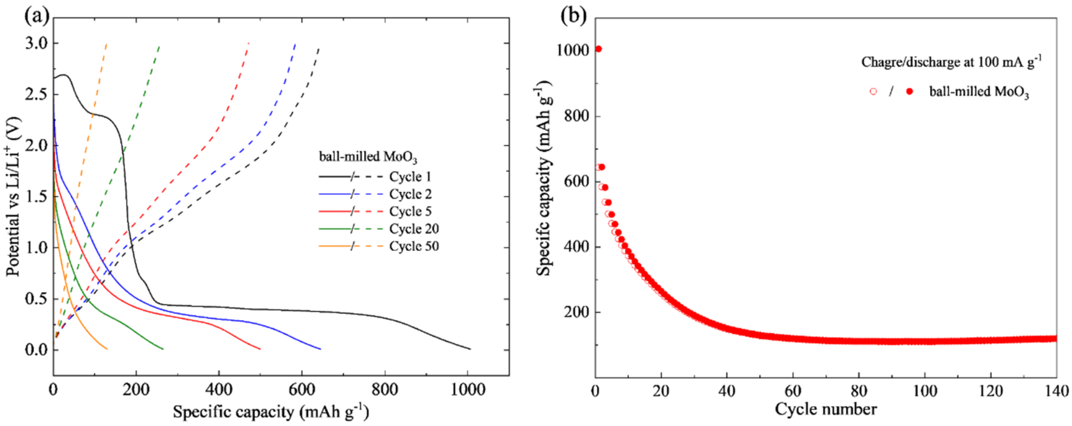

Figure 32. (a) Galvanostatic charge/discharge curves of the ball-milled MoO_3 electrode at a current density of 100 mA g^{-1} for the specific cycles, (b) and corresponding cycling performance of the ball-milled MoO_3 electrode [138]. Hollow and solid circles stand for charge and discharge capacities, respectively.

The charge-discharge curves and cycling performance of ball-milled MoO_3 are shown in Figure 32 at a current density of 100 mA g^{-1}. The MoO_3 electrode exhibits an initial discharge/charge capacity of 1006/643 mAh g^{-1}. The large capacity difference mainly arises from the formation of SEI. The voltage plateaus in the first cycle are obvious and in accordance with the CV result. However, a tremendous capacity decrease to 145 mAh g^{-1} can be found in the first 40 cycles and then the capacity remains stable in the following cycles.

3.3.3.3. Discussion

Similar to the case of Nb_2C, the ball-milling process also shows no effect on the crystal structure and morphology of MoO_3. Nevertheless, unlike Nb_2C, the MoO_3 electrode exhibits high initial specific capacities but shows fast capacity fading. Hence, a rational design to combine the advantages of both materials could be an effective strategy to realize enhanced lithium storage.

3.3.4. MoO_3/Nb_2C composites for lithium ion battery application

In consideration of the above inferior electrochemical behaviors of the pristine MoO_3 and Nb_2C, the ball-milling process as a simple and low-cost method was introduced to prepare MoO_3/Nb_2C composites of m-Nb_2C and commercial MoO_3. The effect of various ball-milling speeds, ball-milling times, and the mass ratio of both components on the crystal structure, morphology, and lithium storage performance of the final products was investigated.

3.3.4.1. Ball-milling speed

The variation of the ball-milling speed was first studied, while the ball-milling time and mass ratio were set at 6 h and 2:1 MoO_3:Nb_2C, respectively. Rotation speeds of 200 rpm, 300 rpm, and 400 rpm were adopted and the obtained composites are denoted as 200-MoO_3/Nb_2C, 300-MoO_3/Nb_2C, and 400-MoO_3/Nb_2C, respectively.

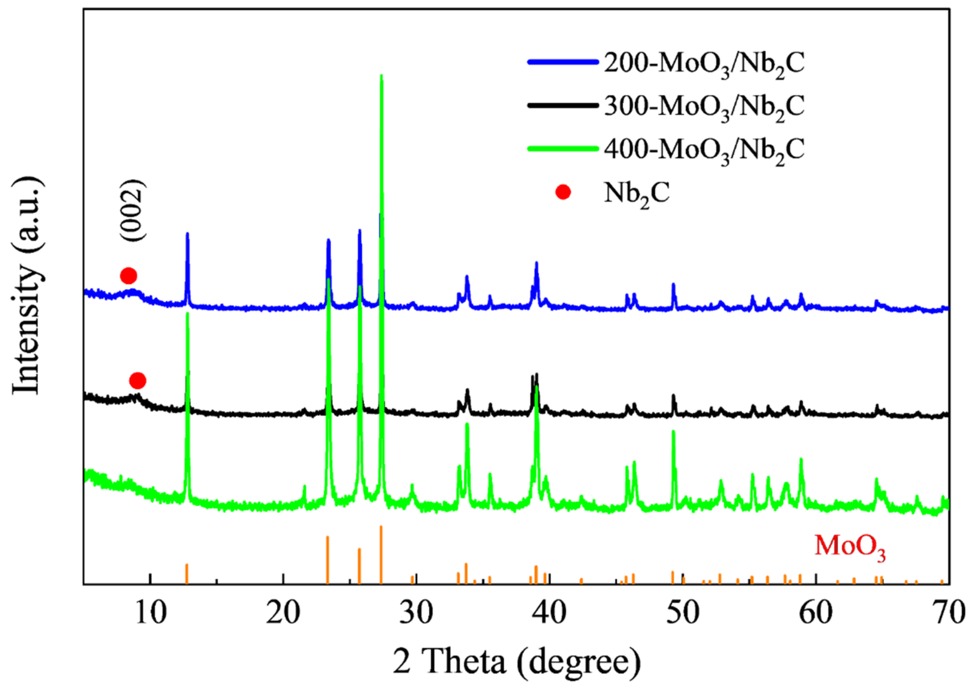

Figure 33. XRD patterns of 200-MoO_3/Nb_2C, 300-MoO_3/Nb_2C, and 400-MoO_3/Nb_2C. The red circle presents the diffraction peak corresponding to the (002) plane of Nb_2C. The vertical ticks show the reference pattern of α-MoO_3 according to ICSD code 166363 [144].

Figure 33 shows XRD patterns of 200-MoO_3/Nb_2C, 300-MoO_3/Nb_2C, and 400-MoO_3/Nb_2C. All diffraction peaks above 10° are in line with that of the reference data of α-MoO_3. In addition, a broad peak at 8.7° corresponding to the (002) plane of Nb_2C can be observed in the patterns of 200-MoO_3/Nb_2C, 300-MoO_3/Nb_2C, indicating the existence of Nb_2C. However, this peak is not detectable in the pattern of 400-MoO_3/Nb_2C. This can be due to the large shearing force at a high ball-milling speed, which might damage the MXene structure in the c-direction. The SEM image of 400-MoO_3/Nb_2C (Figure 34c) also confirms that the layered structure is not visible in this sample. By contrast, 200-MoO_3/Nb_2C and 300-MoO_3/Nb_2C still show clear Nb_2C open structures and were partially embedded and surrounded by MoO_3 particles (Figures 34a, b).

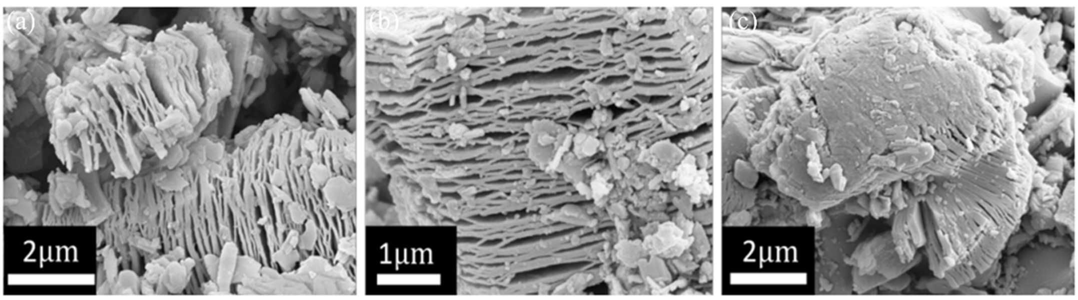

Figure 34. SEM images of 200-MoO_3/Nb_2C (a), 300-MoO_3/Nb_2C (b), and 400-MoO_3/Nb_2C (c).

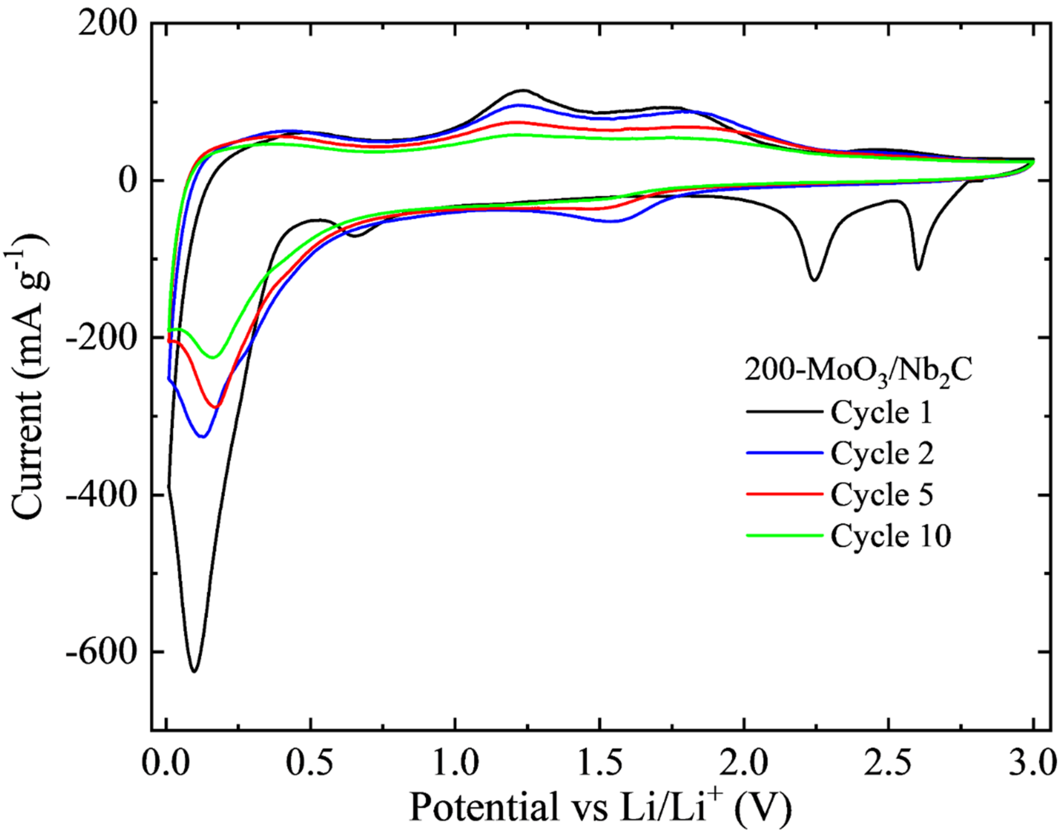

Figure 35. CV curves of the 200-MoO_3/Nb_2C electrode at a scan rate of 0.1 mV s^{-1} in a potential range of 0.01–3 V vs. Li/Li^+ [135].

Since the shape of the CV curves of 300-MoO_3/Nb_2C and 400-MoO_3/Nb_2C (see Appendix) are similar, only the CV curve of 200-MoO_3 /Nb_2C is shown in Figure 35. The CV profile is mostly consistent with that of commercial MoO_3. The extra oxidation peak at 2.63 V might be related to the delithiation of Nb_2C. However, the peak corresponding to the lithiation of Nb_2C (around 1.22 V) is not detectable from the CV curve. One possible explanation is that the peak is too broad and is merged with the peak related to the lithiation of MoO_3.

Figure 36 presents the cycling performance of composites with 200, 300, and 400 rpm as well as commercial MoO_3. The composite electrodes exhibit lower initial specific capacity than that of commercial MoO_3, which is caused by the introduction of low-capacity Nb_2C. However, no significant improvement in capacity retention is found after forming composites. Moreover, changes in ball-milling speed make no difference in the cycling stability of the composites.

Since the open structure of Nb_2C is of importance as the basic framework to support MoO_3, the 400 rpm milling experiment is unsuitable for this purpose due to the damage to the open structure at this speed. For the other two ball-milling speeds, XRD and SEM results show no difference. Therefore, any of them could be adopted to prepare composites. The battery performance of the above three composites indicates that the ball-milling speed is not the key parameter for making composites for better battery performance. Nevertheless, the investigation of the ball-milling speed provides us with more insight into a suitable way to make MXene composite without damaging the open structure.

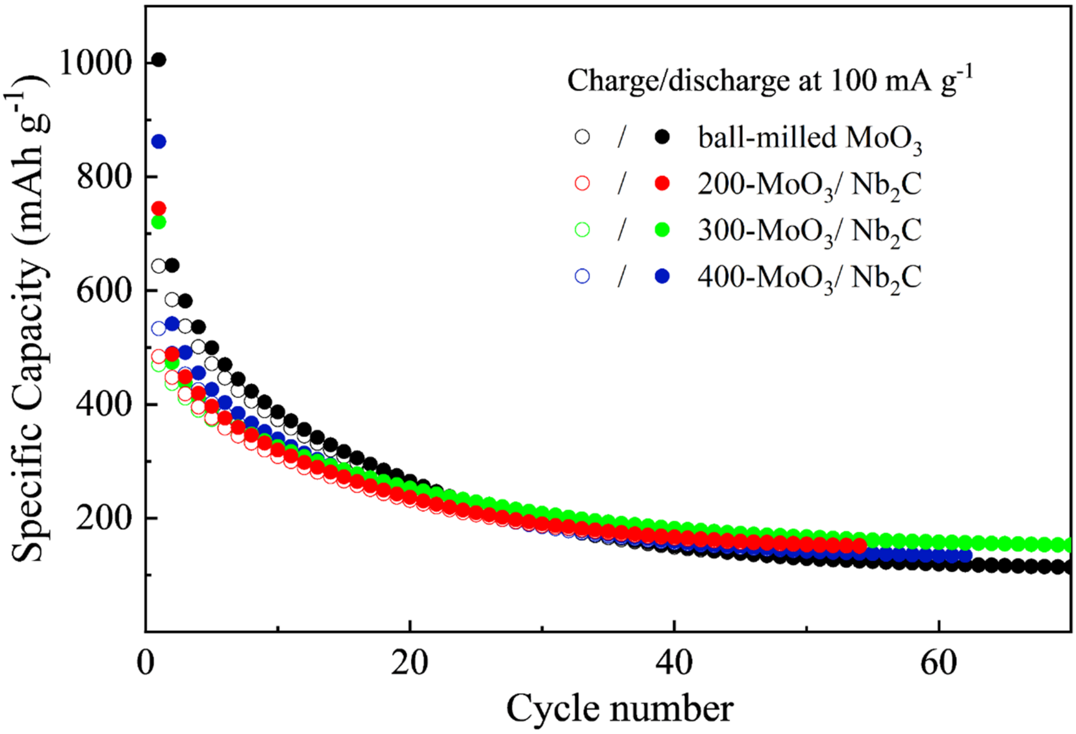

Figure 36. Cycling performance of 200-MoO_3/Nb_2C, 300-MoO_3/Nb_2C, and 400-MoO_3/Nb_2C electrodes at a current density of 100 mA g^{-1} in a potential range of 0.01–3 V vs. Li/Li^+ [138]. Hollow and solid circles stand for charge and discharge capacities, respectively.

3.3.4.2. Ball-milling time

Different ball-milling times (6 h and 24 h) were adopted with a fixed ball-milling speed (200 rpm) and a mass ratio of MoO_3:Nb_2C 2:1. The obtained products are marked as 6 h-MoO_3/Nb_2C and 24 h-MoO_3/Nb_2C, respectively.

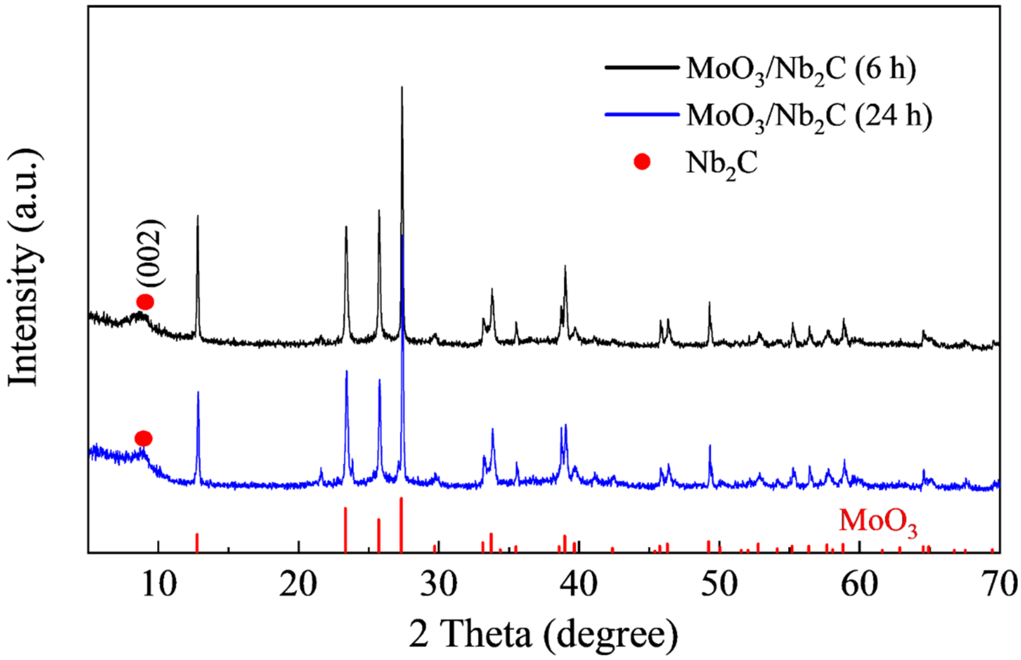

Figure 37. XRD patterns of 6h-MoO_3/Nb_2C and 24h-MoO_3/Nb_2C. The red circle presents the diffraction peak corresponding to the (002) plane of Nb_2C. The vertical ticks show the reference pattern of α-MoO_3 according to ICSD code 166363 [144].

XRD patterns of 6h-MoO_3/Nb_2C and 24h-MoO_3/Nb_2C are shown in Figure 37. Similar to the previous composites synthesized with different ball-milling speeds, the peaks of both patterns match well with the reference data of α-MoO_3 with an additional peak at 8.7°, which can be assigned to the (002) peak of Nb_2C. No impurity or peak broadening and peak shift can be discerned. The SEM images presented in Figure 38 show no clear difference between the 6h-MoO_3/Nb_2C and the 24h-MoO_3/Nb_2C. Similarly, no obvious cycling stability improvement could be found in the 6h-MoO_3/Nb_2C and 24h-MoO_3/Nb_2C electrodes (Figure 39). The CV curves and galvanostatic charge/discharge curves of the 6h-MoO_3/Nb_2C and 24h-MoO_3/Nb_2C electrodes are presented in Appendix.

From the physical and electrochemical characterization of MoO_3/Nb_2C with different ball-milling times, one can find that a longer ball-milling time will not change the morphology and structure of the obtained composites and thus could hardly improve their battery performance. Therefore, the ball-milling time of 6h is enough for the synthesis process and more time is not necessary.

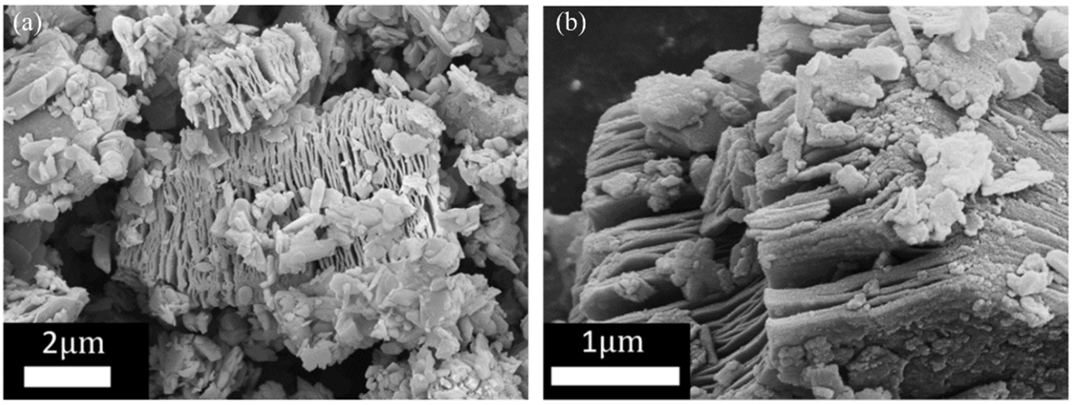

Figure 38. SEM images of MoO_3/Nb_2C (6h) (a), and MoO_3/Nb_2C (12h) (b).

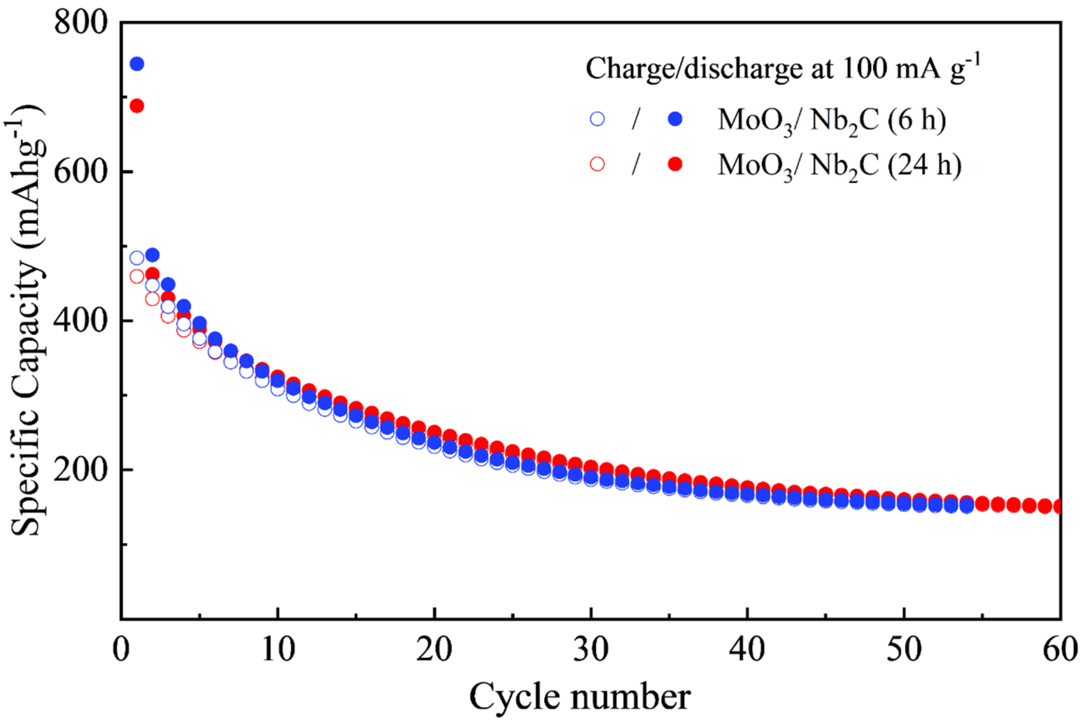

Figure 39. Cycling performance of the MoO_3/Nb_2C (6 h) and MoO_3/Nb_2C (12 h) electrodes at a current density of 100 mA g^{-1} in a potential range of 0.01–3 V vs. Li/Li^+ [138]. Hollow and solid circles stand for charge and discharge capacities, respectively.

3.3.4.3. Variation of precursor mass ratio

Based on previous investigations of ball-milling time and ball-milling speed, the effect of the mass ratio of MoO_3 and Nb_2C is studied. Here, the ball-milling time and ball-milling speed are fixed to 6 h and 200 rpm respectively, and the mass ratio of MoO_3 to Nb_2C was varied between 2:1, 1:1 and 1:2. The composites are denoted as a-MoO_3/Nb_2C, where a is the mass ratio employed.

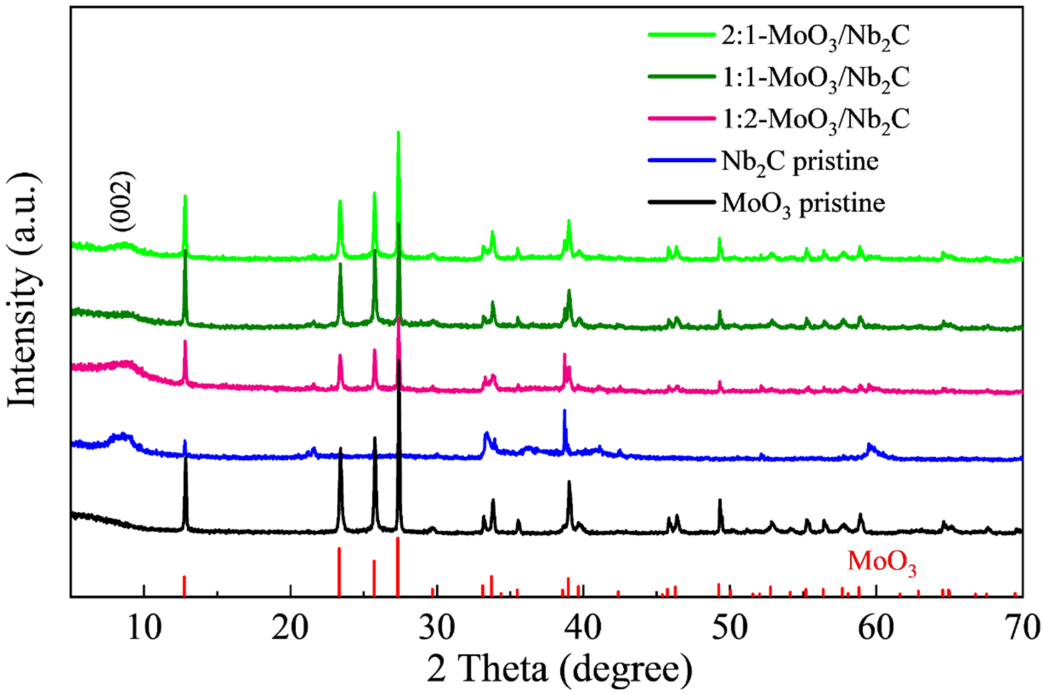

Figure 40. XRD patterns of commercial MoO_3, pristine Nb_2C, and MoO_3/Nb_2C composites with mass ratios 2:1, 1:1, and 1:2. The vertical ticks show the reference pattern of α-MoO_3 according to ICSD code 166363 [144].

Figure 40 shows the XRD patterns of commercial MoO_3, pristine Nb_2C, and MoO_3/Nb_2C composites with mass ratios 2:1, 1:1, and 1:2. The XRD patterns of the composites present diffraction peaks belonging to Nb_2C and MoO_3, which is in accordance with those of commercial MoO_3 and pristine Nb_2C. One difference, however, is a peak intensity variation with different mass ratios.

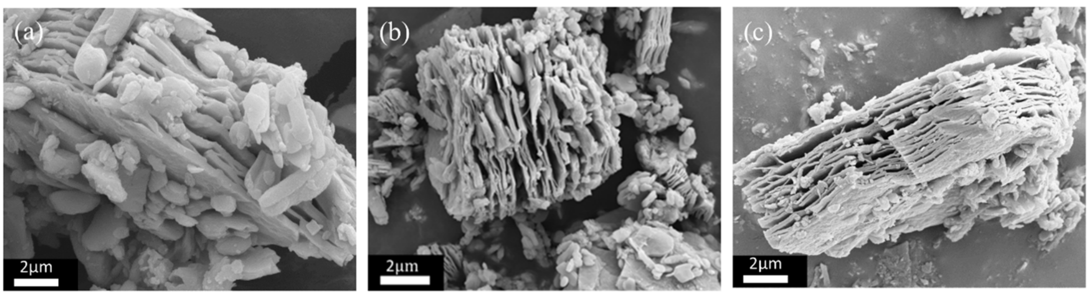

Figure 41. SEM images of 2:1-MoO_3/Nb_2C (a), 1:1-MoO_3/Nb_2C (b) and 1:2- MoO_3/Nb_2C (c).

Figure 41 depicts the SEM images of MoO_3/Nb_2C composites with mass ratios 2:1, 1:1, and 1:2. From these images, one can find that with more MoO_3 in the 2:1-MoO_3/Nb_2C composite (Figure 41a), a lot of individual MoO_3 microplates exists, which are not combined with Nb_2C. With less MoO_3 (1:2-MoO_3/Nb_2C), however, the SEM image shows that the accordion-like Nb_2C dominates and is not completely covered by MoO_3 microplates (Figure 41c). By comparison, in the case of 1:1-MoO_3/Nb_2C composite, the combination of the two components is more suitable as shown in Figure 41b where MoO_3 microplates are mainly embedded in the layered structure of Nb_2C.

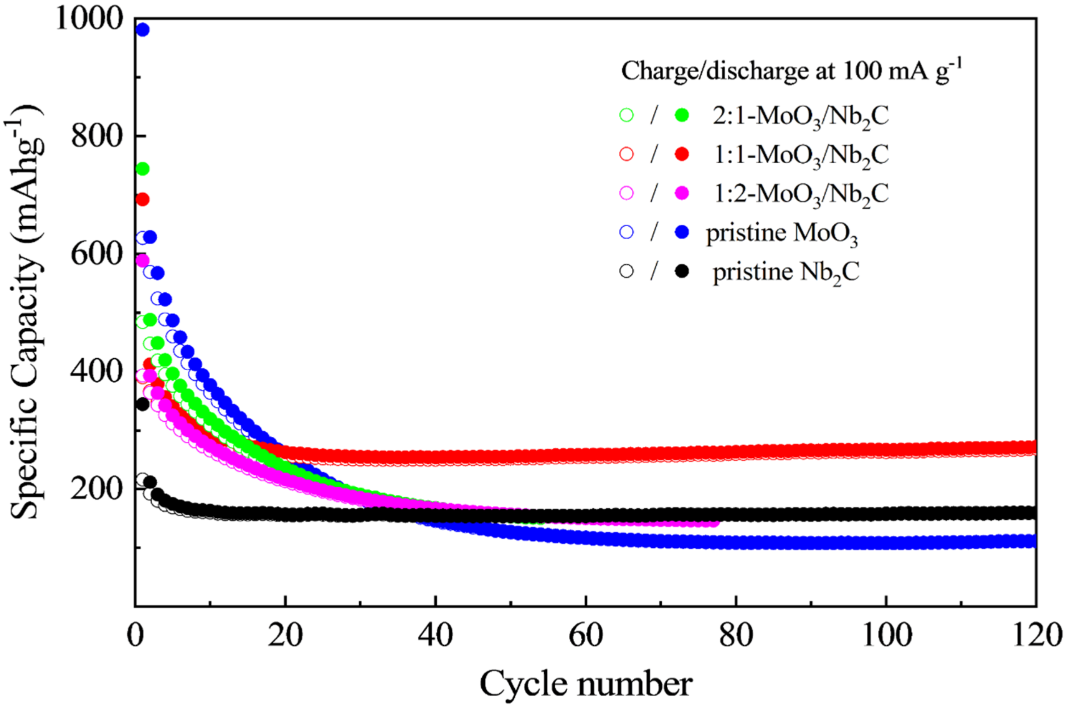

Figure 42. Cycling performance of pristine MoO_3, pristine Nb_2C, 2:1-MoO_3/Nb_2C, 1:1-MoO_3/Nb_2C, and 1:2-MoO_3/Nb_2C electrodes at a current density of 100 mA g^{-1} in the range of 0.01-3.00 vs. Li/Li^+ [138]. Hollow and solid circles stand for charge and discharge capacities, respectively.

The electrochemical performance of the MoO_3/Nb_2C composites prepared with different mass ratios of components was investigated by CV and GCPL measurements (see Appendix). Figure 42 shows the cycling stability of 2:1-MoO_3/Nb_2C, 1:1-MoO_3/Nb_2C, and 1:2-MoO_3/Nb_2C electrodes at a current density of 100 mA g^{-1} in the range of 0.01-3.00 vs. Li/Li^+. In addition, the cycling performance of pristine Nb_2C and MoO_3 were also presented as references. The 2:1-MoO_3/Nb_2C, 1:1-MoO_3/Nb_2C, and 1:2-MoO_3/Nb_2C electrodes exhibit an initial discharge/charge capacity of 746/483, 694/412, and 589/392 mAh g^{-1}. The capacity values variation is consistent with the mass ratios, i.e. with less MoO_3, the composites exhibit a lower initial capacity. Besides, the 2:1-MoO_3/Nb_2C and 1:2-MoO_3/Nb_2C electrodes exhibit similar cycling stability with that of pristine MoO_3, for which a fast capacity fading is observed in the first 50 cycles. Moreover, there is very limited improvement in the capacity value (about 40 mAh g^{-1}) compared to the pristine MoO_3 electrode.

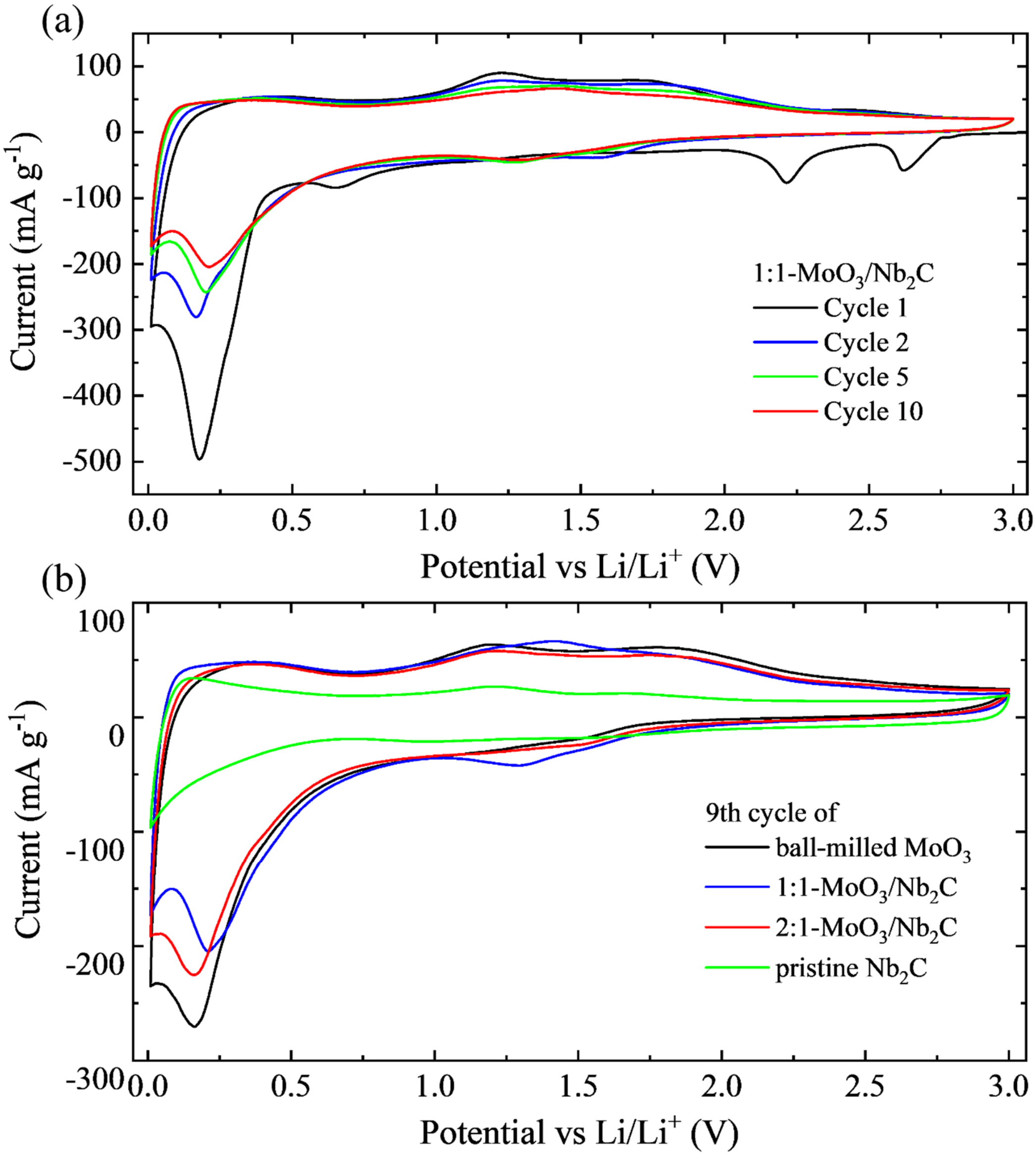

Figure 43. CV curves of the 1:1-MoO_3/Nb_2C electrode (a), and CV curves of ball-milled MoO_3, 1:1-MoO_3/Nb_2C, 2:1-MoO_3/Nb_2C, and pristine Nb_2C electrodes in the 9th cycle at a scan rate of 0.1 mV s^{-1} in a potential range of 0.01–3 V vs Li/Li^+ [138].

Figure 43a shows the CV curves of the 1:1-MoO_3/Nb_2C electrode in a voltage range from 0.01V to 3.00 V at a scan rate of 0.1 mV s^{-1}. Peaks in the first, second, and fifth cycles are consistent with those of other MoO_3/Nb_2C composites and pristine MoO_3 (see Appendix). It is worth noting that a shift in the reduction peak at around 0.22 V corresponding to the conversion reaction is observed, which is a common behavior for transition metal oxides due to the facilitated kinetics for Li^+ and O^{2-} diffusion in amorphous structures [149]. Moreover, the formation of an amorphous phase after the conversion reaction causes an enhanced Gibbs free energy compared to the crystalline bulk structures, leading to an increased lithiation potential, and this may explain the peak shift to a higher potential [150]. In addition, the 1:1-MoO_3/Nb_2C electrode exhibits a pair of prominent redox peaks at 1.31 and 1.43 V in the ninth cycle compared to other electrodes (ball-milled MoO_3, 2:1-MoO_3/Nb_2C, and pristine Nb_2C) (Figure 43b), indicating that a distinct MoO_x phase is formed and the degradation of this MoO_x is significantly suppressed due to the better confinement effect in this composite, resulting in a stable lithiation/delithiation process.

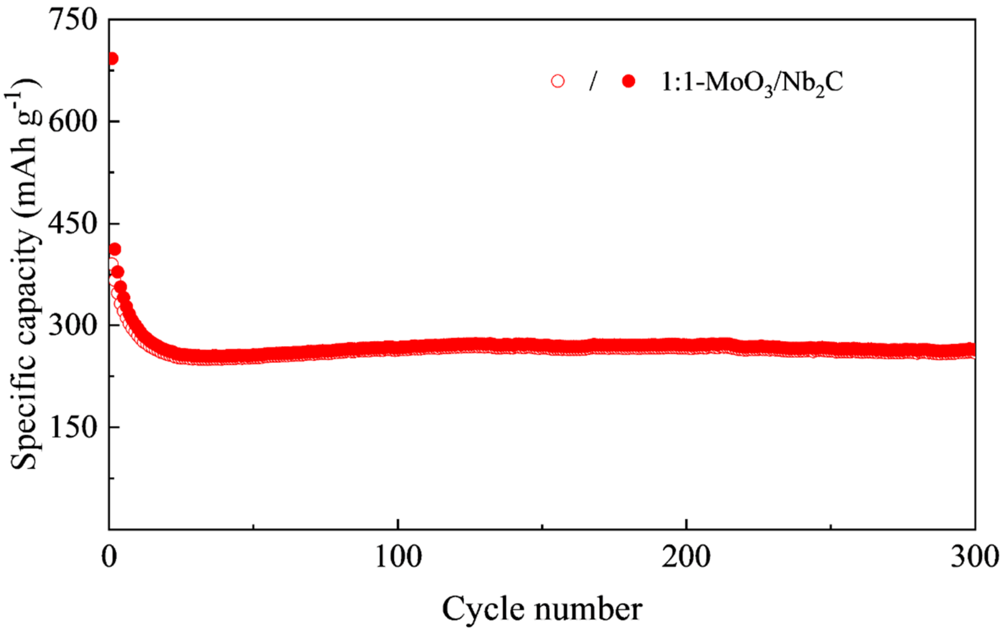

Figure 44. Long-term cycling performance of the 1:1-MoO_3/Nb_2C electrode at a current density of 100 mA g^{-1} in the range of 0.01-3.00 vs. Li/Li^+ [138]. Hollow and solid circles stand for charge and discharge capacities, respectively.

Figure 44 shows the long-term cycling stability of the 1:1-MoO_3/Nb_2C electrode at 100 mA g^{-1}. The electrode delivers a remarkable cyclability, and a reversible capacity of 267 mAh g^{-1} after 300 cycles could still be achieved, demonstrating the good combination of the two components in a mass ratio of 1:1. Moreover, the 1:1-MoO_3/Nb_2C composite displays enhanced specific capacity and cycling stability compared to the pristine MoO_3 and Nb_2C ones.

3.3.5. Discussion

Among these composites, the 1:1-MoO_3/Nb_2C composite shows the best lithium storage performance. Following the overall hypothesis motivating the synthesis of the composites, it might be because, with an optimal combination of two components in this mass ratio, the Nb_2C layered structure efficiently buffers the volume change and stabilize the amorphous MoO_x phase. However, the lower mass ratio (1:2) does not yield this positive effect. It might be because Nb_2C is not completely covered by MoO_3 microplates in this mass ratio, as suggested by the SEM images.

Moreover, a higher mass ratio (2:1) provides excessive individual MoO_3 microplates which have no combination with Nb_2C, causing large volume expansion and the formation of the unstable MoO_x phase. Both cases lead to an ineffective combination of components. It can be concluded that the rational mass ratio of two components is of importance for the lithium storage performance of composites. These results might be attributed to an oversaturation of MoO_3 in the case of 2:1 MoO_3/Nb_2C, or an undersaturation in the case of 1:2 MoO_3/Nb_2C. In the case of oversaturation, the Nb_2C structure can not completely accommodate the excessive MoO_3 microplates, resulting in the existence of many individual MoO_3 microplates of which the volume expansion during the cycling process may not be effectively alleviated. In the undersaturation case, the insufficient introduction of MoO_3 might not take full advantage of the Nb_2C structure. Additionally, the electrochemical contribution from MoO_3 is not enough, resulting in low capacity for the 1:2 MoO_3/Nb_2C composite. By contrast, the 1:1-MoO_3/Nb_2C electrode shows good capacity retention, and a reversible capacity of 272 mAh g^{-1} is achieved after 120 cycles, indicating a good combination of two components which is in accordance with the SEM result.

Although optimization of the structure and battery performance was obtained, the capacity is still not high enough for an application. One possible reason is the selection of MoO_3. The adopted commercial MoO_3 has a relatively large primary particle size of micrometers, and the composites have to be further optimized by using synthesized nanoscale MoO_3, which might more easily embed into the open structure of Nb_2C.

3.3.6. Conclusion

MoO_3/Nb_2C composites were synthesized via a simple ball-milling method. Commercial MoO_3 microplates are embedded in the open structure of Nb_2C. The lithium storage performance was enhanced by optimizing the synthesis conditions including ball-milling time, ball-milling speed, and mass ratio of components. Consequently, the MoO_3/Nb_2C composite with mass ratio 1:1 (MoO_3:Nb_2C) leads to an electrode with improved specific capacity and excellent cycling stability compared to that of pristine MoO_3 and Nb_2C: a capacity of 261 mAhg^{-1} is attained after 300 cycles at a current density of 100 mA g^{-1}.

3.4. $MoO_2/C/V_2C$ composites for lithium storage

In this Chapter, $MoO_2/C/V_2C$ composites were fabricated via an electrostatic interaction-assisted hydrothermal and a post-annealing process. The crystal structure, morphology, and chemical compositions of composites were investigated by XRD, SEM, TEM, and XPS measurements. Additionally, CV and GCPL were performed to study the lithium storage performance of their electrodes. Parts of the electrochemical study was conducted by Hinz Brian under the supervision of the author [151].

3.4.1 Synthesis of $MoO_2/C/V_2C$ composites

(1). V_2C/PDDA: The positively charged V_2C/PDDA was prepared by modifying V_2C with polydiallyldimethylammonium chloride (PDDA) solution: The V_2C was first synthesized (see 2.1 for details). Afterward, 50 mg V_2C was dispersed in 30 mL water. 1ml PDDA solution (20 wt%) was then added dropwise to the above V_2C solution under continuous stirring for 2 h.

(2). MoO_2/PDDA/V_2C: The $MoO_2/C/V_2C$ composites were prepared via a hydrothermal and annealing process. 400 or 200 mg $(NH_4)_6Mo_7O_{24}$ was added into V_2C/PDDA solution under vigorous stirring. The pH value of the solution was adjusted to 1 by addition of 9 M HCl. After that, the solution was transferred to a Teflon-lined stainless steel autoclave, sealed, and maintained at 200 °C for 12 h. The obtained precipitate was washed with water and centrifugated 3 times. Afterwards, the product was collected and dried in vacuum at 70 °C for 12 h. The product is denoted as MoO_2/PDDA/V_2C-1 or MoO_2/PDDA/V_2C-2 based on the mass ratio of the molybdenum source to V_2C (8:1 or 4:1, respectively). The products were annealed at 400 °C with argon flow for 2 h. The annealed samples were collected and marked as $MoO_2/C/V_2C$-1 or $MoO_2/C/V_2C$-2 according to the mass ratio of molybdenum source to V_2C (8:1 or 4:1, respectively).

(3). MoO_3/V_2C and MoO_2/PDDA: The MoO_3/V_2C and MoO_2/PDDA composites were synthesized with the same procedure as the MoO_2/PDDA/V_2C composites except for the addition of PDDA and V_2C MXene, respectively. The MoO_3/V_2C and MoO_2/PDDA products were annealed at 400 °C with argon flow for 2 h and denoted as MoO_3/V_2C (annealing) and MoO_2/C (annealing).

3.4.2. Experimental design

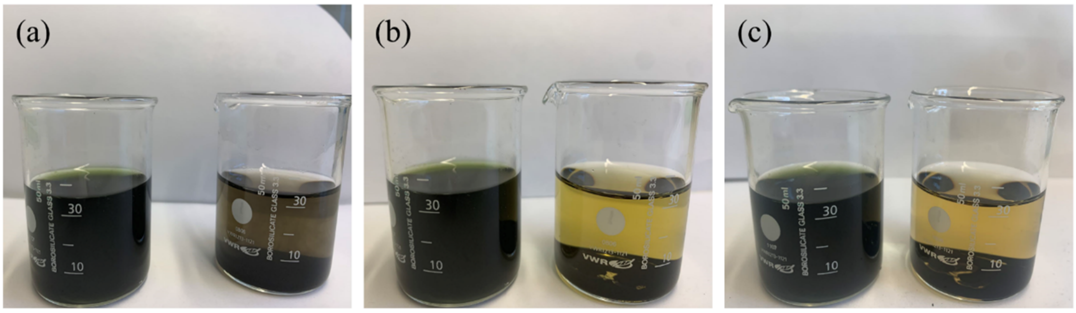

Figure 45. Photographs of dispersions of pristine V_2C MXene (right beakers) and V_2C/PDDA (left beakers) in water after 12 h (a), 24 h (b), and 72 h (c).

During the preparation process, negatively charged V_2C was first synthesized via the etching process with a mixture of HCl and LiF. Usually, synthesized V_2C shows a multilayer structure with sizes of several micrometers [152]. Therefore, it can be hardly dispersed in water, making it impossible to combine V_2C with the molybdenum source during the hydrothermal process. Instead, the PDDA, a typical water solution cationic polyelectrolyte, can be introduced to combine with V_2C by electric force, which on one hand stabilizes the V_2C dispersion in solution, on the other hand, makes V_2C positively charged for further treatment.

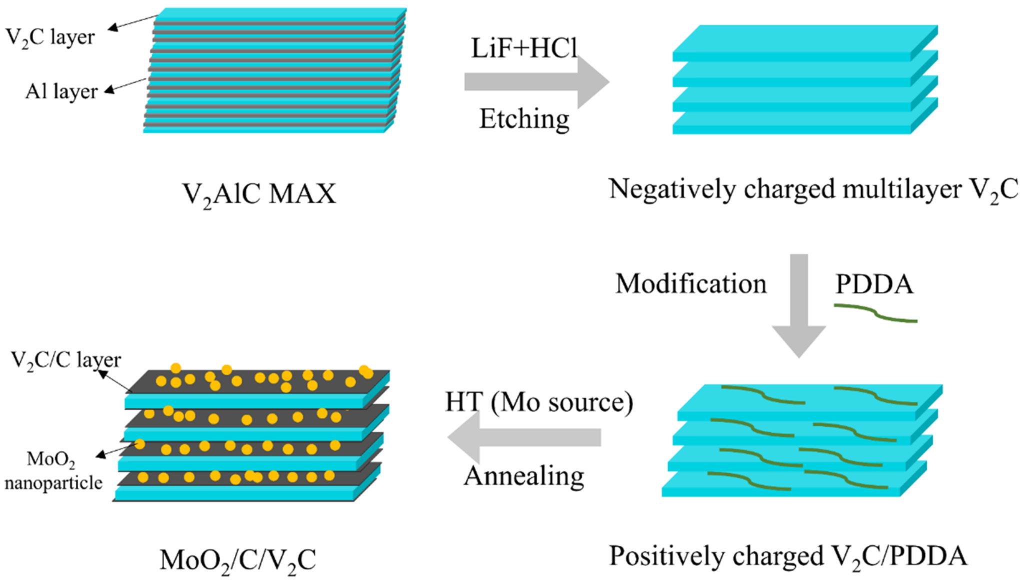

Figure 46. Schematic illustration of the preparation of $MoO_2/C/V_2C$ composites.

The stability of the synthesized multilayer V_2C MXene and V_2C/PDDA dispersions in water was evaluated (Figure 45). After 12 h, most V_2C MXene agglomerated and precipitated, and very little V_2C is dispersed, demonstrating the poor stability of V_2C MXene in water (right in Figure 45a). In contrast, the presence of PDDA in V_2C/PDDA stabilizes the V_2C MXene in water via electrostatic interaction, resulting in a stable dispersion of V_2C/PDDA in water (left in Figure 45a). The stability was maintained even after 48 and 72 h (Figures 45b, c). This improvement makes it possible to preserve the hierarchical structure and integrate it with MoO_2 for excellent lithium storage performance.

Afterwards, the positively charged V_2C/PDDA was combined with isopolymolybdate anions $Mo_7O_{24}^{6-}$ from the molybdenum source $(NH_4)_6Mo_7O_{24}$) and formed V_2C/PDDA/ $Mo_7O_{24}^{6-}$ by electrostatic interaction [152]. During the hydrothermal reaction, the hierarchical structure of MoO_2/PDDA/V_2C composites was obtained. The MoO_2/PDDA/V_2C composites were then converted to MoO_2/C/V_2C via an annealing process (Figure 46).

3.4.3. Physical characterization

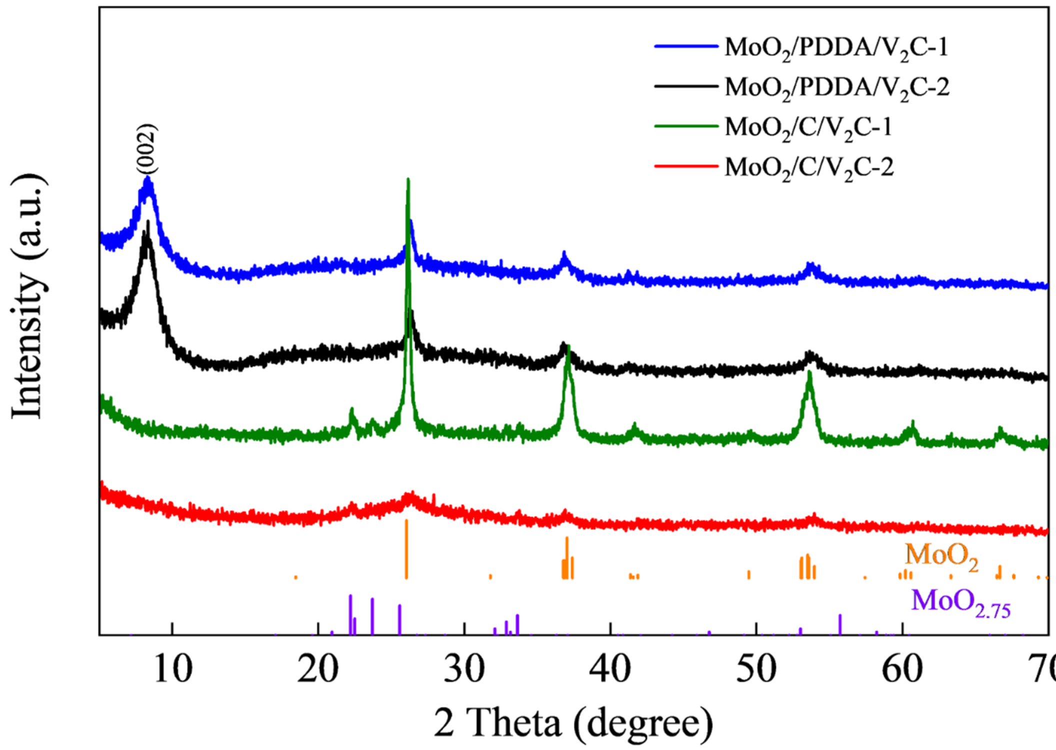

Figure 47. XRD patterns of MoO_2/PDDA/V_2C-1, MoO_2/PDDA/V_2C-2, MoO_2/C/V_2C-1, and MoO_2/C/V_2C-2. Vertical ticks show the reference patterns of MoO_2 and $MoO_{2.75}$ according to ICSD code 80830 [153] and ICSD code 201573 [154], respectively. The (002) label represents the corresponding diffraction peak related to the (002) plane of V_2C.

The structure and phase characteristics of MoO_2/PDDA/V_2C and MoO_2/C/V_2C composites are determined by XRD, as shown in Figure 47. The XRD patterns of MoO_2/PDDA/V_2C-1 and MoO_2/PDDA/V_2C-2 composites show a strong diffraction peak at 8.2° corresponding to the (002) planes of V_2C and peaks at 26.2°, 36.8°, and 53.6°, which can be ascribed to the (110), (111), and

(220) planes of monoclinic MoO_2 (ICSD code 80830). In addition, weak diffraction peaks at around 22.4°, 23.7°, and 33.6° are related to the pattern of $MoO_{2.75}$ (ICSD code 201573), indicating the existence of a small amount of impurities. By comparison, the absence of the (002) peak from V_2C MXenes in the XRD patterns of the $MoO_2/C/V_2C$-1 and $MoO_2/C/V_2C$-2 samples could be the effect of the annealing process at high temperatures, which has been reported in other works [124, 152].

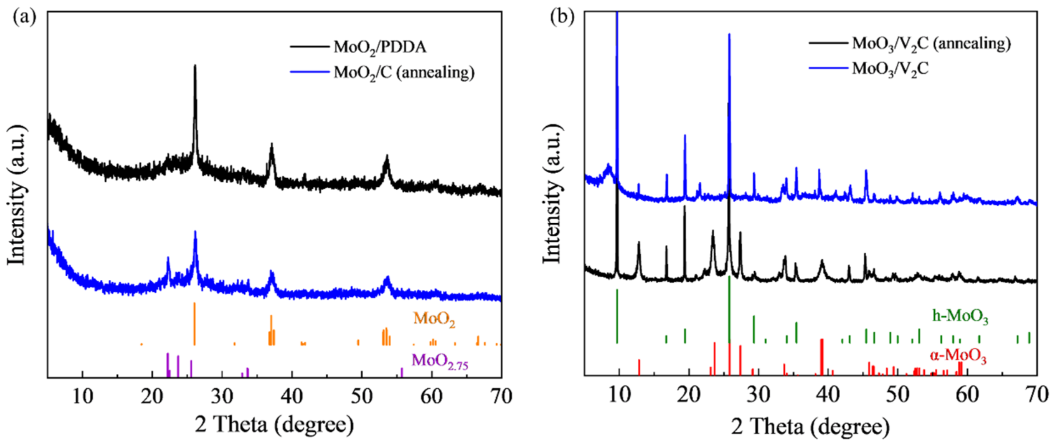

Figure 48. XRD patterns of MoO_2/PDDA and MoO_2/C (annealing) composites without the addition of V_2C MXene (a). Vertical ticks show the reference patterns of MoO_2 and $MoO_{2.75}$ according to ICSD code 80830 [153] and ICSD code 201573 [154], respectively. XRD patterns of MoO_3/V_2C and MoO_3/V_2C (annealing) without the addition of PDDA (b). Vertical ticks show the reference patterns of h-MoO_3 and α-MoO_3 according to ICSD code 80291 [155] and ICSD code 166363 [144], respectively.

In addition, in the case of $MoO_2/C/V_2C$-2, amorphous MoO_2 with poor crystallinity is observed, which might be resulting from a strong confinement effect in the composite. Compared with $MoO_2/C/V_2C$-1, more V_2C MXene in $MoO_2/C/V_2C$-2 might reduce the crystallinity of MoO_2 by increasing the depletion of the lattice oxygen atoms at high temperatures [156]. The absence of V_2C MXene leads to the production of MoO_2/PDDA and corresponding annealing-MoO_2/C samples, of which XRD pattern exhibit obvious diffraction peaks, matching well with that of monoclinic MoO_2 (Figure 48a). On this basis, it could be concluded that PDDA also works as a reducing agent during hydrothermal reactions. Consistently, the lack of PDDA results in the production of the mixed phases of h-MoO_3 and α-MoO_3 in the MoO_3/V_2C and MoO_3/V_2C (annealing) composites (Figure 48b). Moreover, the diffraction peak at 8.2° ascribed to the (002) plane of V_2C vanishes after the annealing process, in line with that of $MoO_2/C/V_2C$ samples.

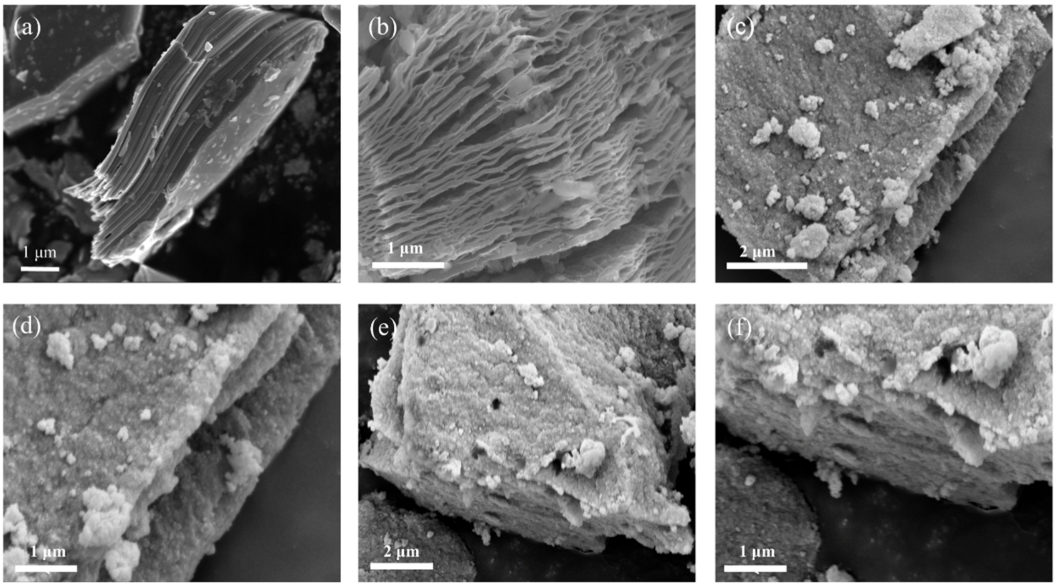

Figure 49. SEM images of V_2AlC (a), V_2C (b), $MoO_2/C/V_2C$-1 (c,d), and $MoO_2/C/V_2C$-2 (e,f).

SEM, TEM, HRTEM, and TEM-EDS measurements were performed to investigate the microstructure, the crystal structure, and element distribution of samples, respectively.

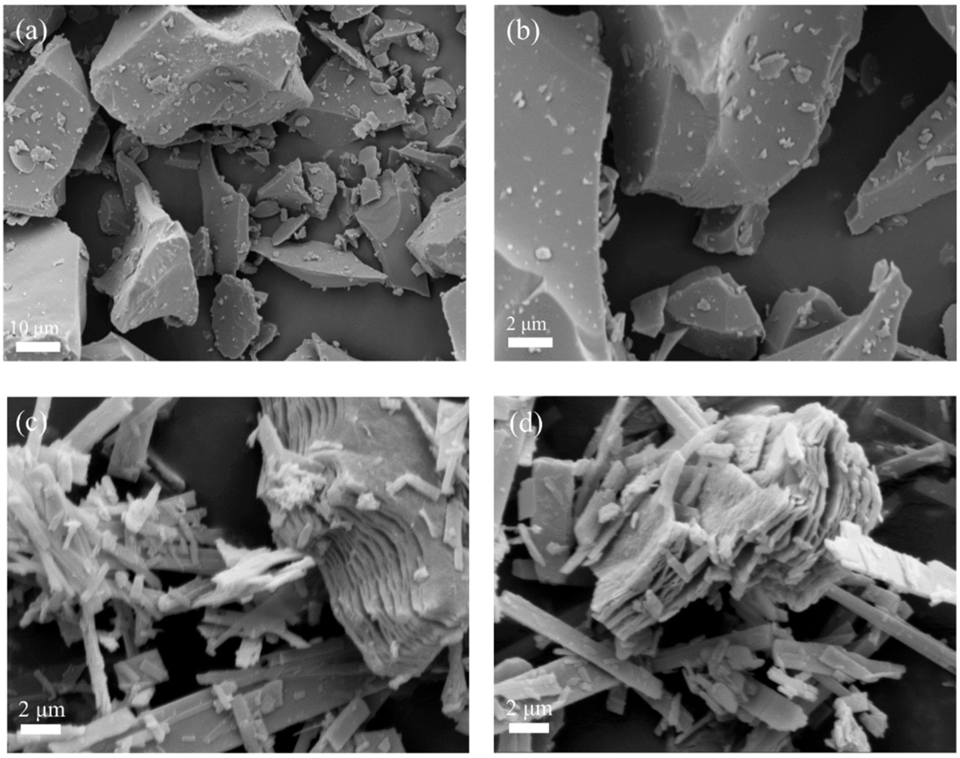

Figure 50. SEM images of MoO_2/C (annealing) composites without the addition of V_2C MXene (a, b) and MoO_3/V_2C (annealing) without the addition of PDDA (c, d).

After the etching process, compared with the precursor V_2AlC (Figure 49a), the pristine V_2C shows the typical accordion-like morphology with the multilayer structure (Figure 49b). The framework from this open structure provides sufficient channels for electrolyte penetration and reduces the migration of lithium ions. The SEM images of the $MoO_2/C/V_2C$-1 composite (Figures 49c, d) show that MoO_2 nanoparticles are distributed uniformly in the layered structure. The hierarchical structure in this composite is not clear to see due to the introduction of excessive MoO_2. In contrast, $MoO_2/C/V_2C$-2 shows a more obvious hierarchical structure because of less MoO_2 content in this composite. Nonetheless, without the participation of V_2C MXene, the synthesized MoO_2/C (annealing) composite shows the morphology of microparticles with a size of 10-20 μm (Figures 50a, b). In the absence of PDDA, the SEM images of the obtained MoO_3/V_2C (annealing) sample reveal a mixture of MoO_3 microrods and accordion-like V_2C (Figures 50c, d), demonstrating that the open structure of V_2C MXene can not be effectively utilized to confine MoO_2 in this case. Therefore, the delicate design with PDDA is indispensable for the better combination of V_2C MXene with MoO_2.

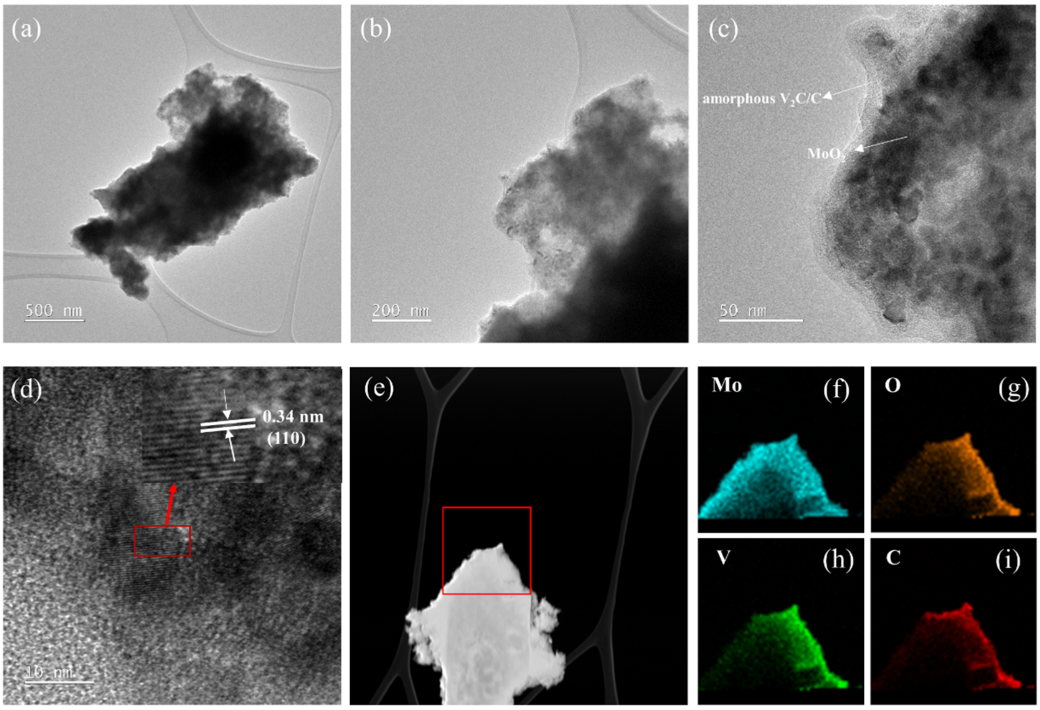

Figure 51. TEM images (a-c), HRTEM image (d), and TEM-EDS elemental mapping (e-i) of $MoO_2/C/V_2C$-1. TEM, HRTEM images, and elemental mapping were measured by Tomasz Kędzierski.

TEM images of $MoO_2/C/V_2C$-1 in Figures 51a-c show the hierarchical structure where MoO_2 nanoparticles of a size of 10-20 nm were almost uniformly confined in the amorphous V_2C/C matrix, agreeing with that of SEM results. HRTEM image of $MoO_2/C/V_2C$-1 in Figure 51d shows the lattice spacing of 0.34 nm corresponding to the (110) plane of monoclinic MoO_2, which is in accordance with the XRD results. TEM-EDS mapping (Figures 50e-i) of the selected area in Figure 51d (red rectangle) confirm the homogeneous distribution of Mo, O, V, and C, indicating sufficient loading of MoO_2 nanoparticles in this hierarchical composite.

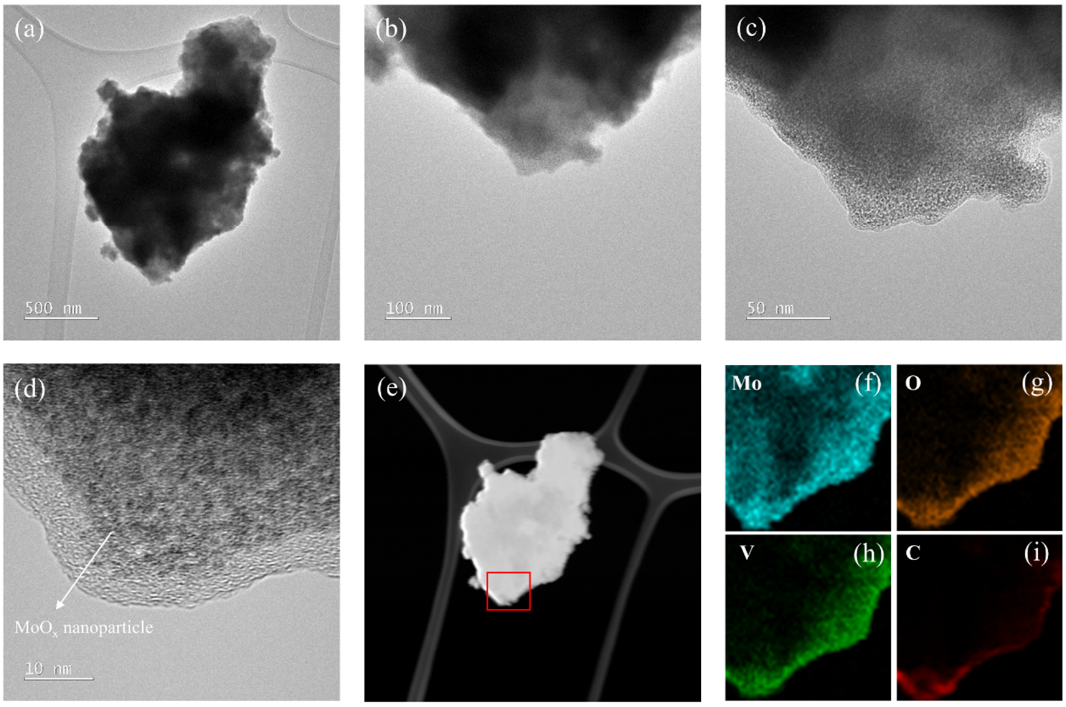

Figure 52. TEM images (a-c), HRTEM image (d), and TEM-EDS elemental mapping (e-i) of $MoO_2/C/V_2C$-2. TEM, HRTEM images, and elemental mapping were measured by Tomasz Kędzierski.

Similarly, a hierarchical structure of MoO_2 nanoparticles constrained in the V_2C/C main framework could be observed in TEM and HRTEM images of $MoO_2/C/V_2C$-2 (Figures 52a-d). In addition, the MoO_2 nanoparticles exhibit smaller sizes by several nanometers than in $MoO_2/C/V_2C$-1, as well as poor cystallinity, in accordance with the XRD results. The uniform distribution of Mo, O, V, and C is verified by the TEM-eds mappings of $MoO_2/C/V_2C$-2 in Figures 52e-i.

3.4.4. Electrochemical characterization

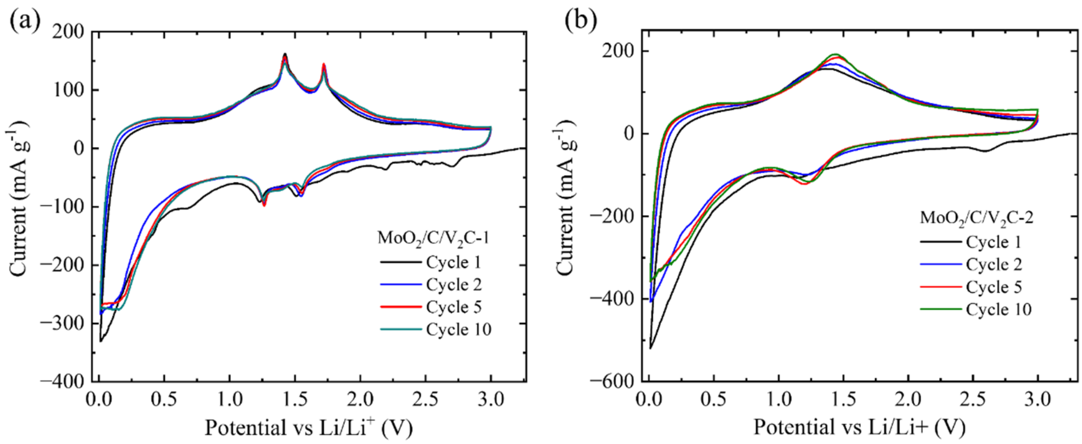

Figure 53. CV curves of the $MoO_2/C/V_2C$-1 and $MoO_2/C/V_2C$-2 electrodes. The CV curve of $MoO_2/C/V_2C$-1 was measured by Hinz Brian [151].

To study the lithium storage behaviors of pristine V_2C, $MoO_2/C/V_2C$-1, and $MoO_2/C/V_2C$-2, CV and GCPL measurements were conducted. Figure 53 shows CV curves of the $MoO_2/C/V_2C$-1 and $MoO_2/C/V_2C$-2 electrodes obtained at a scan rate of 0.1 mV/s in the voltage range 0.01-3 V. As seen in Figure 53a, in the first cathodic sweep, several reduction peaks at the potential over 2 V are visible, which disappear in the following cycles. These peaks indicate irreversible reactions, which might be caused by MoO_3 from the partial oxidation in air at the surface of samples [89]. Two distinct reduction peaks at 1.6 V and 1.3 V correspond to the two-step lithium insertion to MoO_2 forming Li_xMoO_2 (Equation 11), the phase transition of MoO_2 from the monoclinic phase to the orthorhombic phase and back to monoclinic phase [91]. The reduction peak at 0.7 V can be ascribed to the formation of SEI, which is absent in the subsequent cycles. Another reduction peak at around 0.4 V represents the conversion reaction from Li_xMoO_2 to metallic molybdenum (Equation 12) [91]. For the first anodic scan, two oxidation peaks at 1.4 V and 1.7 V are observed. They are attributed to the delithiation process [157-160]. In the second cathodic sweep, the two reduction peaks at 1.6 and 1.3 V are maintained. The reduction peak located at 0.3 is related to the conversion reaction and shows a potential shift, compared with that in the first cycle. This is attributed to the structure change during the conversion reaction. Moreover, the increase in current density indicates a more complete conversion reaction due to the activation process [91]. The peaks in the fifth and tenth cycles are nearly overlapping, implying good reversibility for the insertion and extraction of lithium ions.

The electrochemical reactions can be summarized as follows [158, 161]:

$$xLi^+ + xe^- + MoO_2 \leftrightarrow Li_xMoO_2 \ (0 < x < 0.98) \quad (11)$$

$$MoO_2 + (4-x)Li^+ + (4-x)e^- \leftrightarrow 2Li_2O + Mo \quad (12)$$

By comparison, the CV curve of the $MoO_2/C/V_2C$-2 electrode (Figure 53b) presents distinct CV shapes. The irreversible reduction peak at 2.7 V in the first cathodic sweep is related to electrochemical reactions from MoO_3, similar to that in $MoO_2/C/V_2C$-1 electrode, agreeing with the conclusion of the existence of Mo^{6+} in the composite. The peak at around 1.26 V corresponds to the lithiation of MoO_2 to Li_xMoO_2, which has no phase transition due to the amorphous structure of the MoO_2 nanoparticles [89, 157]. The broad reduction peak at 0.6 V indicates the formation of SEI and the conversion reaction of Li_xMoO_2. Only one oxidation peak at 1.52 V can be observed during the first anodic scan. This is attributed to the delithiation process. Besides, the CV profiles remain fairly consistent and steady in the fifth cycle, suggesting good reversibility and stability of lithium ion transport.

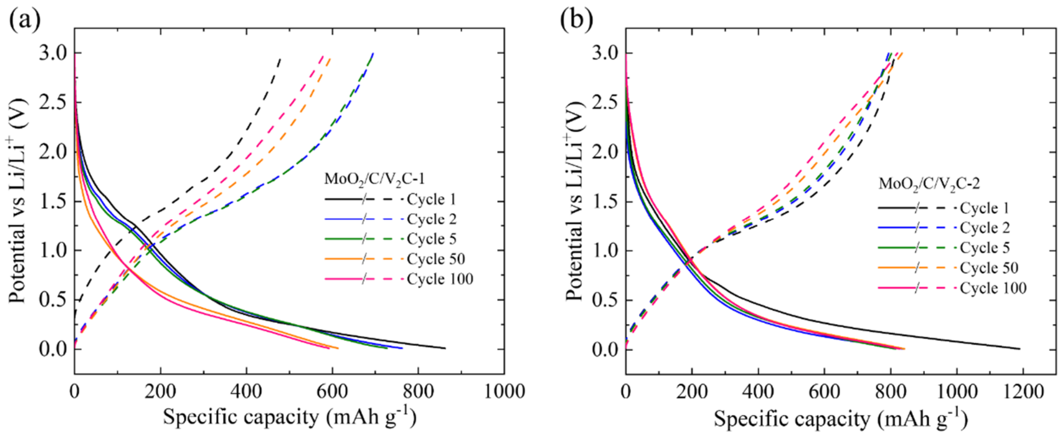

Figure 54. Galvanostatic charge/discharge curves of the $MoO_2/C/V_2C$-1 (a) and $MoO_2/C/V_2C$-2 electrodes at a current density of 100 mA g^{-1} for specific cycles. The galvanostatic charge/discharge curve of the $MoO_2/C/V_2C$-1 was measured by Hinz Brian [151].

The galvanostatic charge/discharge curves of $MoO_2/C/V_2C$-1 and $MoO_2/C/V_2C$-2 electrodes at a current density of 100 mA g^{-1} are presented in Figure 54. The $MoO_2/C/V_2C$-1 electrode delivers an initial discharge/charge capacity of 875/496 mAh g^{-1} with an initial a Coulombic efficiency of 58% (Figure 54a). The capacity loss indicates the formation of SEI and irreversible reaction at high potential (>2.5 V). There are two faint plateaus at around 1.3 and 1.6 V, agreeing with the result of the CV curve. By contrast, a higher Coulombic efficiency of around 70% is achieved for the $MoO_2/C/V_2C$-2 electrode (Figure 54b), which exhibits an initial discharge/charge capacity of 1190/840 mAh g^{-1}, indicating a better synergistic effect of components in this composite.

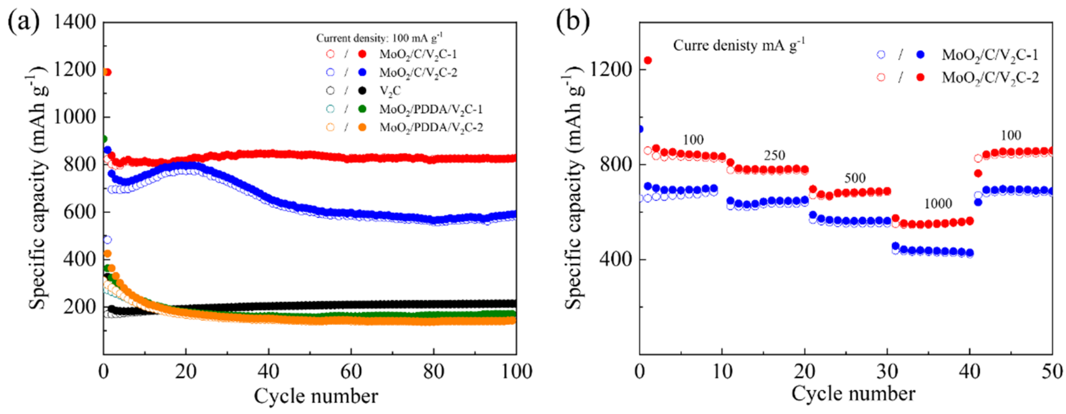

Figure 55. (a) Cycling performance at 100 mA g^{-1} and (b) rate performance of the $MoO_2/C/V2C$-1 and $MoO_2/C/V_2C$-2 electrodes at the current densities ranging from 100 to 1000 mA g^{-1}. In (a), the values for the pristine V_2C, $MoO_2/C/V_2C$-1, and $MoO_2/C/V_2C$-2 are also shown for comparison. The cycling performance of the $MoO_2/C/V_2C$-1 was measured by Hinz Brian [151]. Hollow and solid circles stand for charge and discharge capacities, respectively.

Figure 55a shows the cycling performance of $MoO_2/C/V_2C$-1 and $MoO_2/C/V_2C$-2 electrodes at a current density of 100 mA g^{-1} for 100 cycles. The values for the pristine V_2C, $MoO_2/PDDA/V_2C$-1, and $MoO_2/PDDA/V_2C$-2 are also presented for comparison. The pristine V_2C electrode exhibits good capacity stability but only a low reversible capacity of 196 mAh g^{-1} after 100 cycles, limited by the lithium ion insertion mechanism and the existence of surface groups, which was already discussed in chapter 3.2.4. By comparison, the $MoO_2/PDDA/V_2C$-1 and $MoO_2/PDDA/V_2C$-2 electrodes show higher initial discharge/charge capacity but a fast drop to 170-180 mAh g^{-1} in the first 15 cycles. This might be explained by the poor electrochemical behavior of PDDA in these two composites, which shield the lithium storage performance of MoO_2 [162]. This problem could be overcome via an annealing process, converting PDDA to amorphous carbon, evidenced by the cycling performance of $MoO_2/C/V_2C$-1 and $MoO_2/C/V_2C$-2 electrodes. Both electrodes exhibit enhanced lithium ion storage performance compared to their untreated counterparts. As shown in Figure 55a, the $MoO_2/C/V_2C$-1 electrode shows a slight capacity increase in the first 20 cycles and significant capacity fading in the following 20 cycles. Afterward, the capacity is maintained in the last 60 cycles. The capacity increase can be attributed to the progressive conversion reaction known as the electrode activation effect, where the produced metallic Mo activates more Li_xMoO_2 to participate in the conversion reaction [158, 159]. However, the aggregation of metallic Mo to form metal clusters would hinder this activation effect, causing a capacity drop [157]. The good electrical contacts provided by constructing hierarchical structures with materials like graphene [157], and MXene can alleviate the aggregation and stabilize the cycling process.

In the case of the $MoO_2/C/V_2C$-2 electrode, the amorphous structure of MoO_2 and the higher amount of MXene in the composites offer more complete conversion reactions and better confinement effect, compared with that of the $MoO_2/C/V_2C$-1 electrode, leading to excellent capacity retention of 99% (a reversible capacity of 810 mAh g^{-1}) after 100 cycles.

The rate capabilities of the $MoO_2/C/V_2C$-1 and $MoO_2/C/V_2C$-2 electrodes were also tested under different current densities ranging from 100 to 250, 500, and 1000 mA g^{-1}, see Figure 55b. The $MoO_2/C/V_2C$-1 electrode delivers average specific discharge/charge capacities of 680, 605, 540, and 410 mAh g^{-1}, respectively. As the current density is returned to 100 mAg^{-1}, the specific discharge/charge capacity quickly recovers to 670 mAh g^{-1}. Similar but superior rate performance is observed for the $MoO_2/C/V_2C$-2 electrode, which shows higher average specific discharge/charge capacities of 820, 780, 700, and 603 mAh g^{-1}, respectively, at the same current densities. Consequently, both electrodes display high reversibility and outstanding rate capability, benefiting from the enhanced conductivity in $MoO_2/C/V_2C$ composites.

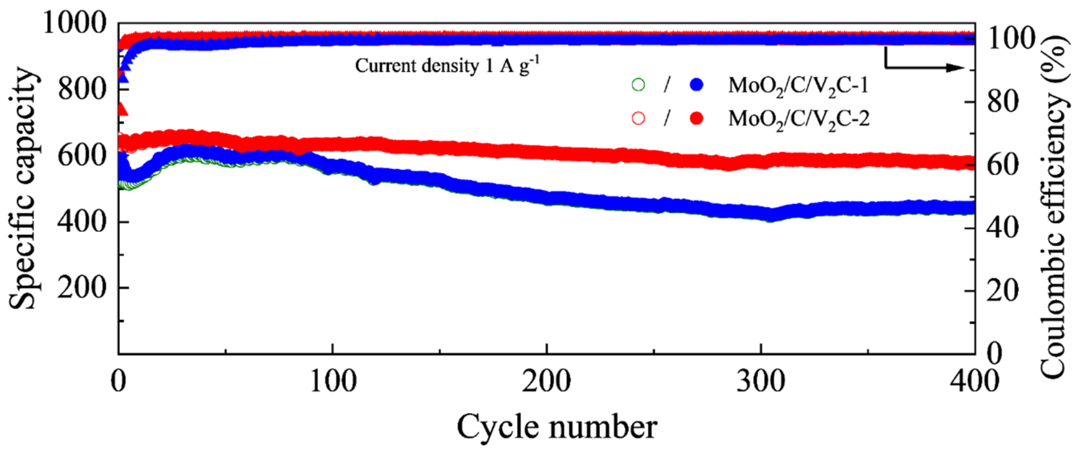

Figure 56. Long cycling capability of the $MoO_2/C/V_2C$-1 and $MoO_2/C/V_2C$-2 electrodes at a high current density of 1000 mA g^{-1}. Hollow and solid circles stand for charge and discharge capacities, respectively.

Inspired by the superior cycling stability and rate capability of the $MoO_2/C/V_2C$-1 and $MoO_2/C/V_2C$-2 electrodes, the long cycling capability of the above two electrodes at a high current density of 1000 mA g^{-1} was investigated. As shown in Figure 56, the $MoO_2/C/V_2C$-1 electrode could still exhibit a reversible capacity of 410 mAh g^{-1} after 400 cycles. Besides, in the case of $MoO_2/C/V_2C$-2, capacity retention of 96% (605 mAh g^{-1}) is achieved after 400 cycles.

In summary, we observe outstanding lithium storage performance of the $MoO_2/C/V_2C$-1 and $MoO_2/C/V_2C$-2 electrodes. This can be ascribed to two aspects: 1. The unique hierarchical structure can help confine MoO_2 nanoparticles to accommodate the volume expansion during cycling and alleviate the metallic Mo aggregation. 2. The V_2C/C framework enhances the electric conductivity of the composites.

3.4.5. Conclusion

$MoO_2/C/V_2C/$ composites were prepared by an electrostatic interaction-assisted hydrothermal and a post-annealing process. Particularly, the stability of V_2C dispersion in water is significantly improved by the introduction of PDDA, providing the possibility to prepare composites of V_2C with MoO_2. As a result, MoO_2 nanoparticles are confined in the framework of V_2C/C, derived from V_2C/PDDA. Benefiting from this unique hierarchical structure, the $MoO_2/C/V_2C$ composites exhibit outstanding lithium storage performance. The $MoO_2/V_2C/C$ composites with the mass ratio of 8:1 and 4:1 (molybdenum source: vanadium source) show a reversible specific capacity of 602 and 810 mAh g^{-1}, respectively at 100 mA g^{-1} after 100 cycles. In particular, the latter composite also exhibits superior long-term cycling performance (capacity retention of 96%) at a high current density of 1000 mA g^{-1} with a reversible capacity of 605 mAh g^{-1} after 400 cycles. Moreover, excellent rate performance is obtained for the electrodes of these two composites. The outstanding lithium storage performance of $MoO_2/C/V_2C$ composites can be ascribed to the unique hierarchical structure which not only buffers the volume expansion of MoO_2, but also improves the electric conductivity.

4. Carbon coated tungsten based anode materials for lithium storage applications[1]

4.1. Introduction

As another kind of transition metal-related advanced anode material, tungsten-based materials are potential alternative anode materials for next-generation LIBs, due to their high theoretical capacity (693 mAh g^{-1} for WO_3 and 432 mAh g^{-1} for WS_2), high intrinsic density, low cost, and environmental friendliness [164-167].

To make tungsten-based materials more accessible for the practical application of LIBs, two important issues need to be solved. The first one is the fast capacity fading and poor rate performance of tungsten-based materials, caused by low electrical conductivity and large volume expansion during cycling [168-171]. This problem has been significantly improved by several routes. Particularly, constructing composites with carbonaceous materials has proven to be a promising strategy [172-174]. Most previous studies reported composites of metal oxides and sulfides with carbonaceous materials, including graphene, carbon nanotubes (CNTs), and carbon fiber, which worked as a substrate via in-situ growth or the liquid assembly method [175-177]. In particular, Liu et al. prepared a WS_2 and graphene oxide composite via electrostatic assisted filtration process. The composite showed a good reversible capacity of 697.7 mAh g^{-1} under 150 mA g^{-1} over 100 cycles [178]. Zhou et al. fabricated WS_2/carbon nanofiber composites by electrospinning [179]. This material exhibited a specific capacity of 458 mAh g^{-1} at 1 A g^{-1} after 100 cycles. Pang and their coworkers grew WS_2 nanosheets on mesoporous carbon CMK-3 by the hydrothermal approach; the resulting composite delivered a good specific capacity of 720 mAh g^{-1} at 100 mA g^{-1} after 100 cycles [180].

Although the above composites exhibited better battery performance than the bare ones, complicated synthesis methods and high-cost carbonaceous materials limit their practical application, which brings us to the second issue, i.e. scalable and low-cost approaches to fabricating tungsten-based anode materials and their composites. This problem has rarely been addressed so far. In this part, a facile and simple approach was developed to fabricate carbon-coated tungsten oxides and sulfides. Two kinds of carbon sources, viz. polyvinyl pyrrolidone (PVP) and cetyltrimethylammonium bromide (CTAB), were adopted to verify our approach. Important synthesis conditions, such as carbonization temperature, sulfurization temperature, and the amount of the carbon source, were optimized. As a result, carbon-coated tungsten oxide and tungsten disulfide synthesized with two different carbon sources exhibit excellent battery performance. The reported approach provides an easy and versatile route that can be extended to the preparation of other metal oxides and disulfides.

[1] Main parts of this chapter have been published. The text of this chapter has in part been taken verbatim from the paper [163].

4.2 Synthesis of WO_x/C composites and WS_2/C composites

(1) pristine WO_3 and the WO_x/C composite: WO_x/C composites were synthesized by a hydrothermal process and subsequent carbonization. Firstly, 600 mg Na_2WO_4 was dissolved in 25 ml deionized water at room temperature, then 9 M HCl solution was added dropwise to adjust the pH of the mixture to 1.5. 200 mg or 500 mg carbon source (CTAB, PVP) was subsequently added to the solution. The mixture was transferred to a 50 ml stainless steel autoclave lined with PTFE and heated to 180°C for 24h and then cooled to room temperature. The precipitate was collected after centrifugation, washed several times with water and ethanol, and dried in an oven at 80 °C for 24 h. Finally, the powder was sintered under a flow of Argon gas at 400 – 800 °C for two hours to obtain WO_x/C composites, which are denoted as c-WO_x/C and p-WO_x/C respectively (x is a value varying from 2 to 3), according to the carbon source (CTAB or PVP) used for the synthesis. Pristine WO_3 was prepared using the same reaction conditions without addition of a carbon source.

(2) pristine WS_2 and the WS_2/C composite: WO_x/C composites as described above were used as precursors and further sulfurized to WS_2/C. 100 mg WO_x/C composite was ground with 500 mg thiourea and then loaded into an alumina crucible, which was put downstream of a tube furnace; Another alumina boat containing 500 mg thiourea was put in the upstream. The tube furnace was then kept at 600 or 800 °C for 2 h under argon flow. Pristine WS_2 was fabricated using the same reaction conditions by sulfurization of pristine WO_3. Depending on the initial carbon source, either CTAB (c) or PVP (p), the obtained products are denoted as c/p-WS_2/C. Mixed-phase composites are labeled as c/p-WO_x/C-WS_2/C.

4.3 Experimental design

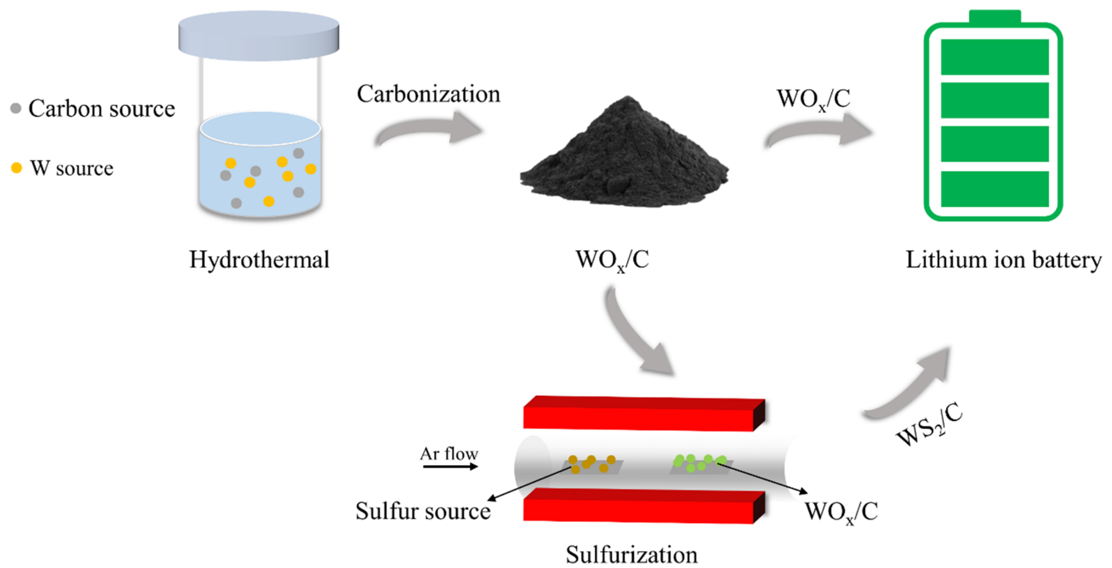

Figure 57. Schematic illustration of the preparation of WO_x/C and WS_2/C composites [163].

The synthesis procedure of WO_x/C and WS_2/C composites is illustrated in Figure 57. The WO_x/C was obtained based on a hydrothermal process and a post-carbonization procedure. After an additional sulfurization step, the corresponding WS_2/C was fabricated. It is noted that instead of high-cost carbonaceous materials like graphene, mesoporous carbon, and carbon nanotubes, the commonly used and inexpensive carbon source CTAB and PVP were introduced. Both carbon-coated tungsten oxides and disulfides could be easily obtained without the involvement of any sacrificial template and complex preparation steps. The effects of crucial synthesis parameters, such as the amount of carbon source, carbonization and sulfurization temperature on the crystal structure, morphology, and battery performance of the above composite materials were investigated.

4.4. CTAB-based WO_x and WS_2 carbon composites for lithium storage

In this chapter, CTAB was used as the carbon source to prepare the c-WO_x/C composites. In addition, c-WO_x/C-WS_2/C and c-WS_2/C composites were synthesized via additional sulfurization at different temperatures. These above composites were investigated physically and electrochemically. Part of the electrochemical characterization was done by Finn Sebastian under the supervision of the author [181].

4.4.1. Physical characterization

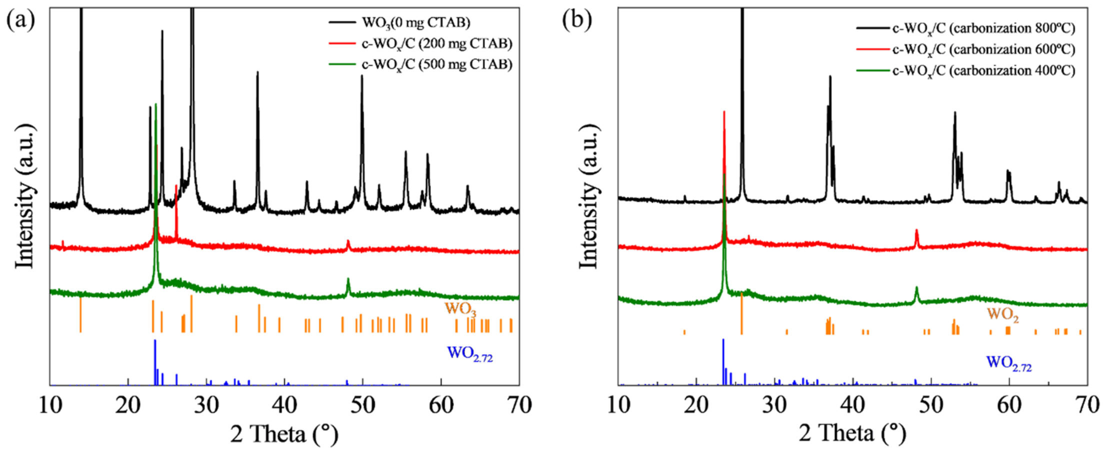

Figure 58. Powder XRD patterns of c-WO_x/C with various carbonization temperatures and amounts of CTAB [163]. (a) 600 °C carbonization and 0 mg CTAB, 600 °C carbonization and 200 mg CTAB, 600 °C carbonization and 500 mg CTAB. Vertical ticks show reference patterns according to ICSD code 32001 [182] (WO_3) and ICSD code 15254 [183] ($WO_{2.72}$), respectively. (b) 400 °C carbonization and 500 mg CTAB, 600 °C carbonization and 500 mg CTAB, 800 °C carbonization and 500 mg CTAB. Vertical ticks show reference patterns according to ICSD code 80829 [153] (WO_2) and ICSD code 15254 [183] ($WO_{2.72}$), respectively.

Figure 58a shows the powder XRD patterns of pristine WO_3 and c-WO_x/C composites produced with various amounts of carbon source (CTAB). The pattern of WO_3 exhibits diffraction peaks that fit well with those of h-WO_3 (ICSD code 32001). While the patterns of c-WO_x/C composites prepared with 200 mg and 500 mg CTAB exhibit distinct peaks at 23° and 48°, characteristic of $WO_{2.72}$ (ICSD code 15254) [184]. In addition, the amounts of CTAB were fixed at 500 mg and the influence of carbonization temperature on the obtained phase is presented in Figure 58b. The carbonization temperatures of 400 °C and 600 °C produced the same phase of $WO_{2.72}$. However, with a higher carbonization temperature (800°C), a new phase of WO_2 was obtained. Thus, we conclude that CTAB also acts as a reducing agent during the carbonization in addition to serving as a carbon source, and this effect becomes stronger at higher temperatures.

The c-WO_x/C composite synthesized with 500 mg CTAB and a carbonization temperature of 600 °C was further sulfurized. The XRD patterns of c-WS_2/C with various sulfurization temperatures are presented in Figure 59a. Upon sulfurization, the characteristic $WO_{2.72}$-diffraction peaks are suppressed and new features at 13°, 32°and 60° appear, pointing to the presence of WS_2 (ICSD code 202366). When the sulfurization process is performed at 800 °C, the resulting product is c-WS_2/C as indicated by the complete absence of the $WO_{2.72}$ diffraction peaks. By comparison, if the sulfurization temperature is 600 °C, a mixture of two components (c-WO_x/c-WS_2/C) is formed. It can thus be concluded that the degree of sulfurization is controlled by the sulfurization temperature [185]. Moreover, all peaks associated with WS_2 are rather broad, indicating poor crystallinity. The phase of WS_2 was maintained when a small amount of CTAB (200 mg) was used (Figure 59b), which is similar to the case of $WO_{2.72}$.

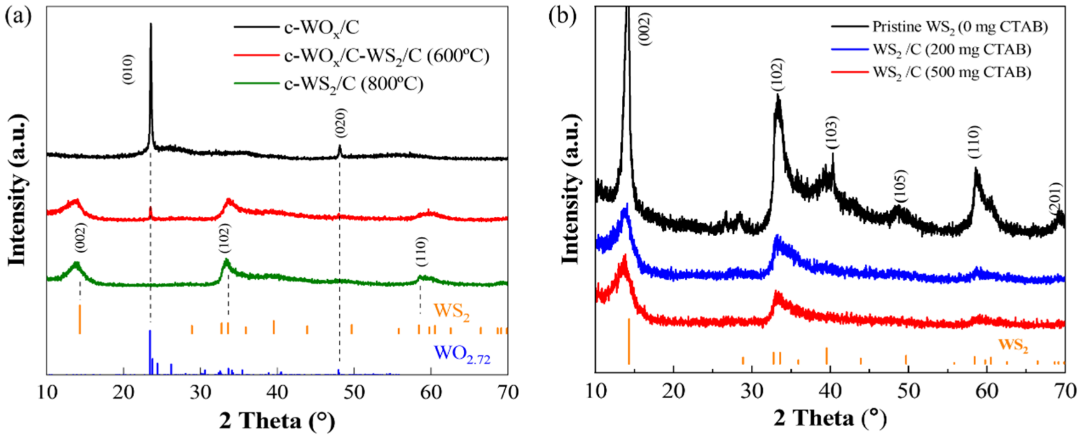

Figure 59. XRD patterns of c-WS_2/C with various sulfurization temperatures and amounts of CTAB [163]. (a) XRD patterns of c-WO_x/C, c-WO_x/C-WS_2/C (sulfurization at 600°C) and c-WS_2/C (sulfurization at 800°C). Vertical ticks show the reference patterns according to ICSD code 202366 [186] (WS_2) and ICSD code 15254 [183] ($WO_{2.72}$), respectively. (b) XRD patterns of c-WS_2/C (sulfurization at 800°C) with 0, 200, and 500 mg CTAB added. Vertical ticks show the reference patterns according to ICSD code 202366 [186].

The effect of carbonization temperature, the amount of CTAB added, and sulfurization temperatures on the microstructure of the resulting composites is demonstrated by SEM and TEM measurements. Figure 60 shows SEM images of c-WO_x/C with various carbonization temperatures and amounts of CTAB. The c-WO_x/C composites prepared with an identical carbonization temperatures (600 °C) but different amounts of CTAB (200 mg, 500 mg) exhibit a nanocluster-like structure of agglomerated nanorods with 100 – 200 nm in length (Figures 60a-c), demonstrating that the change in the amounts of carbon source has no obvious influence on the morphology of c-WO_x/C composites. However, a low carbonization temperature (400 °C) caused the production of irregular c-WO_x/C composites (Figure 60d).

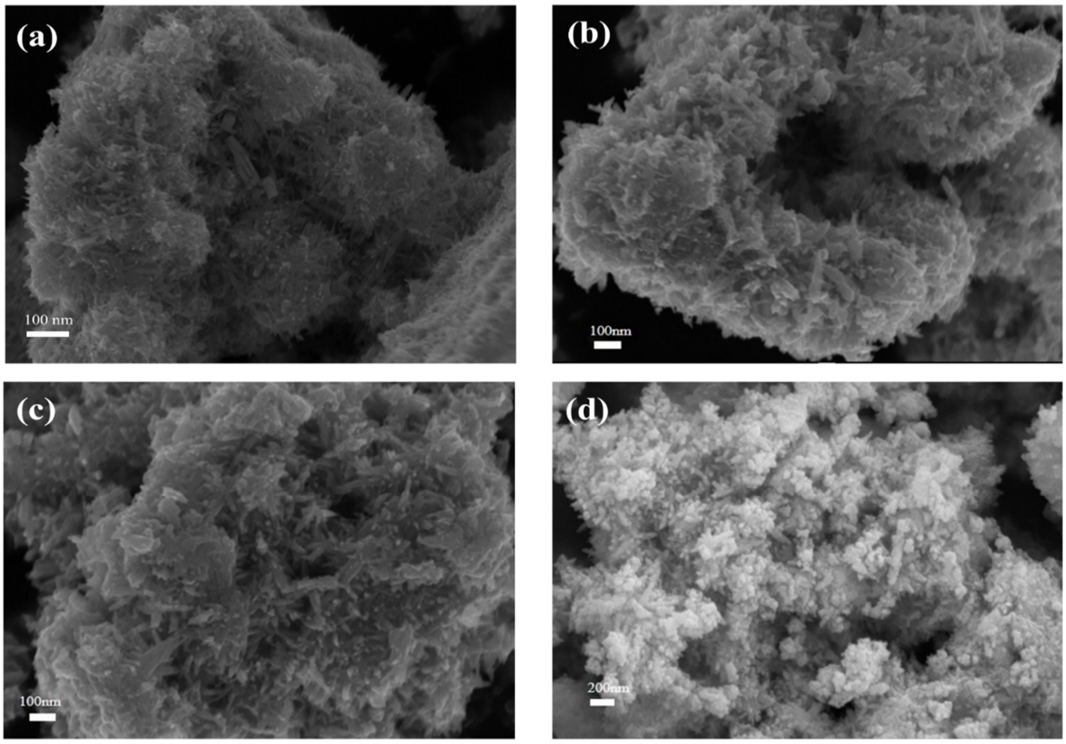

Figure 60. SEM images of c-WO_x/C with various carbonization temperatures and amounts of CTAB [163]. (a) 600 ℃ carbonization and 500 mg CTAB. (b) 600 ℃ carbonization and 200 mg CTAB. (c) 600 ℃ carbonization and 500 mg CTAB. (d) 400 ℃ carbonization and 500 mg CTAB.

The microstructure of c-WO_x/C synthesized with 500 mg CTAB and a carbonization temperature of 600 ℃ was further confirmed by the TEM and HRTEM images shown in Figure 61. The c-WO_x/C nanorods are coated by amorphous carbon, which agrees with the SEM images. In addition, the lattice fringes with a spacing of 0.375 nm can be indexed to the (010) planes, corresponding to the main peak of $WO_{2.72}$ in the XRD patterns.

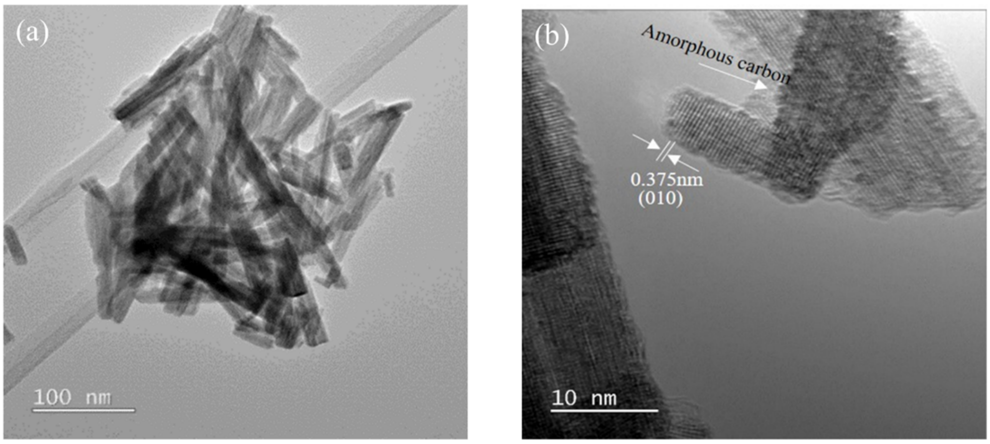

Figure 61. The TEM image (a) and HR-TEM image (b) of c-WO_x/C synthesized with 500 mg CTAB and carbonization temperature of 600 ℃ [163].

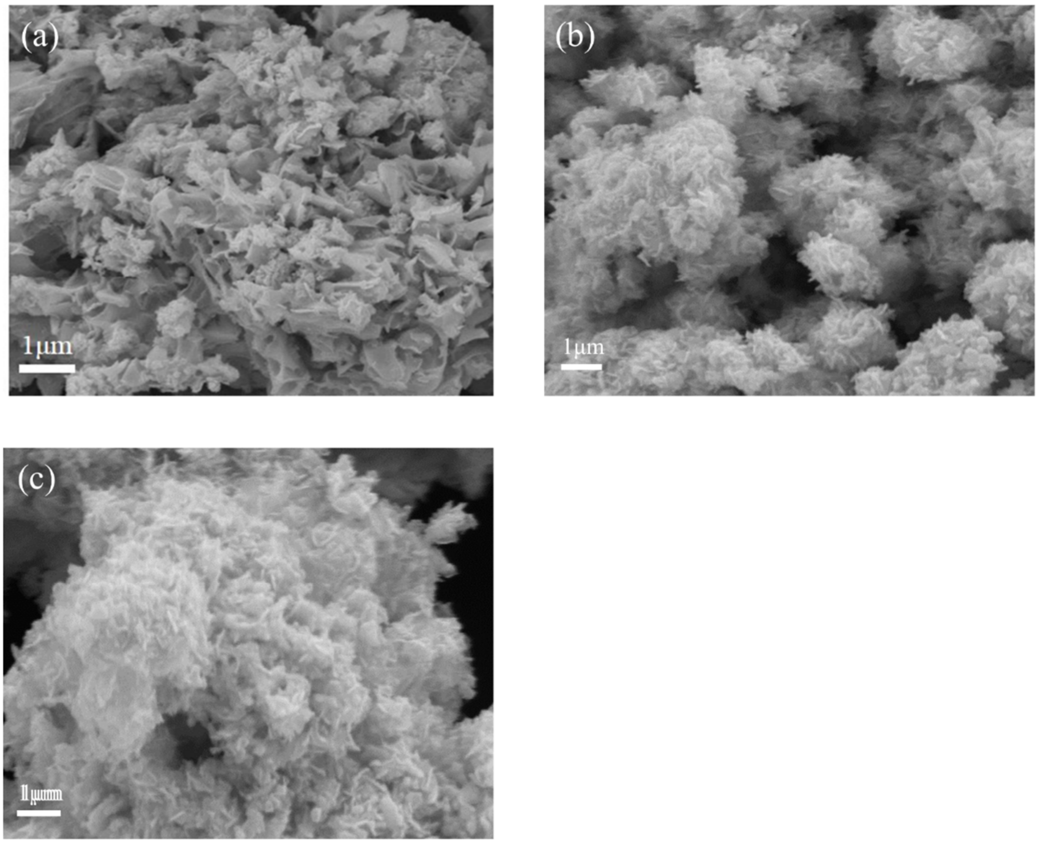

Figure 62. SEM images of c-WO_x/C-WS_2/C (sulfurization at 600 °C) (a) and c-WS_2/C (sulfurization at 800 °C) with 500 mg (b), and 200 mg (c) CTAB [163].

Figure 62 exhibits SEM images of c-WO_x/C-WS_2/C (sulfurization at 600°C) and c-WS_2/C (sulfurization at 800°C) with 200, and 500 mg CTAB. Compared with the WO_x/C composite, the mixed phase c-WO_x/C-WS_2/C is composed of curled nanosheets as well as nanoparticles, which are assumed to be c-WO_x/C and c-WS_2/C, respectively (Figure 62a). After the complete sulfurization at 800 °C, only curled nanosheets are observed in the resulting c-WS_2/C (Figure 62b). Moreover, as shown in Figure 62c, the morphology of c-WS_2/C does not change noticeably at a small amount of CTAB added (200 mg), which is in accordance with the case of c-WO_x/C.

Figure 63 presents HRTEM images and elemental mapping images of the mixed phase c-WO_x/C-WS_2/C. Both WS_2 nanosheets and WO_x nanoparticles are observed in the HRTEM images (Figures 63a, b), which is consistent with the corresponding SEM images. EDS elemental mapping, presented in Figures 63c-f, further illustrates the homogenous distribution of W, O, S, and C within a randomly selected area in Figure 63b, indicating the coexistence of c-WO_x/C and c-WS_2/C, which is in good agreement with the XRD data.

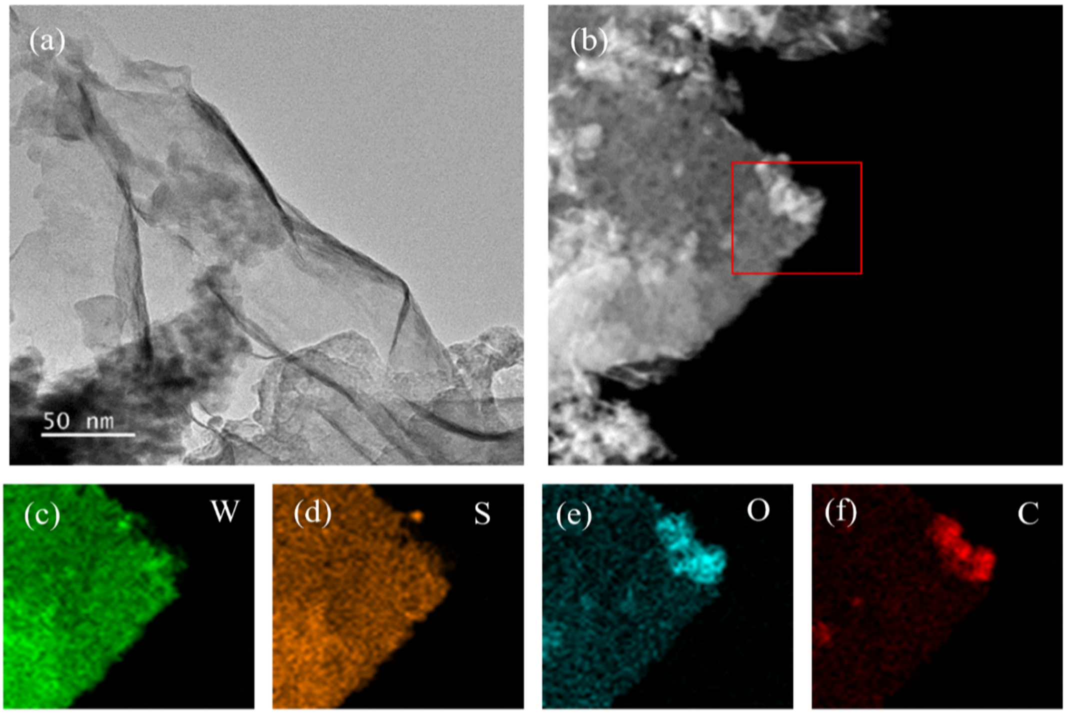

Figure 63. TEM images (a,b) and elemental mapping images (c-f) of c-WO_x/C-WS_2/C (sulfurized at 600 °C) [163].

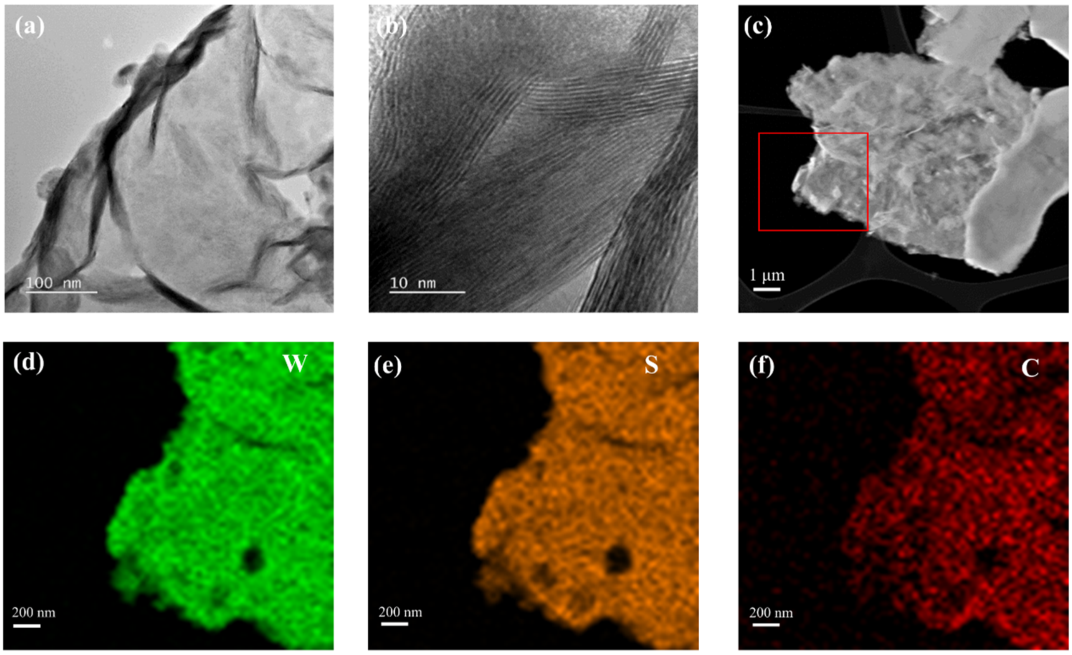

Figure 64. TEM images, HR-TEM images (a-c), and elemental mapping images (d-f) of c-WS_2/C (sulfurized at 800 °C) [163].

The HRTEM images and elemental mapping images of c-WS_2/C (sulfurized at 800 °C) are shown in Figure 64. The c-WS_2/C composite exhibits curled nanosheets with an interlayer spacing of 0.675 nm, which can be attributed to the (002) plane of WS_2 [187] (Figures 64a,b). The elemental mappings of c-WS_2/C by TEM-EDS presented in Figures 64c-f confirm the uniform distribution of W, S, and C in this composite.

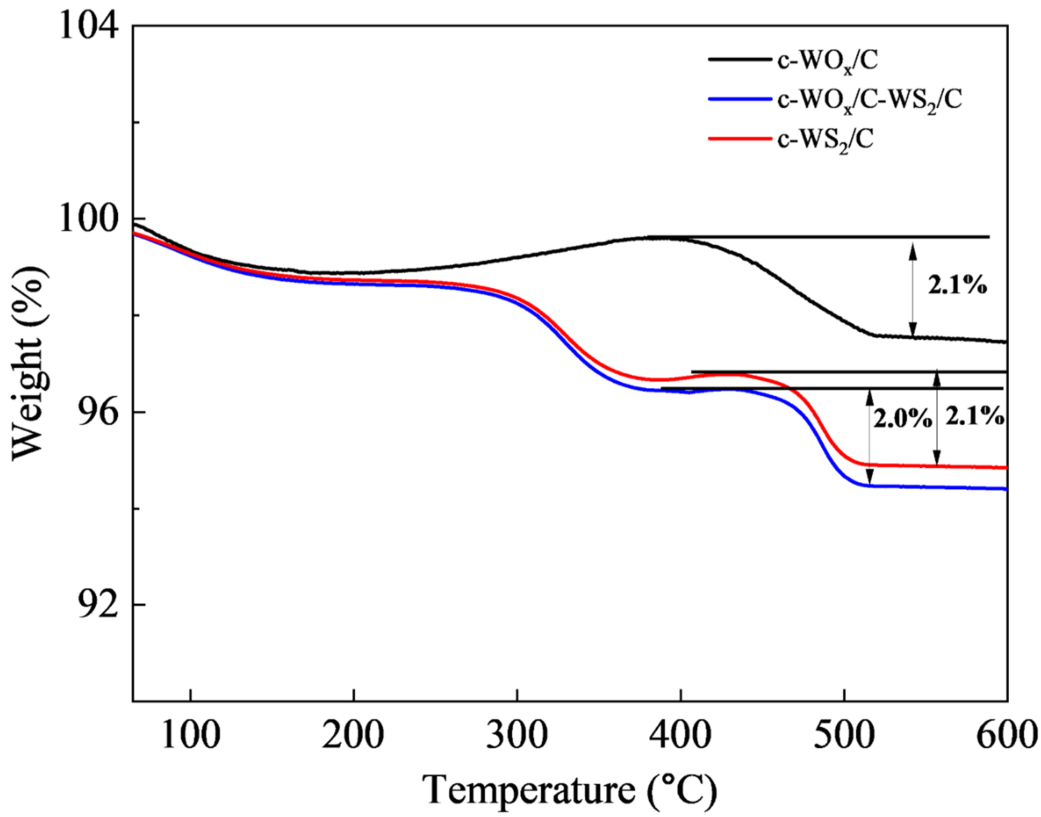

Figure 65. TGA curves of c-WO_x/C, c-WO_x/C-WS_2/C, and c-WS_2/C [163].

The thermogravimetric analysis (TGA) was conducted to study the carbon content in the c-WO_x/C, c-WO_x/C-WS_2/C, and c-WS_2/C composites in air. Figure 65 shows the TGA curves of c-WO_x/C, c-WO_x/C-WS_2/C, and c-WS_2/C. The weight loss from 100 °C to 200 °C in three samples can be attributed to the vaporization of adsorbed water. For the c-WO_x/C sample, a slight weight increase is observed from 300 °C to 400 °C corresponding to the oxidation of $WO_{2.72}$ in c-WO_x/C, verifying the existence of oxygen vacancies. In contrast, significant weight loss can be found for c-WO_x/C-WS_2/C and c-WS_2/C samples in this temperature range, which is related to the oxidation of WS_2. In addition, the weight increase derived from the oxidation of $WO_{2.72}$ in c-WO_x/C-WS_2/C is not visible due to a smaller weight change compared to the oxidation of WS_2. When the applied temperature is above 400 °C, a distinct weight loss ascribed to combustion reactions of the carbon component can be observed for the three samples. Consequently, the carbon content in c-WO_x/C, c-WO_x/C-WS_2/C, and c-WS_2/C are about 2.0, 2.1, and 2.0 (±0.5) wt%, respectively.

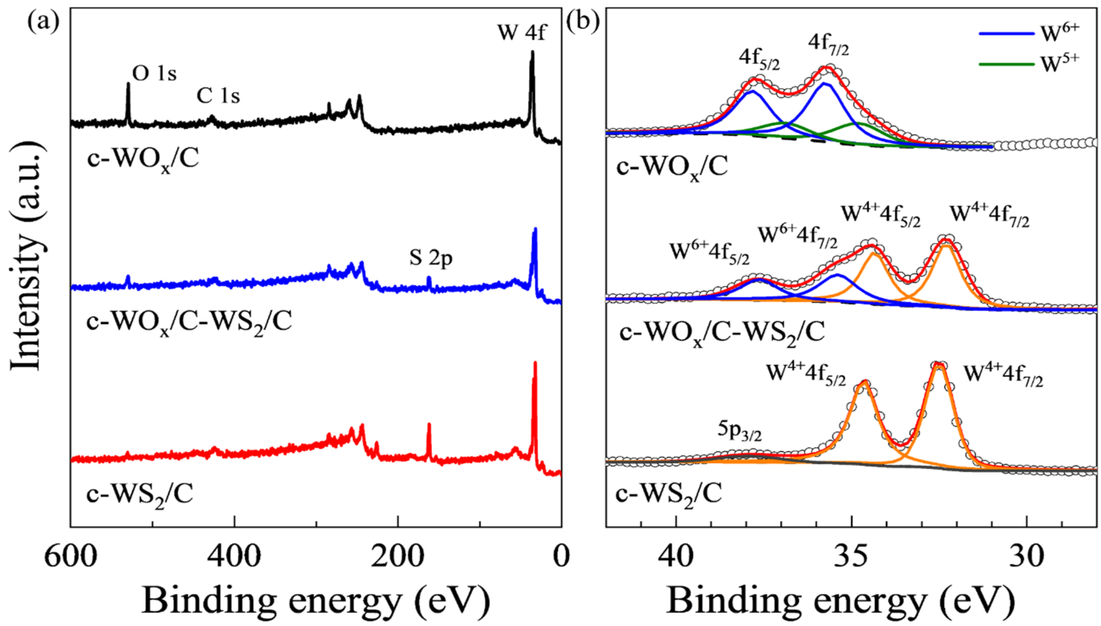

Figure 66. Wide-scan XP spectra (a) and W 4f XP spectra (b) of c-WO_x/C, c-WO_x/C-WS_2/C, and c-WS_2/C [163].

Chemical states and compositions of c-WO_x, c-WO_x/C-WS_2/C, and c-WS_2/C were monitored by XPS. The wide-scan XP spectrum of WO_x/C shown in Figure 66a confirms the presence of W, O, and C in this material. After the sulfurization, there is a clear signature of S, as seen in the wide-scan spectra of c-WO_x/C-WS_2/C and c-WS_2/C. Simultaneously, the signal of O gradually decreases in intensity due to the sulfurization treatment. These observations agree well with the results of the EDS elemental mapping.

The W 4f XP spectrum of the c-WO_x/C composite shown in Figure 66b exhibits a superposition of two W $4f_{7/2,5/2}$ doublets. The first doublet, with the component peaks at ~35.7 and ~37.8 eV, is attributed to W^{6+}. The second, comparably weak doublet, with the component peaks at ~34.9 eV and ~36.9 eV, is assigned to W^{5+}. One can thus conclude that c-WO_x/C is composed of W^{5+} and W^{6+}, in good agreement with literature data [188, 189]. In contrast, in the W 4f XP spectrum of c-WS_2/C, a single W $4f_{7/2,5/2}$ doublet, with the component peaks at 32.5 eV and 34.6 eV, is found, corresponding to the W^{4+} oxidation state [190]. This doublet is accompanied by a broad W $5p_{3/2}$ peak at 37.8 eV. Complementary information is provided by the S 2p XP spectrum of c-WS_2/C. The characteristic S $2p_{3/2,1/2}$ doublet, with the component peaks at 161.8 eV and 162.9 eV (Figure 67), can be assigned to an S−W bond, confirming the presence of WS_2. Moreover, the very low intensity of the O 1s peak in the spectrum of c-WS_2/C (Figure 67) verifies a nearly complete conversion of WO_x/C to WS_2/C. Significantly, the W 4f XP spectrum of the mixed-phase, c-

$WO_x/C-WS_2/C$, confirms the presence of both W^{4+} and W^{6+}. Specifically, this spectrum exhibits two W $4f_{7/2,\ 5/2}$ doublets, with the component peaks at 32.2 eV and 34.4 eV for the first one and the component peaks at 35.5 eV and 37.7 eV for the second one. A coexistence of WO_x/C and WS_2/C in c-$WO_x/C-WS_2/C$ is thus confirmed.

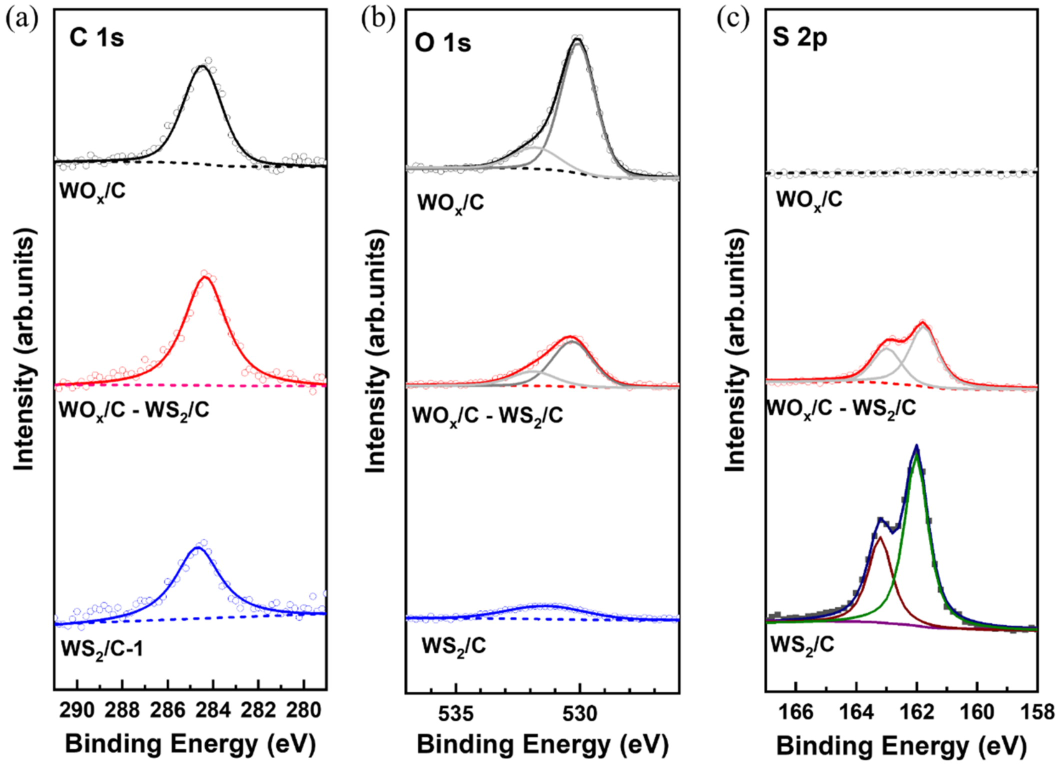

Figure 67. C 1s (a), O 1s, (b) and S 2p (c) XP spectra of c-WO_x/C, c-$WO_x/C-WS_2/C$, and c-WS_2/C [163].

4.4.2. Electrochemical characterization

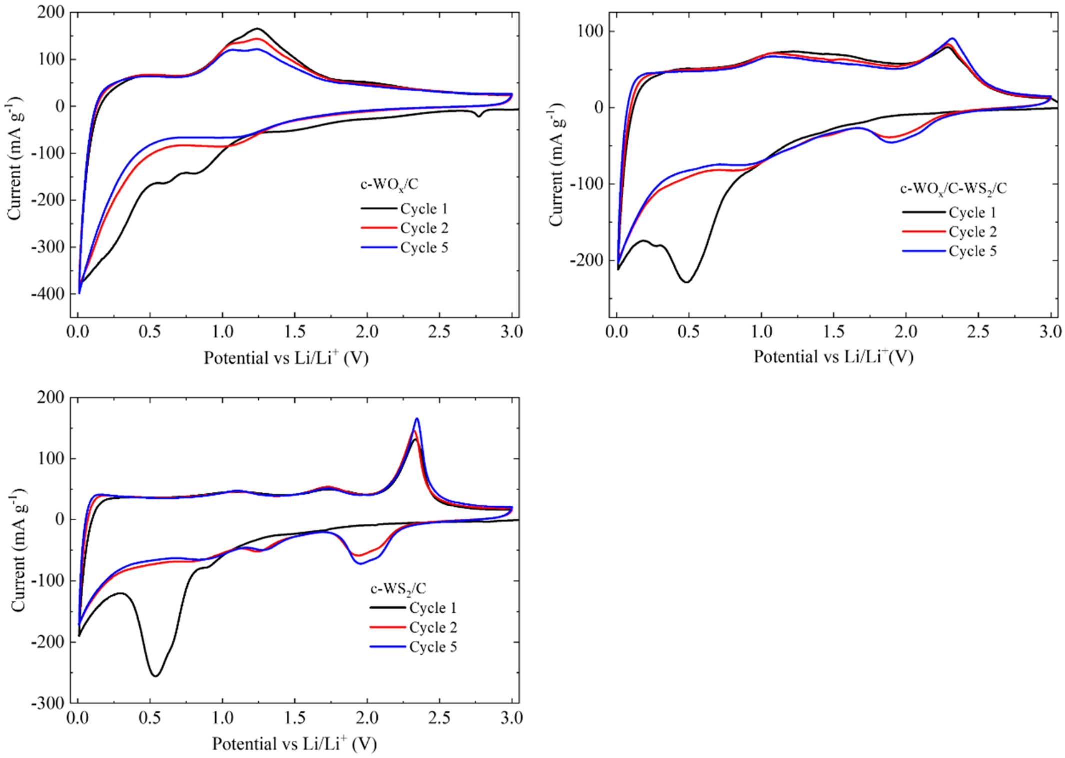

Figure 68. CV curves for (a) c-WO_x/C, (b) c-WO_x/C-WS_2/C, and (c) c-WS_2/C electrodes for the first, second, and fifth cycles at a scan rate of 0.1 mV s^{-1} in a potential range of 0.01–3 V versus Li/Li^+ [163].

To investigate the electrochemical behavior of c-WO_x/C, c-WO_x/C-WS_2/C, and c-WS_2/C electrodes, cyclic voltammetry (CV) at a scan rate of 0.1mV s^{-1} and galvanostatic cycling with potential limitation (GCPL) were performed. The current density was set to either 100 or 500 mA g^{-1} and the potential window was set from 0.01 V to 3 V.

Figure 68a shows the first, second, and fifth CV cycles of the c-WO_x/C electrode. The first cathodic scan displays five reduction peaks. Peaks at 2.8 and 0.6 V correspond to irreversible reactions and the formation of solid electrolyte interface (SEI), which disappear in the subsequent cycles. The other two reduction peaks at 1.5 and 0.8 V can be assigned to the lithium intercalation into $WO_{2.72}$ (Equation 13). The peak located at 0.3 V is attributed to the conversion reaction of $Li_xWO_{2.72}$ (Equation 14). During the first anodic process, an oxidation peak appears at 1.25 V, which is associated with the delithiation process of Li_2O (Equation 15) [191].

In the second discharge cycle, only one reduction peak at 1.1 V, corresponding to the lithium insertion into $WO_{2.72}$ (Equation 13), is visible. This peak is representative for a similar electrochemical reaction as the reduction peaks in the first cathodic scan but its position is slightly different, which can be attributed to structural changes caused by irreversible conversion reactions during the initial cycling[191]. The second and fifth CV cycles are mostly overlapping, implying high reversibility of Li^+ storage in the c-WO_x/C electrode after the second cycle.

The relevant electrochemical reactions for c-WO_x/C can be expressed as below[191]:

$$WO_{2.72} + xLi^+ + xe^- \leftrightarrow Li_x WO_{2.72} \quad (13)$$

$$Li_x WO_{2.72} + (5.44 - x)Li^+ + (5.44 - x)e^- \rightarrow W + 2.72Li_2O \quad (14)$$

$$Li_2O + W \rightarrow xWO_{2.72} + (2 - x)W + zLi_2O + (2 - 2z)Li^+ + (2 - 2z)e^- \quad (15)$$

The c-WS_2/C electrode exhibits a completely different electrochemical behavior as shown by the respective CV curves in Figure 68c. In the first cathodic scan, three reduction peaks are observed. The ones at 1.6 and 0.9 V can be attributed to the lithiation of WS_2 to form Li_xWS_2 (Equation 16). The third reduction peak, centered at 0.6 V, corresponds to the conversion reaction from Li_xWS_2 to metallic W (Equation 17) as well as to the generation of SEI [192, 193]. Also, in the first anodic scan, three oxidation peaks are recorded. Two of them, at 1.1 and 1.7 V, are fingerprints of the delithiation of Li_xWS_2 to form WS_2 (Equation 16). The pronounced oxidation peak at 2.3 V is associated with the oxidation of Li_2S to S (Equation 18) [193]. In the subsequent cathodic scan, three new reduction peaks appear which are ascribed to the lithiation of WS_2 (features at 0.9 and 1.3 V) (Equation 16) and the formation of Li_2S (1.9 V). At the same time, the reduction peak at 0.6 V disappears, indicating the irreversibility of the conversion reaction.

The electrochemical processes for c-WS_2/C can be described as follows:

$$WS_2 + xLi^+ + xe^- \leftrightarrow Li_x WS_2 \quad (16)$$

$$Li_x WS_2 + (4 - x)Li^+ + (4 - x)e^- \rightarrow 2Li_2 S + W \quad (17)$$

$$2Li_2 S \leftrightarrow 4Li^+ + 4e^- + 2S \quad (18)$$

The oxidation peaks in the second anodic scan are overlapping with the ones in the first cycle. Besides, the CV profiles remain fairly consistent and steady in the fifth cycle, suggesting good reversibility and stability of lithium ion transport.

For the mixed-phase, c-WO_x/C-WS_2/C, the CV profile in Figure. 68b displays the fingerprints of both constituting materials. Specifically, three reduction peaks in the first cathodic scan at 1.0, 0.5, and 0.3 V emphasize the intercalation of lithium ions into $WO_{2.72}$ and WS_2, the formation of an SEI, and the conversion reactions of WS_2 and $WO_{2.72}$, respectively. Oxidation peaks in the first anodic scan correspond to the delithiation of Li_xWO_x and Li_xWS_2 (1.1 V) and the delithiation of WS_2 (2.3 V). Similarly, in the further cycles, features related to WO_x/C as well as to WS_2/C are observed thereby showing that both materials in this mixed-phase contribute to the electrochemical behavior. Again, the good matching of the redox peaks in the second and fifth cycles indicates high reversibility of Li^+ storage in the c-WO_x/C-WS_2/C electrode.

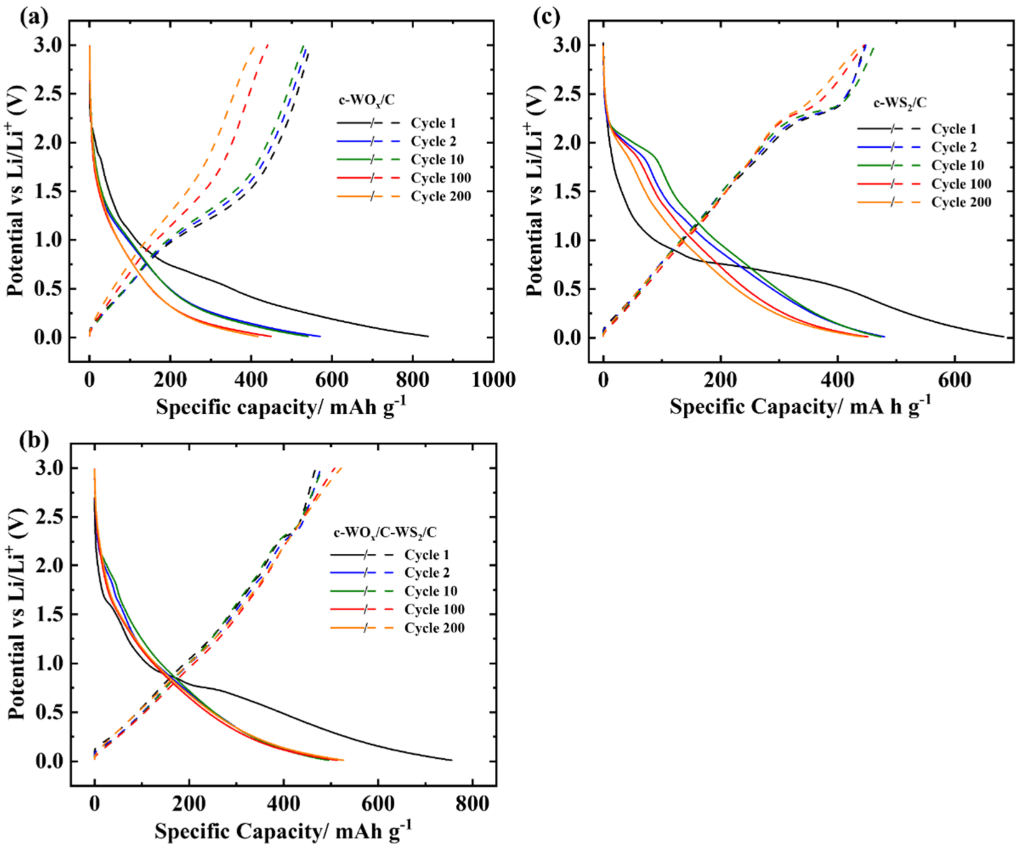

Figure 69. Galvanostatic discharge/charge curves of the c-WO_x (a), c-WO_x-WS_2/C, (b) and c-WS_2/C (c) electrodes at a current density of 100 mA g^{-1} for specific cycles [163].

Figure 69 shows the galvanostatic charge-discharge profiles for the 1st, 2nd, 10th, 100th, and 200th cycles of the c-WO_x/C, c-WO_x/C-WS_2/C, and c-WS_2/C electrodes at a current density of 100 mA g^{-1}. The observed potential plateaus are in good agreement with the CV results. The corresponding cycling performances are shown in Figure 70, where the data of the pristine WO_3 electrode are also presented for comparison. The pristine electrode shows an initial specific discharge/charge capacity of 645/338 mAh g^{-1} which decreases gradually to 198/197 mAh g^{-1} after 200 cycles. The reason behind this decrease is typically assigned to the volume expansion effects and poor electric conductivity [184]. In contrast, the carbon-coated c-WO_x/C electrode not only delivers a higher initial specific discharge/charge capacity of 840/560 mAh g^{-1} but also exhibits noticeably better capacity retention (74%), which still amounts to 420 mAh g^{-1} after 200 cycles.

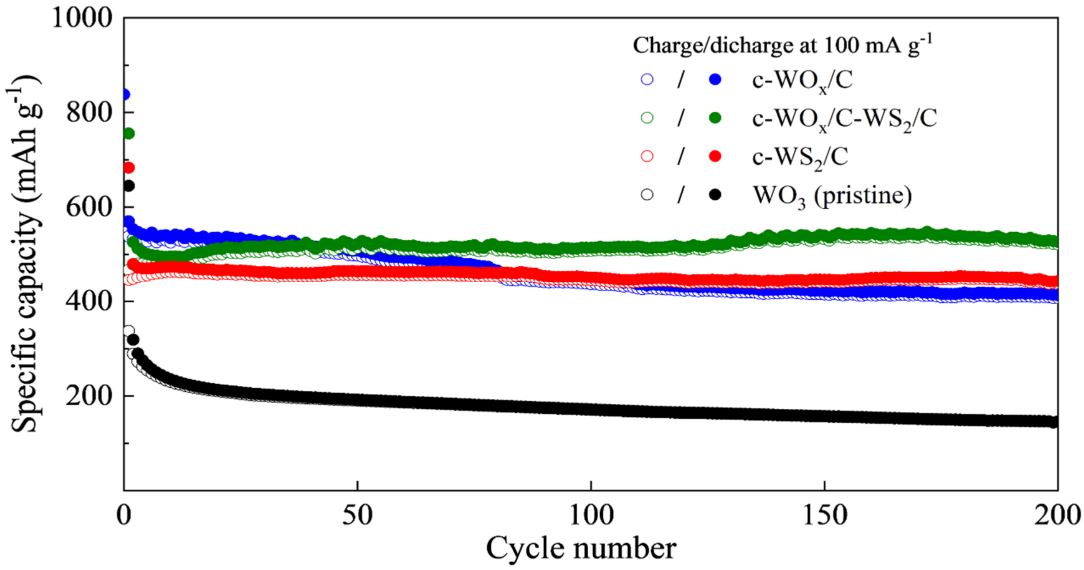

Figure 70. Cycling performance for the c-WO_x/C, c-WO_x/C-WS_2/C, and c-WS_2/C electrodes at a current density of 100 mA g^{-1}. The values for the pristine WO_3 electrode are also shown for comparison [163]. Hollow and solid circles stand for charge and discharge capacities, respectively.

For comparison, if a relatively small amount of CTAB (200 mg) is used, the initial specific discharge/charge capacity (860/630 mAh g^{-1}) is slightly higher than for the "standard" amount of CTAB (500 mg) but the capacity retention value (48%) is noticeably lower (Figure 71a). This can be explained by the lower carbon content resulting from the smaller amount of CTAB, which is not enough to completely cover WO_x. By contrast, the sufficiently high carbon content (500 mg) provides the full carbon coating on the WO_x surface, which not only promotes the electron and lithium ion diffusion kinetics but also alleviates the pulverization and volume expansion of WO_x[194].

The c-WO_x/C electrode exhibits a faster capacity fading in the first 20 cycles and the specific capacity is gradually maintained in the following cycles if the carbonization temperature is set to 400°C (Figure 71b). Interestingly, a capacity retention of 88% is observed after nearly 100 cycles for the c-WO_x/C electrode synthesized at the high carbonization temperature (800°C), but the low initial specific discharge/charge capacity of 630/420 mAh g^{-1} hinders its application. The above results imply that parameters of the preparation procedure, such as carbonization temperature and the amount of carbon source, play crucial roles in the battery performance of the synthesized c-WO_x/C.

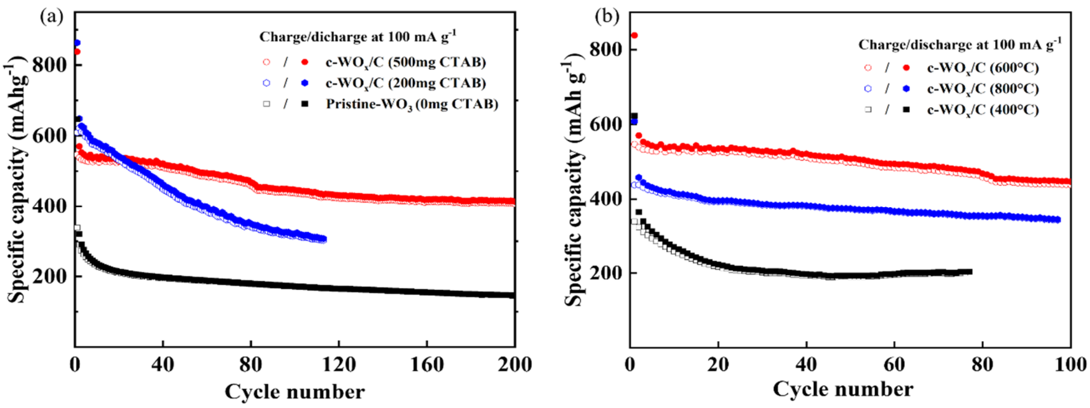

Figure 71. Cycling performance of c-WO_x/C with 0, 200, and 500 mg CTAB and a fixed carbonization temperature of 600°C (a), and c-WO_x/C with carbonization temperatures of 400, 600 and 800℃ and a fixed amount of CTAB 500 mg (b) [163]. Hollow and solid circles stand for charge and discharge capacities, respectively.

After sulfurization at 600°C, c-WO_x/C was partially converted to c-WS_2/C, and the mixed-phase, c-WO_x/C-WS_2/C, was obtained. In comparison with the c-WO_x/C electrode, the c-WO_x/C-WS_2/C electrode shows enhanced cycling stability as well as slightly lower initial specific discharge/charge capacities of 760/530 mAh g^{-1}. Remarkably, after 200 cycles, the specific discharge capacity of this electrode is maintained at 525 mAh g^{-1} (99% capacity retention) and no obvious capacity fading is observed during the cycling (Figure 70).

The full sulfurization of c-WO_x/C to c-WS_2/C at 800°C provides an electrode with an initial discharge/charge capacity of 680/483 mAh g^{-1}. Besides, this electrode shows remarkable cycling stability (95% capacity retention) and a high discharge capacity of 460 mAh g^{-1} after 200 cycles, which is close to the theoretical capacity of WS_2 (462 mAh g^{-1}) (Figure 70).

The pristine WS_2 and c-WS_2/C electrodes prepared with a small amount of CTAB (200 mg) were also tested to verify the importance of carbon coating. The respective pristine WS_2 electrode displays a fast discharge capacity fading from 836 to 248 mAh g^{-1} after 60 cycles (Figure 72). The c-WS_2/C electrode has a high initial capacity but shows a significant capacity drop from 763 to 428 mAh g^{-1} after 100 cycles (Figure 72). Hence, optimization of the amounts of CTAB for the c-WS_2/C electrode is of importance.

In brief, the electrodes of c-WO_x/C and c-WS_2/C as well as the mixed-phase c-WO_x/C-WS_2/C all exhibit better cycling performance and higher specific capacities than the pristine WO_3 electrode implying the usefulness of the facile composite preparation method described here.

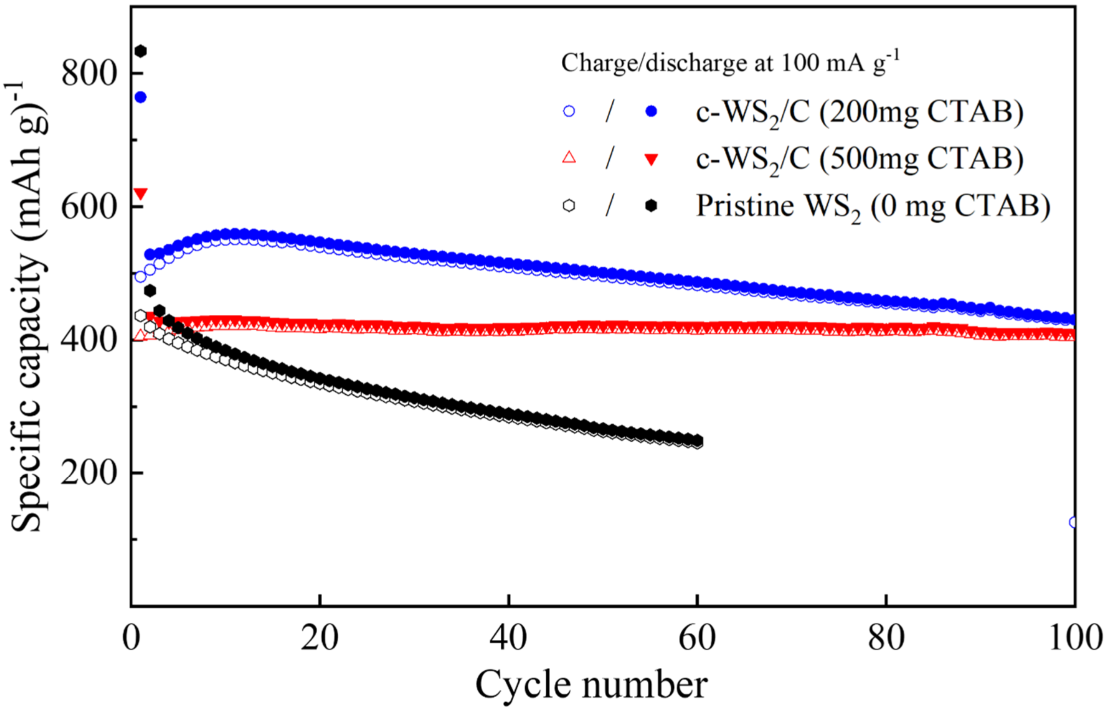

Figure 72. Cycling performance of c-WS_2/C with 0, 200, and 500 mg CTAB [163]. Hollow and solid circles stand for charge and discharge capacities, respectively.

Additionally, as shown in Figure 73a, the rate capabilities of the c-WO_x/C, c-WO_x/C-WS_2/C, and c-WS_2/C electrodes were tested under different current densities ranging from 100 to 250, 500, and 1000 mA g^{-1}. The c-WS_2/C electrode delivers average specific discharge/charge capacities of 440, 360, 300, and 250 mAh g^{-1}, respectively. As the current density is returned to 100 mAg^{-1}, the specific discharge/charge capacity quickly recovers to 435 mAh g^{-1}. Similar superior rate performances are also observed for the c-WO_x/C-WS_2/C electrode which shows slightly higher average specific discharge/charge capacities of 500, 420, 380, and 320 mAh g^{-1}, respectively, at the same current densities. Consequently, both the c-WS_2/C and c-WO_x/C-WS_2/C electrodes display high reversibility and excellent rate capability. By comparison, the c-WO_x/C electrode exhibits slightly inferior rate capability, delivering specific capacities of 550, 420, 280, and 220 mAh g^{-1}, respectively.

Motivated by the excellent stability and rate performance of the c-WS_2/C electrode, its long-term stability was evaluated at a high current density of 500 mA g^{-1}. Remarkably, as shown in Figure 73b, even over 500 cycles, a high capacity retention of 97% is obtained and the electrode delivers a capacity of 307 mAh g^{-1}.

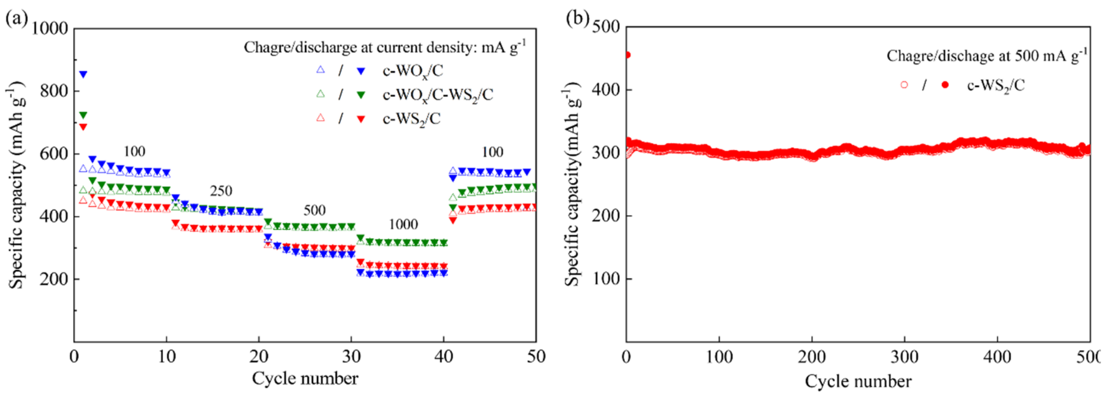

Figure 73. Rate performance of the above electrodes at the current densities ranging from 100 to 1000 mA g^{-1} for the c-WO_x/C, c-WO_x/C-WS_2/C, and c-WS_2/C electrodes (a) and long-term cycling performance of c-WS_2/C at a high current density of 500 mA g^{-1}(b) [163]. Hollow and solid circles stand for charge and discharge capacities, respectively.

4.5. PVP-based WO_x and WS_2 carbon composites for lithium storage

To confirm the general applicability of the presented preparation method, in this chapter, PVP was used as an alternative carbon source to prepare carbon-coated tungsten-based oxide and disulfide. In analogy to the case of CTAB, p-WO_x/C was first synthesized via a hydrothermal and carbonization process, and then sulfurized at 600 and 800 °C to be converted into p-WO_x/C-WS_2/C and p-WS_2/C, respectively.

4.5.1 Physical characterization

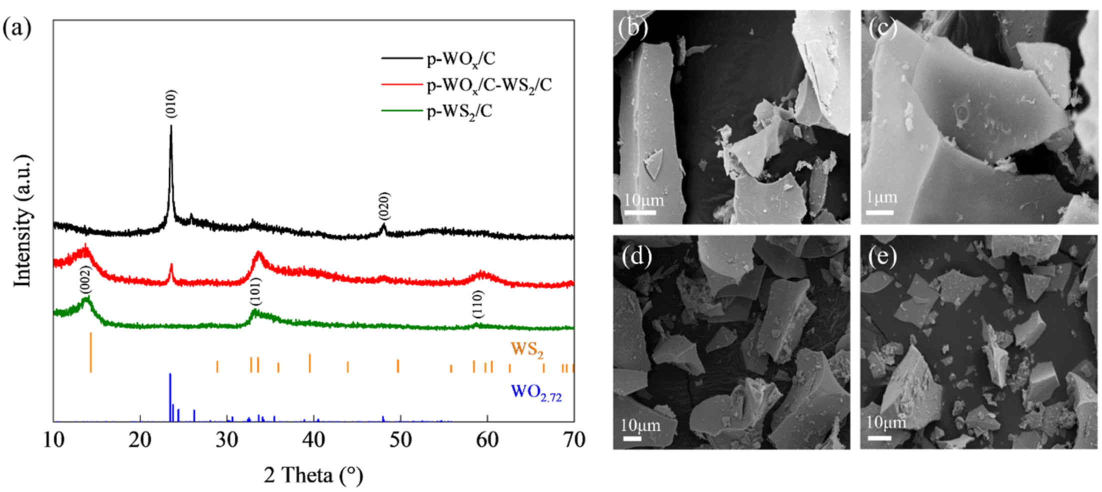

Figure 74. (a) XRD patterns of p-WO_x/C, p-WO_x/C-WS_2/C (sulfurization at 600 °C), and p-WS_2/C (sulfurization at 800 °C) [163]. Vertical ticks show the reference patterns according to ICSD code 202366 [186] (WS_2) and ICSD code 15254 [183] ($WO_{2.72}$), respectively. (b-e) SEM images of (b, c) p-WO_x/C, (d) p-WO_x/C-WS_2/C, and (e) p-WS_2.

Figure 74a shows the XRD patterns of p-WO_x/C, p-WO_x/C-WS_2/C, and p-WS_2/C. In the case of p-WO_x/C, two main peaks at 23° and 48° are observed, corresponding to the (010), and (020) planes of $WO_{2.72}$, respectively. It is noteworthy that, similar to CTAB, PVP works as a carbon source as well as a reducing agent. After sulfurization of p-WO_x/C at 600°C, three new peaks located at 13°, 32°, and 60° appeared which are attributed to the (002), (102), and (110) planes of WS_2. When the sulfurization temperature was elevated to 800°C, the peaks characteristic of $WO_{2.72}$ disappeared, while the peaks characteristic of WS_2 remained. It can be concluded that the use of CTAB and PVP results in similar products, which confirms the general character of the preparation method.

Some differences were however observed. In contrast to the regular structure of the c-WO_x/C particles, the morphology of p-WO_x/C turned out to be quite irregular, exhibiting microparticles ranging from 2 to 50 µm as well as some microplates (Figures 74b, c). It is notable that this irregular morphology is maintained after sulfurization to p-WO_x/C-WS_2/C and p-WS_2/C (Figures 74d, e), which differs noticeably from the behavior of the CTAB-based composites, for which the morphology changed from nanorods to nanosheets after the sulfurization.

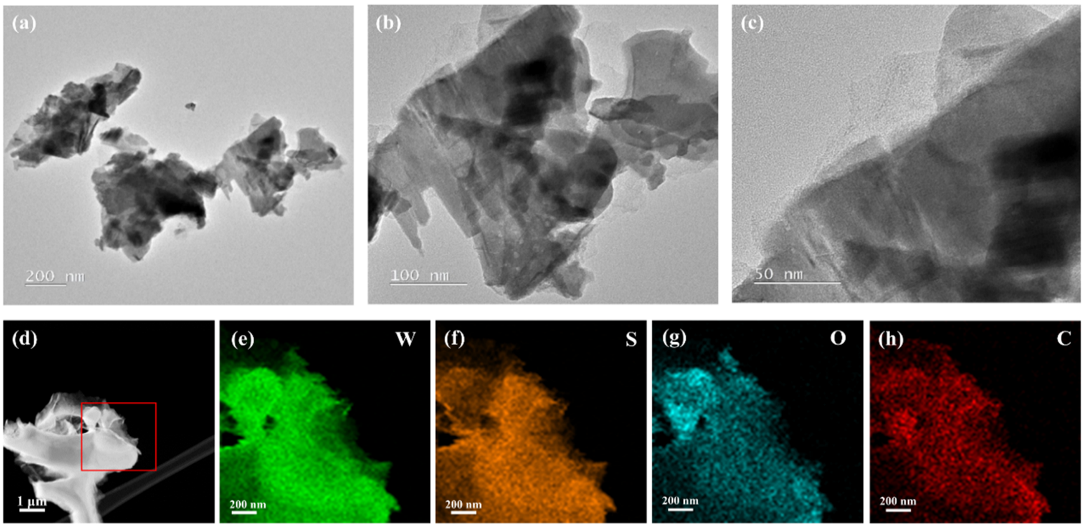

Figure 75. TEM images (a), HR-TEM images (b-d), and elemental mapping images (e-h) of p-WOx-WS_2/C (sulfurized at 600 °C) [163].

Figure 75 exhibits TEM, HR-TEM, and elemental mapping images of p-WOx-WS_2/C (sulfurized at 600 °C). The irregular p-WO_x-WS_2/C particles shown in Figures 75a-c confirm the result of the SEM data. Moreover, TEM-EDS mappings in the selected area in Figure 75d (red square) (Figures 75e-h), show a uniform distribution of the elements, including W, O, S, and C in p-WO_x/C-WS_2/C.

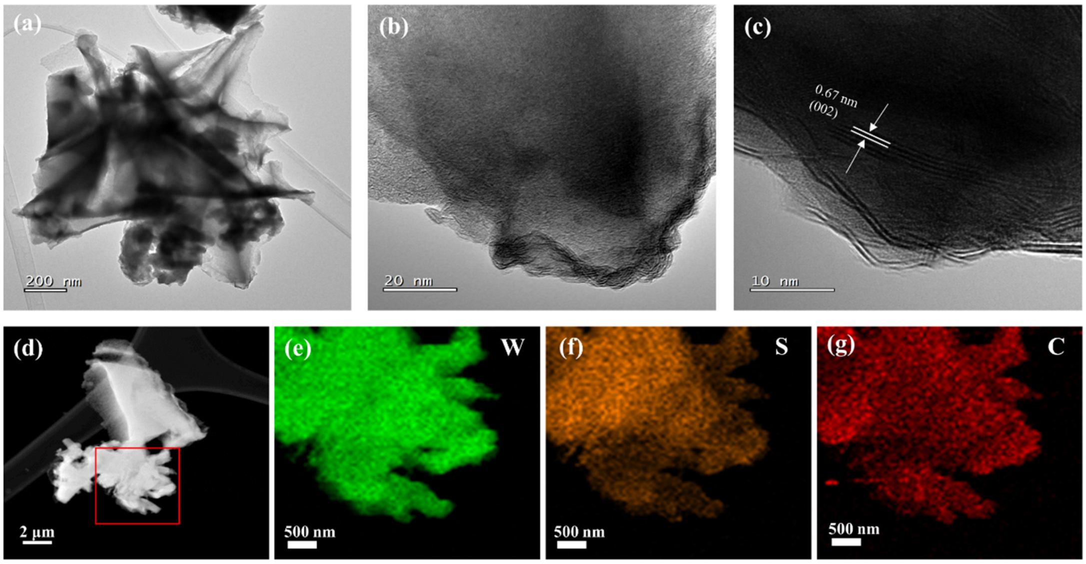

Figure 76. TEM images (a), HR-TEM images (b-d), and elemental mapping images (e-g) of p-WS_2/C (sulfurized at 800 °C) [163].

The p-WS_2/C composite shows similar morphology to that of p-WO_x/C-WS_2/C (Figures 75, 76). The lattice fringe in p-WS_2/C shown in the HRTEM image (Figure 76c) exhibits an interlayer spacing of 0.675 nm, corresponding to the (002) plane of WS_2, which is in accordance with the XRD data of p-WS_2/C. Figures 76e-g show the EDS-mapping of the selected area from Figure 76d, implying a homogeneous distribution of W, S, and C in the p-WS_2/C composite.

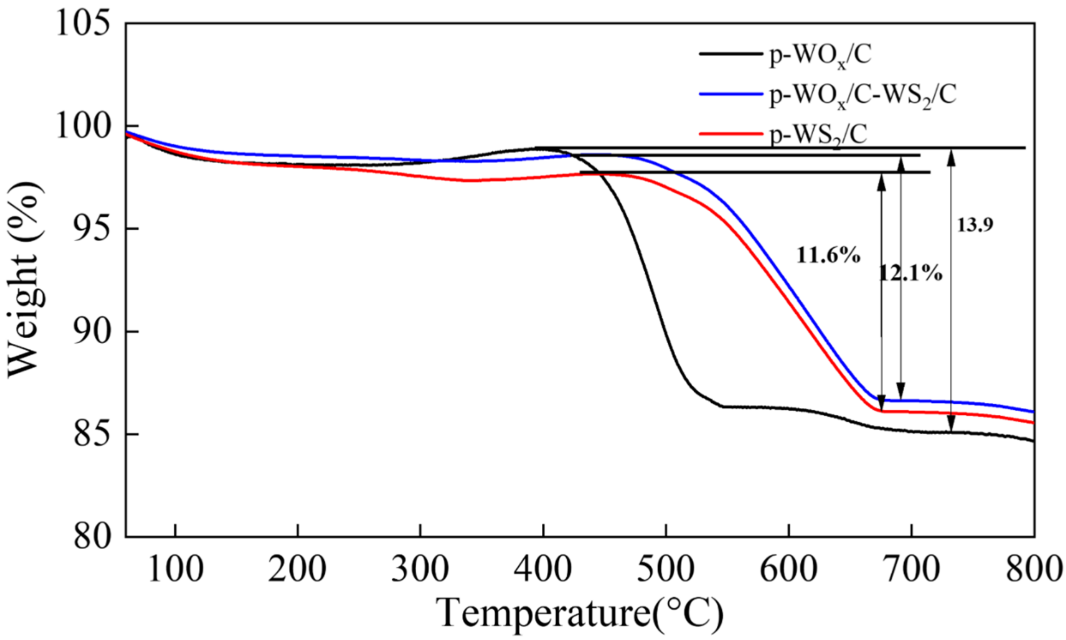

Figure 77. TGA curves of p-WO_x/C, p-WO_x/C-WS_2/C, and p-WS_2/C [163].

TGA was performed to evaluate the carbon content of three composites. As shown in Figure 77, TGA curves of p-WO_x/C, p-WO_x/C-WS_2/C, and p-WS_2/C shared similar shapes with the counterparts of the CTAB-assisted composites. The carbon contents in p-WO_x/C, p-WO_x/C-WS_2/C, and p-WS_2/C amount to 11.6, 13.9, and 12.1 wt%, respectively (±0.5). Accordingly, we conclude that PVP provides more carbon coating than CTAB under similar preparation conditions.

4.5.2 Electrochemical characterization

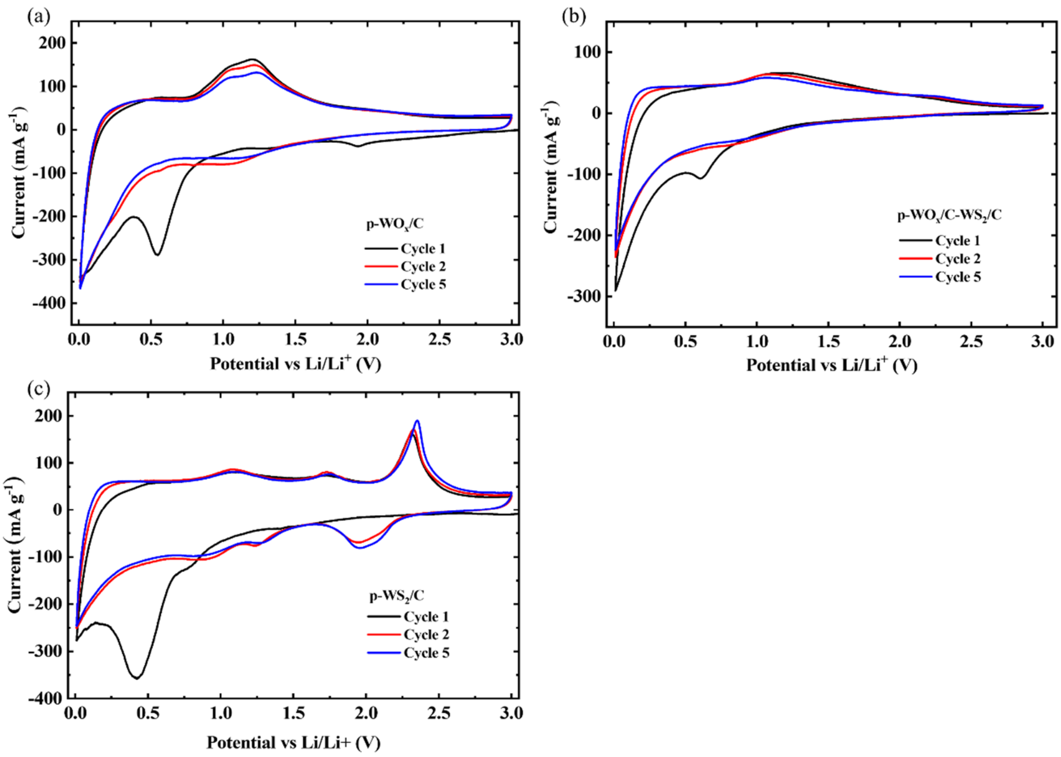

Figure 78. CV curves for (a) p-WO_x/C, (b) p-WO_x/C-WS_2/C, and (c) p-WS_2/C electrodes for the first, second, and fifth cycles at a scan rate of 0.1 mV s^{-1} in a potential range of 0.01–3 V versus Li/Li^+ [163].

The electrochemical behavior of p-WO_x/C, c-WO_x/C-WS_2/C, and p-WS_2/C electrodes, as studied by CV and GCPL measurements, are very similar to the materials obtained by the CTAB-assisted syntheses (Figures 78, 79). Nonetheless, the CV curve of the p-WO_x/C-WS_2/C electrode exhibits some differences in the peak intensities. The redox peaks at 1.8 and 2.3 V, corresponding to the electrochemical process of WS_2, are much weaker than those for the CTAB-assisted syntheses, indicating that not WS_2 but WO_x makes the largest contribution to the electrochemical behavior. This might be because the degree of sulfurization for p-WO_x/C-WS_2/C is lower than that for c-WO_x/C-WS_2/C at the same sulfurization temperature. To increase this degree, the sulfurization temperature should be increased. This point might be investigated in the future.

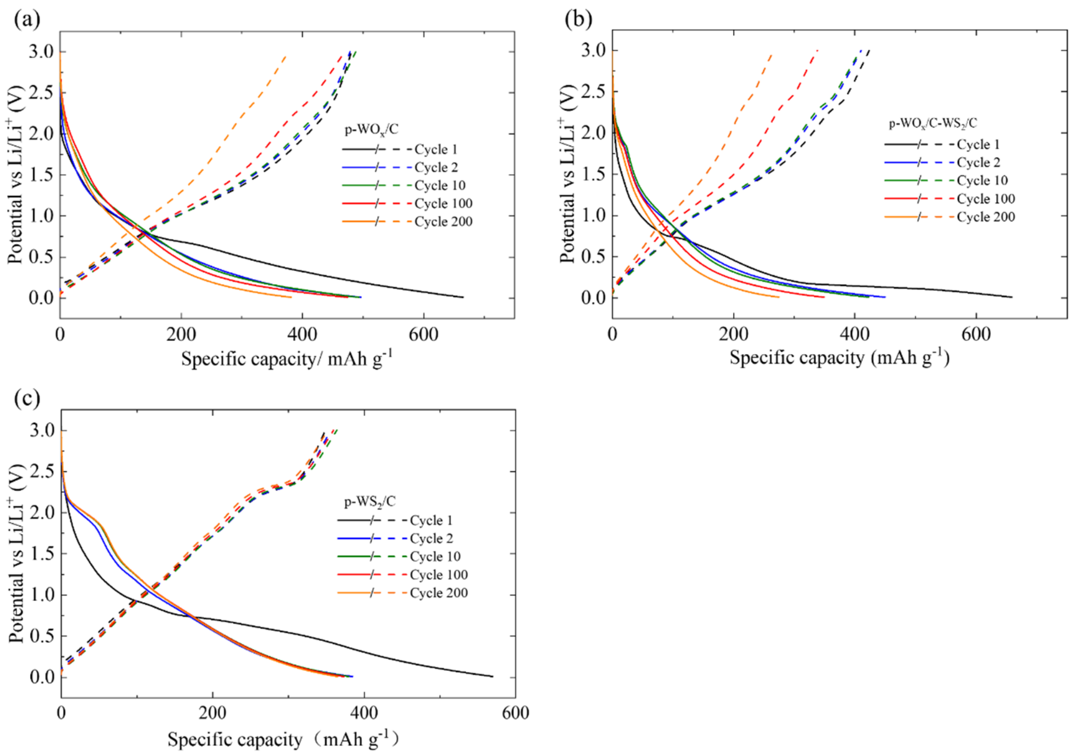

Figure 79. Galvanostatic discharging/charging curves of the p-WO_x (a), p-WO_x-WS_2/C, (b) and p-WS_2/C (c) electrodes at a current density of 100 mA g^{-1} for specific cycles [163].

The cycling performance of pristine WO_3, p-WO_x/C, p-WO_x/C-WS_2/C, and p-WS_2/C electrodes was studied, and the results are shown in Figure 80. Compared with the pristine WO_3 electrode, the p-WO_x/C electrode delivers a lower initial discharge/charge specific capacity of 660/480 mAh g^{-1} but exhibits more stable cycling performance (80% capacity retention after 200 cycles) at 100 mA g^{-1}. The mixed-phase p-WO_x/C-WS_2/C electrode, however, does not show an obvious improvement in battery performance compared with the p-WO_x/C electrode. It delivers an initial discharge/charge specific capacity of 630/440 mAh $g^{-1}$and a capacity retention of 67% after 200 cycles at 100 mA g^{-1}. In the case of the CTAB-assisted mixed-phase, c-WO_x/C-WS_2/C, the big improvement in the cycling stability was explained by the synergetic effect of c-WO_x/C and c-WS_2/C. However, the micro-scale structure of p-WO_x/C-WS_2/C might mitigate the impact of this effect and lead to worse capacity retention. As p-WO_x/C completely converted to p-WS_2/C at 800 °C, the p-WS_2/C electrode delivers a comparatively low initial discharge/charge specific capacity of 654/420 mAh g^{-1} but shows excellent stability, viz. capacity retention of 90% after 200 cycles at 100 mA g^{-1}.

.

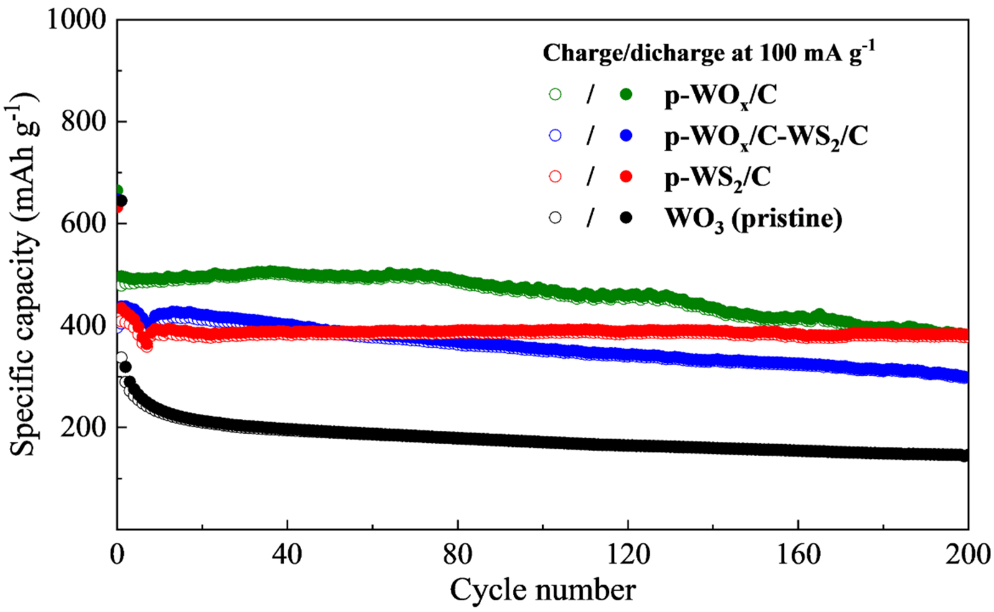

Figure 80. Cycling performance for p-WO_x/C, p-WO_x/C-WS_2/C, and p-WS_2/C electrodes at a current density of 100 mA g^{-1}. The values for the pristine WO_3 are shown for comparison [163]. Hollow and solid circles stand for charge and discharge capacities, respectively.

To evaluate the rate capabilities, the p-WO_x/C, p-WO_x/C-WS_2/C, and p-WS_2/C electrodes were cycled at various current densities ranging from 100 mA g^{-1} to 1000 mA g^{-1} with 10 cycles for each (Figure 81a). The p-WO_x/C and p-WO_x/C-WS_2/C electrodes show a pronounced capacity decrease along with increasing current densities. In contrast, the p-WS_2/C electrode exhibits an excellent rate performance, delivering high reversible capacities of 390, 280, 200, and 150 mAh g^{-1} and fast recovering to 360 mAh g^{-1} as the current density returns to 100 mA g^{-1}. In addition, the long-life cycling performance of the p-WS_2/C electrode was tested at a current density of 500 mA g^{-1} to further verify its cycling stability. As displayed in Figure 81b, a capacity retention of 80% is attained after 500 cycles, suggesting a superior cycling performance.

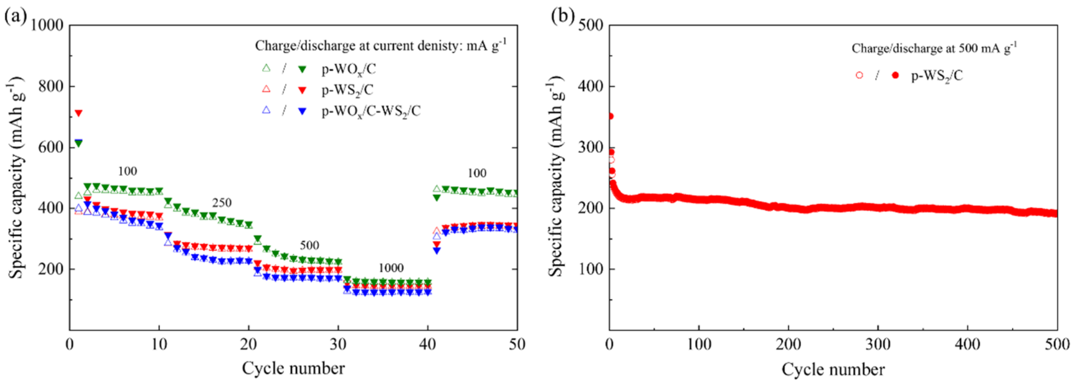

Figure 81. Rate performance of the above electrodes at current densities ranging from 100 to 1000 mA g^{-1} for the p-WO_x/C, p-WO_x/C-WS_2/C, and p-WS_2/C electrodes (a), and long-term cycling performance of p-WS_2/C at a high current density of 500 mA g^{-1}(b) [163]. Hollow and solid circles stand for charge and discharge capacities, respectively.

In the context of the above results, it is worth noting that CTAB works as a growth controller, setting a preferential orientation of WO_x and causing the formation of nanorods[195]. The subsequent sulfurization process leads to the growth of WS_2 nanosheets. These unique nanostructures can not only provide a shorter lithium ion diffusion path but also assure a larger electrode-electrolyte contact area. As a consequence, a higher capacity is obtained. Regretfully, such a favorable morphology is not characteristic in the PVP case, resulting in inferior capacity. Howver, for both CTAB and PVP, functional composites were successfully synthesized emphasizing the broad applicability of the proposed method for high-performance lithium storage.

4.6 Conclusion

In summary, we developed a facile and useful method for the synthesis of carbon-coated tungsten oxides and disulfides. Two kinds of carbon sources (PVP and CTAB), were adopted to obtain WO_x/C, WS_2/C, and mixed-phase, WO_x/C-WS_2/C composites. The respective composite electrodes exhibit excellent lithium-ion battery performance. Specifically, the c-WO_x/C electrode delivers a high initial discharge/charge capacity of 840/560 mAh g^{-1} at 100 mA g^{-1} and a 74% capacity retention after 200 cycles. Significantly, the c-WO_x/C-WS_2/C and c-WS_2/C electrodes show outstanding cycling stability with capacity retention of 99% and 95% respectively, after 200 cycles at 100 mA g^{-1}. Besides, the c-WS_2/C electrode also features a capacity retention of 97% after 500 cycles at a high current density of 500 mA g^{-1}. In addition, the p-WO_x/C, p-WS_2/C, and WO_x/C-WS_2/C electrodes exhibit high potential for high-performance lithium-ion storage. In particular, p-WS_2/C shows a capacity retention of 80% after 500 cycles at 500 mA g^{-1}. Hence, the proposed fabrication method provides a simple and low-cost way to prepare carbon-coated tungsten oxides and disulfides, useful in the context of high-performance lithium storage.

5. Summary and Outlook

The work in this thesis investigate advanced metal based materials as alternative anode materials for LIBs. In Chapter 3, pristine transition metal carbides (MXenes) and their composites were synthesized and studied physically and electrochemically. In Chapter 3.2, Ti_3C_2, a standard MXene, was firstly synthesized via two types of methods, i.e. the conventional HF etching process and the HCl+LiF mixture assisted hydrothermal etching process. The hydrothermal environment as well as the fresh HF generated from the HCl+LiF mixture ensure the production of Ti_3C_2 with fewer impurities and a more open structure compared to that from conventional method. When used as anode materials for LIBs, both synthesized Ti_3C_2 exhibit low specific capacity of less than 200 mAh g^{-1} at a current density of 100 mA g^{-1}, while the Ti_3C_2 from the HCl+LiF mixture (m-Ti_3C_2) presents better cycling stability after 75 cycles, which might be due to the existence of fewer impurities and fewer –F surface groups in the m-Ti_3C_2 sample. Consistently, the V_2C and Nb_2C materials prepared by the HCl+LiF etching exhibit excellent cycling performance over 100 cycles. As summarized in Table 1, although good cycling stability was achieved for MXene synthesized by HCl+LiF etching, the specific capacity is quite low, even compared to commercial anode material (graphite: 372 mAh g^{-1}).

Active material	Initial discharge/charge capacity (mAh g^{-1})	Current (mA g^{-1})	Cycle number	Capacity (mAh g^{-1})
Ti_3C_2 (HF)	325/172	100	75	112
Ti_3C_2 (LiF+HCl)	372/188	100	75	185
Nb_2C (LiF+HCl)	346/216	100	100	160
V_2C (LiF+HCl)	327/168	100	100	212

Table 1. Summary of the electrochemical performance of various synthesized MXenes in LIBs.

Hence, it is still imperative to enhance the capacity of pristine MXene. There are three promising approaches to solve this problem: 1. Surface group modifications of MXenes with metal ions, large organic molecules intercalation. After surface group modification, the surface groups on the MXene might be changed to an individual surface group that is beneficial for lithium diffusion. Metal ion or large organic molecule intercalation will enlarge the interlayer distance of MXene for fast lithium diffusion and extra storage sites. 2. A new synthesis method for the preparation of MXenes without surface groups would be an effective way to improve their lithium storage performance. 3. Integreting MXenes with other high-capacity anode materials. As the most efficient approach, composite construction can take advantage of each component for battery application.

In Chapter 3.3, commercial MoO_3 and synthesized Nb_2C were for the first time used to form MoO_3/Nb_2C composites via a simple ball-milling method. The effect of important experimental conditions including ball-milling time, ball-milling speed, and the mass ratio of components on the morphology, crystallinity, and lithium storage performance of MoO_3/Nb_2C was studied. As a result, changes in ball-milling time and ball-milling speed have no impact on the morphology and crystallinity of MoO_3/Nb_2C. Thus, there is also no obvious enhancement of these composites for lithium storage compared to pristine Nb_2C and commercial MoO_3 (Table 2). For the composites with various mass ratio, the SEM images show that the MoO_3 microplates are mainly embedded into the open structure of Nb_2C in the MoO_3/Nb_2C composite with the mass ratio of 1:1 (1:1-MoO_3/Nb_2C), while excessive individual MoO_3 and Nb_2C are observed in the MoO_3/Nb_2C composites with the mass ratio of 2:1 and 1:1, respectively, demonstrating a good combination of the two components in the 1:1-MoO_3/Nb_2C composite. Therefore, the 1:1-MoO_3/Nb_2C composite exhibits enhanced battery performance that a specific capacity of 267 mAh g^{-1} is achieved after 300 cycles at a current density of 100 mA g^{-1}, which is two times higher than that of commercial MoO_3 (Table 2). The CV results of the MoO_3/Nb_2C composites with different mass ratios reveal that after several cycles, the degradation of the formed MoO_x phase is significantly suppressed in 1:1-MoO_3/Nb_2C due to the favorable combination of two components, causing a stable lithiation/delithiation process.

This work provides a simple and scalable way to prepare composites of Nb_2C MXene and commercial MoO_3 for enhanced lithium storage performance. The improved capacity, however, is still limited, also compared with the commercial anode materials e.g. graphite with 372 mAh g^{-1}. In consideration of the large size (micrometers) of commercial MoO_3, one can prepare nanosized MoO_3 and integrate it with MXenes by a ball-milling process. Besides, instead of the ball-milling method, synthesis methods such as the hydrothermal and the sol-gel method are suggested to realize in-situ growth of MoO_3 in MXenes layered structure.

Active material	Initial discharge/ charge capacity (mAh g^{-1})	Current (mA g^{-1})	Cycle number	Capacity (mAh g^{-1})
Pristine Nb_2C	341/217	100	120	160
Commercial MoO_3	978/630	100	50	125
MoO_3/Nb_2C (ball-milling time 6 h)	746/483	100	50	153
MoO_3/Nb_2C (ball-milling time 12 h)	691/461	100	50	150
MoO_3/Nb_2C (ball-milling speed 200 rpm)	743/485	100	50	157
MoO_3/Nb_2C (ball-milling speed 300 rpm)	724/471	100	50	172
MoO_3/Nb_2C (ball-milling speed 400 rpm)	860/530	100	50	132
MoO_3/Nb_2C (mass ratio of 2:1)	746/483	100	50	151
MoO_3/Nb_2C (mass ratio of 1:1)	694/412	100	300	267
MoO_3/Nb_2C (mass ratio of 1:2)	589/392	100	50	154

Table 2. Summary of the electrochemical performance of MoO_3/Nb_2C composites synthesized at different ball-milling times, ball-milling speeds, and mass ratios of MoO_3 and Nb_2C in LIBs.

To further utilize the unique accordion-like structure of MXene and improve its lithium storage performance, in Chapter 3.4, $MoO_2/C/V_2C$ composites were fabricated for the first time for high-performance lithium storage. During the synthesis process, the positively charged polymer, PDDA, was introduced to combine with negatively charged V_2C in the aqueous solution via electrostatic force. The introduction of PDDA can not only stabilize V_2C in aqueous solution but also make it positively charged for following growth in the hydrothermal process. With the delicate experimental design, the synthesized $MoO_2/C/V_2C$ composites exhibit hierarchical structures, where MoO_2 nanoparticles are distributed uniformly in the accordion-like structure of V_2C/C. When used as anode materials for LIBs, the $MoO_2/C/V_2C$ composites exhibit a high capacity of 810 mAh g^{-1} after 100 cycles at a current density of 100 mA g^{-1}. Even at a high current density of 1000 mA g^{-1}, a capacity of 605 mAh g^{-1} is obtained for the $MoO_2/C/V_2C$ composite. The superior battery performance of the $MoO_2/C/V_2C$ composites may have several reasons: 1. The short lithium ion diffusion path caused by the hierarchical structure and nanosized MoO_2, as well as the enhanced electronic conductivity of the $MoO_2/C/V_2C$ composites due to the presence of high conductive V_2C ensure the fast charge transfer, resulting in the outstanding rate performance. 2. Since the MoO_2 nanoparticle are confined in the open structure of V_2C, the large volume expansion of MoO_2 can be buffered during the cycling process, causing excellent cycling stability. The approach adopted in this work provides a facile and simple way to better use the open structure of MXene for structure design of composites for high performance LIBs. Moreover, as shown in Table 3, compared to various other reported MXenes composites, the hierarchical structure of $MoO_2/C/V_2C$ composites in this work exhibit superior rate capability and better cycling stability.

Active material	Current (mA g^{-1})	Cycle number	Capacity (mAh g^{-1})	Ref.
Si@V_2C composites	200	150	443	61
MoS_2@C/V_2C composites	200	300	870	152
SnS_2/Sn_3S_4 hybrid/Ti_3C_2	100	100	463	196
SnO_2 quantum dots/Ti_3C_2 composite	100	100	655	197
Hierarchical structure of $MoO_2/C/V_2C$ composites	100	100	810	This work
	1000	400	605	

Table 3. Summary of electrochemical performance of MXenes composites in LIBs.

In Chapter 4, composites of metal oxides and sulfides with carbon is investigated via a simple and low-cost way by taking carbon coated tungsten based oxides and disulfides as an example. Unlike other reports using expensive carbon sources and complex synthesis methods, this work adopts low-cost carbon sources (CTAB and PVP) and a simple hydrothermal process followed by sulfurization to obtain carbon coated tungsten oxides (WO_x/C) and tungsten disulfides (WS_2/C). The XRD results confirm the phase transition from WO_x/C to the mixed phase WO_x/C-WS_2/C and then to WS_2/C after the sulfurization process at different temperatures. When used as anode materials for LIBs, the CTAB assisted WO_x/C (c-WO_x/C), the mixed phase WO_x/C-WS_2/C (c-WO_x/C), and the WS_2/C (c-WS_2/C) show specific capacities of 420, 525 and 460 mAh g^{-1}, respectively after 200 cycles at a current density of 100 mA g^{-1}, which are much higher than that of pristine WO_x and WS_2. The c-WS_2/C composite shows a superior long-term cycling stability that a capacity retention of 97% (307 mAh g^{-1}) is observed after 500 cycles at a current density of 500 mA g^{-1}. Compared to other various tungsten oxide and sulfide carbon composites for LIBs, the carbon coated tungsten oxides and sulfides in this work possess comparable specific capacities and longer cycling stability in both low and high current density (Table 4). Moreover, PVP-assisted WO_x/C (p-WO_x/C), the mixed phase WO_x/C-WS_2/C (p-WO_x/C) and WS_2/C (p-WS_2/C) are prepared at the same experimental condition to prove the general applicability of the developed synthesis methods. The PVP-assisted tungsten oxide and disulfide also display enhanced battery performance compared to pristine pristine WO_x and WS_2. In particular, the p-WS_2/C electrode exhibits a capacity retention of 80% after 500 cycles at a current density of 500 mA g^{-1}, indicating an outstanding cycling performance.

Active material	Current (mA g^{-1})	Cycle number	Capacity (mAh g^{-1})	Ref.
WO_{3-x}/C nanosheets	200	100	662	172
m-WO_x /C	250	100	443	173
Cauliflower-like WO_3@C composites	50	50	650	198
WS_2/carbon nanotube-reduced graphene oxide	200	100	556	79
Polygonal WS_2@graphene multilayer films	100	100	430	199
WS_2@Super P nanocomposites	100	200	389	200
WS_2 nanoflowers@carbon nanotube vines	1000	140	455	201
WS_2 nanosheets@cabon composites	100	100	322	202
Carbon coated WO_x Carbon coated WO_x-WS_2 Carbon coated WS_2	100 100 100/500	200 200 200/500	420 525 460/307	This work

Table 4. Summary of electrochemical performance of various tungsten oxide and sulfide composites in LIBs.

6. Appendix

6.1 Abbreviations

α-MoO_3	orthorhombic MoO_3
h-MoO_3	hexagonal MoO_3
r-WO_3	monoclinic WO_3
CNF	carbon nanofiber
CNT-rGO	carbon nanotube- reduced graphene oxide
CNTs	carbon nanotubes
CTAB	Cetyltrimethylammonium bromide
CV	Cyclic voltammetry
DMC	Dimethyl carbonate
EC	Ethylene carbonate
ED	Energy dispersive
EDS	Energy dispersive spectroscopy
EDX	Energy dispersive X-ray
ESEM	Environmental scanning electron microscopy
EVs	Electric vehicles
GCPL	Galvanostatic cycling with potential limitation
GCNF	graphene carbon nanofiber
HADDF	High-angle annular dark-field
HRTEM	High-resolution transmission electron microscopy
HT	Hydrothermal

ICSD	Inorganic Crystal Structure Database
LIB	Lithium ion battery
LIBs	Lithium ion batteries
LSV	linear sweep voltammetry
M	mole per liter
m-$W_{18}O_{49}$	mesoporous $W_{18}O_{49}$
Ni-Cd	Nickel-cadmium
Ni-MH	Nickle-metal hybrid
NMP	N-methyl-2-pyrrolidone
NB	nanobelt
NR	nanorod
NW	nanowire
PDDA	Polydiallyldimethylammonium chloride
PVP	Polyvinyl pyrrolidone
PTFE	Polytetrafluoroethylene
PVDF	Polyvinylidene difluoride
ppm	parts per million
PXRD	Powder X-ray diffraction
Ref	Reference
rpm	revolutions per minute
SEM	Scanning electron microscopy
STEM	Scanning transmission electron microscopy
SEI	Solid electrolyte interphase

TEM	Transmission electron microscopy
TGA	Thermogravimetric analysis
TMAOH	Tetramethylammonium hydroxide
Wt%	weight percent
XPS	X-ray photoelectron spectroscopy

6.2 Electrochemical performance for commercial MoO_3

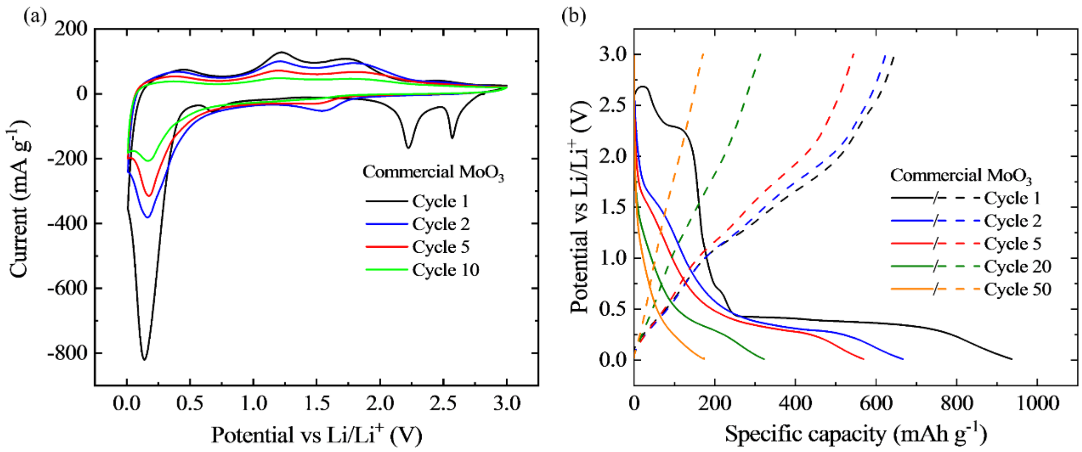

Figure 82. CV curve (a) and Galvanostatic charge/discharge curve (b) of the commercial MoO_3 electrode at a current density of 100 mA g^{-1} for the specific cycles [138].

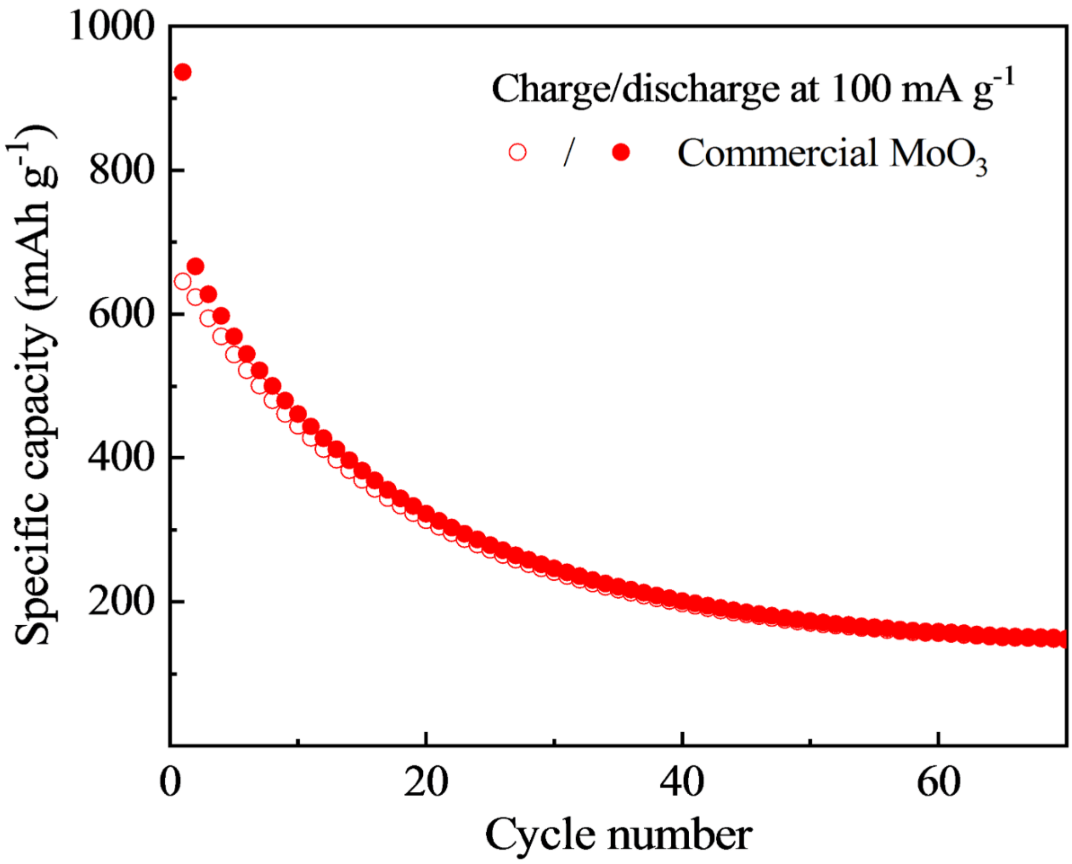

Figure83. Cycling performance of commercial MoO_3 electrode at a current density of 100 mA g^{-1} in the range of 0.01-3.00 vs. Li/Li^+ [138]. Hollow and solid circles stand for charge and discharge capacities, respectively.

6.3 CV and GCPL results for 300-MoO_3/Nb_2C and 400-MoO_3/Nb_2C composites

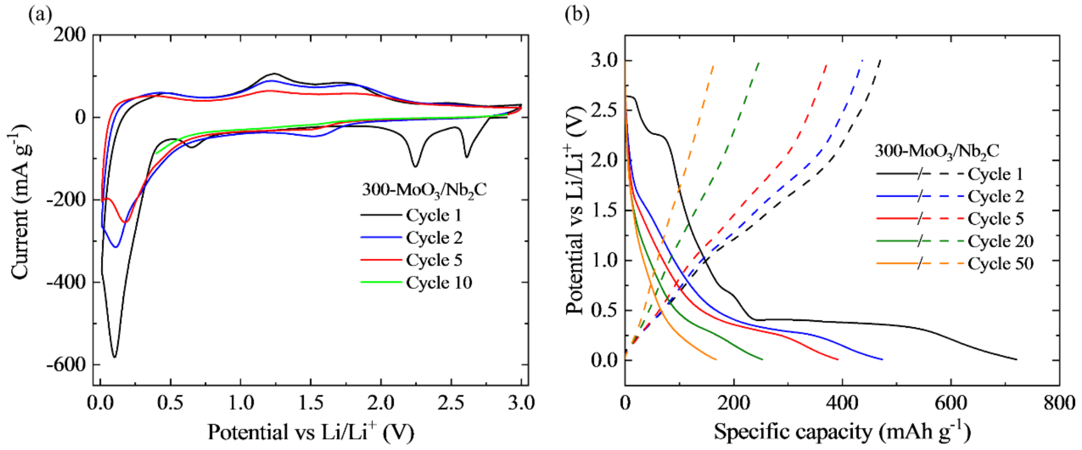

Figure 84. CV curve (a) and Galvanostatic charge/discharge curve (b) of the 400-MoO_3/Nb_2C electrode at a current density of 100 mA g^{-1} for the specific cycles [138].

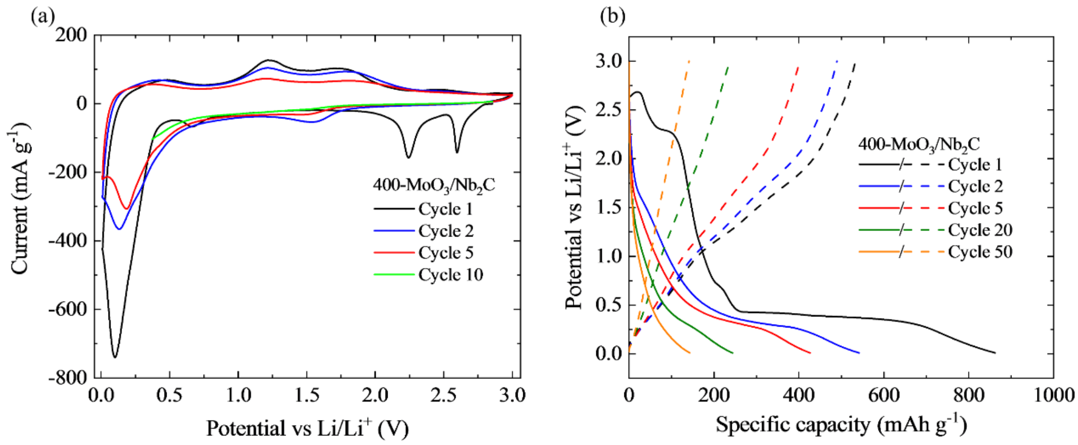

Figure 85. CV curve (a) and Galvanostatic charge/discharge curve (b) of the 400-MoO_3/Nb_2C electrode at a current density of 100 mA g^{-1} for the specific cycles [138].

6.4 CV and GCPL results for MoO_3/Nb_2C (6h) and MoO_3/Nb_2C (24h) composites

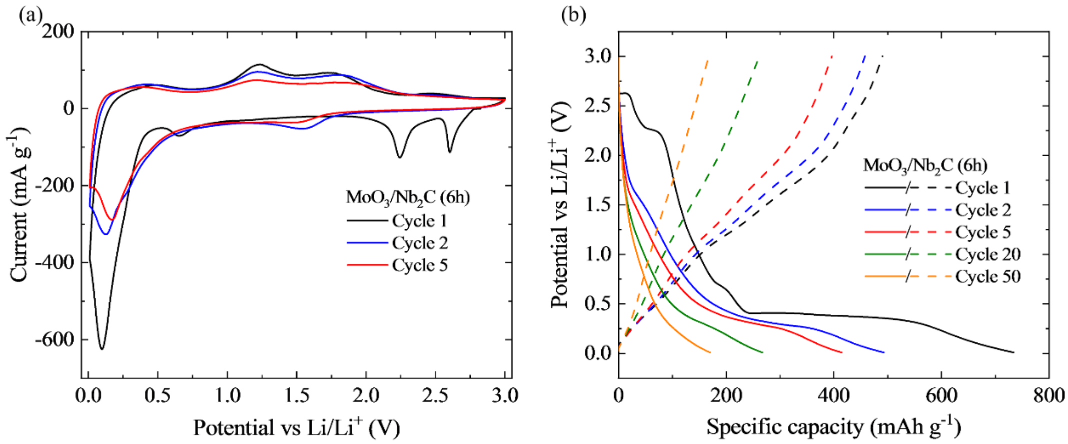

Figure 86. CV curve (a) and Galvanostatic charge/discharge curve (b) of the MoO_3/Nb_2C (6h) electrode at a current density of 100 mA g^{-1} for the specific cycles [138].

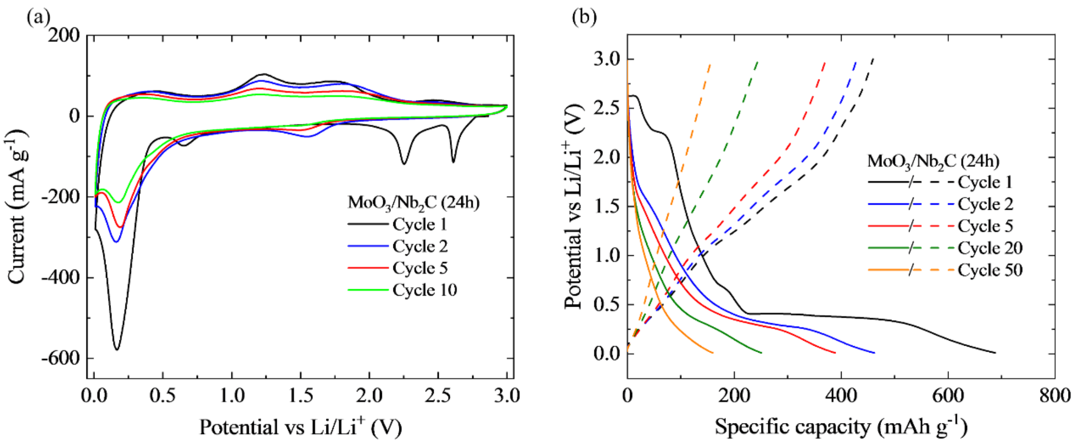

Figure 87. CV curve (a) and Galvanostatic charge/discharge curve (b) of the MoO_3/Nb_2C (24h) electrode at a current density of 100 mA g^{-1} for the specific cycles [138].

6.5 CV and GCPL results for 2:1-MoO_3/Nb_2C, 1:1-MoO_3/Nb_2C and 1:2-MoO_3/Nb_2C composites

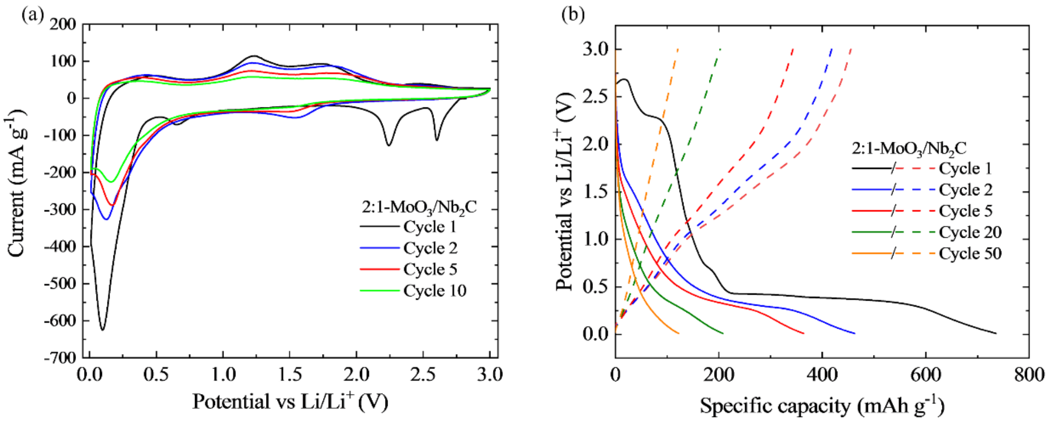

Figure 88. CV curve (a) and Galvanostatic charge/discharge curve (b) of the 2:1-MoO_3/Nb_2C electrode at a current density of 100 mA g^{-1} for the specific cycles [138].

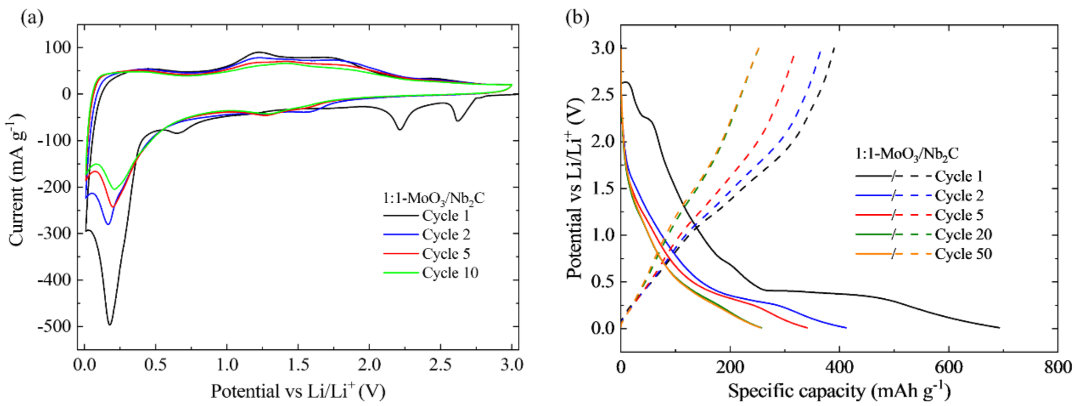

Figure 89. CV curve (a) and Galvanostatic charge/discharge curve (b) of the 1:1-MoO_3/Nb_2C electrode at a current density of 100 mA g^{-1} for the specific cycles [138].

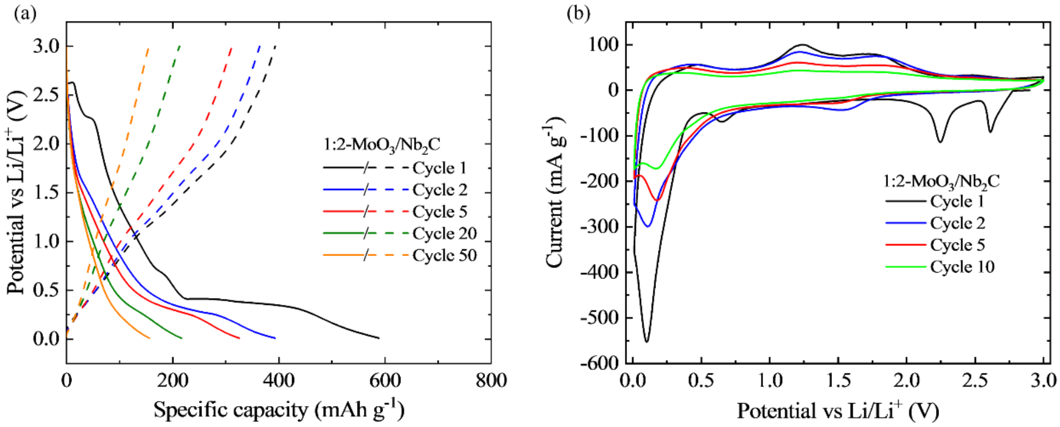

Figure 90. CV curve (a) and Galvanostatic charge/discharge curve (b) of the 1:2-MoO_3/Nb_2C electrode at a current density of 100 mA g^{-1} for the specific cycles [138].

7. References

[1] Z. Yang, J. Zhang, M.C. Kintner-Meyer, X. Lu, D. Choi, J.P. Lemmon, J. Liu, Electrochemical energy storage for green grid, Chem. Rev. 111 (2011) 3577-3613.

[2] M. Armand, J.-M.J.n. Tarascon, Building better batteries, Nature 451 (2008) 652-657.

[3] B.J.N. Scrosati, Challenge of portable power, Nature 373 (1995) 557-558.

[4] B. Dunn, H. Kamath, J.M. Tarascon, Electrical energy storage for the grid: a battery of choices, Science 334 (2011) 928-935.

[5] D. Larcher, J.M. Tarascon, Towards greener and more sustainable batteries for electrical energy storage, Nat Chem 7 (2015) 19-29.

[6] J. David, Nickel-cadmium battery recycling evolution in Europe, J. Power Sources 57 (1995) 71-73.

[7] H. Cheng, J.G. Shapter, Y. Li, G. Gao, Recent progress of advanced anode materials of lithium-ion batteries, J. Energy Chem 57 (2021) 451-468.

[8] M. Li, J. Lu, Z. Chen, K. Amine, 30 Years of Lithium-Ion Batteries, Adv. Mater. (2018) e1800561.

[9] G. Zubi, R. Dufo-López, M. Carvalho, G. Pasaoglu, The lithium-ion battery: State of the art and future perspectives, Renewable and Sustainable Energy Reviews 89 (2018) 292-308.

[10] Y. Liang, C.Z. Zhao, H. Yuan, Y. Chen, W. Zhang, J.Q. Huang, D. Yu, Y. Liu, M.M. Titirici, Y.L. Chueh, H. Yu, Q. Zhang, A review of rechargeable batteries for portable electronic devices, InfoMat 1 (2019) 6-32.

[11] W. Chen, J. Liang, Z. Yang, G.J.E.P. Li, A review of lithium-ion battery for electric vehicle applications and beyond, Energy Procedia 158 (2019) 4363-4368.

[12] H. Li, Practical Evaluation of Li-Ion Batteries, Joule 3 (2019) 911-914.

[13] Y. Lu, X. Rong, Y.-S. Hu, L. Chen, H. Li, Research and development of advanced battery materials in China, Energy Storage Materials 23 (2019) 144-153.

[14] H. Hao, X. Cheng, Z. Liu, F. Zhao, China's traction battery technology roadmap: Targets, impacts and concerns, Energy Policy 108 (2017) 355-358.

[15] D. Bresser, K. Hosoi, D. Howell, H. Li, H. Zeisel, K. Amine, S. Passerini, Perspectives of automotive battery R&D in China, Germany, Japan, and the USA, J. Power Sources 382 (2018) 176-178.

[16] J. Amici, P. Asinari, E. Ayerbe, P. Barboux, P. Bayle-Guillemaud, R.J. Behm, M. Berecibar, E. Berg, A. Bhowmik, S. Bodoardo, I.E. Castelli, I. Cekic-Laskovic, R. Christensen, S. Clark, R.

Diehm, R. Dominko, M. Fichtner, A.A. Franco, A. Grimaud, N. Guillet, M. Hahlin, S. Hartmann, V. Heiries, K. Hermansson, A. Heuer, S. Jana, L. Jabbour, J. Kallo, A. Latz, H. Lorrmann, O.M. Løvvik, S. Lyonnard, M. Meeus, E. Paillard, S. Perraud, T. Placke, C. Punckt, O. Raccurt, J. Ruhland, E. Sheridan, H. Stein, J.M. Tarascon, V. Trapp, T. Vegge, M. Weil, W. Wenzel, M. Winter, A. Wolf, K. Edström, A Roadmap for Transforming Research to Invent the Batteries of the Future Designed within the European Large Scale Research Initiative BATTERY 2030+, Adv. Energy. Mater 12 (2022).

[17] J.-M. Tarascon, M.J.n. Armand, Issues and challenges facing rechargeable lithium batteries, Nature 414 (2001) 359-367.

[18] X. Zeng, M. Li, D. Abd El-Hady, W. Alshitari, A.S. Al-Bogami, J. Lu, K. Amine, Commercialization of Lithium Battery Technologies for Electric Vehicles, Adv. Energy. Mater 9 (2019).

[19] A.S. Arico, P. Bruce, B. Scrosati, J.-M. Tarascon, W.J.N.m. Van Schalkwijk, Nat Mater Nanostructured materials for advanced energy conversion and storage devices, 4 (2005) 366-377.

[20] P.U. Nzereogu, A.D. Omah, F.I. Ezema, E.I. Iwuoha, A.C. Nwanya, Anode materials for lithium-ion batteries: A review, Applied Surface Science Advances 9 (2022).

[21] N. Pradeep, E. Sivasenthil, B. Janarthanan, S. Sharmila, A Review of Anode Material for Lithium Ion Batteries, Journal of Physics: Conference Series 1362 (2019).

[22] X. Zuo, J. Zhu, P. Müller-Buschbaum, Y.-J. Cheng, Silicon based lithium-ion battery anodes: A chronicle perspective review, Nano Energy 31 (2017) 113-143.

[23] R. Amine, A. Daali, X. Zhou, X. Liu, Y. Liu, Y. Ren, X. Zhang, L. Zhu, S. Al-Hallaj, Z. Chen, G.-L. Xu, K. Amine, A practical phosphorus-based anode material for high-energy lithium-ion batteries, Nano Energy 74 (2020).

[24] K. Cao, T. Jin, L. Yang, L. Jiao, Recent progress in conversion reaction metal oxide anodes for Li-ion batteries, Materials Chemistry Frontiers 1 (2017) 2213-2242

[25] F. Yao, D.T. Pham, Y.H. Lee, Carbon-Based Materials for Lithium-Ion Batteries, Electrochemical Capacitors, and Their Hybrid Devices, ChemSusChem 8 (2015) 2284-2311.

[26] Y. Lu, L. Yu, X.W. Lou, Nanostructured Conversion-type Anode Materials for Advanced Lithium-Ion Batteries, Chem 4 (2018) 972-996.

[27] F. Dou, L. Shi, G. Chen, D. Zhang, Silicon/Carbon Composite Anode Materials for Lithium-Ion Batteries, Electrochemical Energy Reviews 2 (2019) 149-198.

[28] B. Luo, L. Zhi, Design and construction of three dimensional graphene-based composites for lithium ion battery applications, Energy & Environmental Science 8 (2015) 456-477.

[29] H. Budde-Meiwes, J. Drillkens, B. Lunz, J. Muennix, S. Rothgang, J. Kowal, D.U. Sauer, A review of current automotive battery technology and future prospects, Proceedings of the Institution of Mechanical Engineers, Part D: Journal of Automobile Engineering 227 (2013) 761-776.

[30] R. Tian, S.H. Park, P.J. King, G. Cunningham, J. Coelho, V. Nicolosi, J.N. Coleman, Quantifying the factors limiting rate performance in battery electrodes, Nat Commun 10 (2019) 1933.

[31] J. Lu, Z. Chen, F. Pan, Y. Cui, K. Amine, High-Performance Anode Materials for Rechargeable Lithium-Ion Batteries, Electrochemical Energy Reviews 1 (2018) 35-53.

[32] Z. Li, F. Tian, Y. Li, D. Lei, C. Wang, Zero-Strain Insertion Anode Material of Lithium-Ion Batteries, Small 18 (2022) e2204875.

[33] M. Naguib, M. Kurtoglu, V. Presser, J. Lu, J. Niu, M. Heon, L. Hultman, Y. Gogotsi, M.W. Barsoum, Two-dimensional nanocrystals produced by exfoliation of Ti_3AlC_2, Adv. Mater. 23 (2011) 4248-4253.

[34] M. Naguib, V.N. Mochalin, M.W. Barsoum, Y. Gogotsi, 25th anniversary article: MXenes: a new family of two-dimensional materials, Adv. Mater. 26 (2014) 992-1005.

[35] Z.W. Seh, K.D. Fredrickson, B. Anasori, J. Kibsgaard, A.L. Strickler, M.R. Lukatskaya, Y. Gogotsi, T.F. Jaramillo, A. Vojvodic, Two-Dimensional Molybdenum Carbide (MXene) as an Efficient Electrocatalyst for Hydrogen Evolution, ACS Energy Letters 1 (2016) 589-594.

[36] M.R. Lukatskaya, O. Mashtalir, C.E. Ren, Y. Dall'Agnese, P. Rozier, P.L. Taberna, M. Naguib, P. Simon, M.W. Barsoum, Y. Gogotsi, Cation intercalation and high volumetric capacitance of two-dimensional titanium carbide, Science 341 (2013) 1502-1505.

[37] B. Anasori, M.R. Lukatskaya, Y. Gogotsi, 2D metal carbides and nitrides (MXenes) for energy storage, Nature Reviews Materials 2 (2017).

[38] M. Naguib, O. Mashtalir, J. Carle, V. Presser, J. Lu, L. Hultman, Y. Gogotsi, M.W.J.A.n. Barsoum, Two-dimensional transition metal carbides, ACS Nano 6 (2012) 1322-1331.

[39] A. Shayesteh Zeraati, S.A. Mirkhani, P. Sun, M. Naguib, P.V. Braun, U. Sundararaj, Improved synthesis of $Ti_3C_2T_x$ MXenes resulting in exceptional electrical conductivity, high synthesis yield, and enhanced capacitance, Nanoscale 13 (2021) 3572-3580.

[40] J. Xuan, Z. Wang, Y. Chen, D. Liang, L. Cheng, X. Yang, Z. Liu, R. Ma, T. Sasaki, F.J.A.C. Geng, Organic-base-driven intercalation and delamination for the production of functionalized titanium carbide nanosheets with superior photothermal therapeutic performance, Angew. Chem. Int. Ed. Engl. 128 (2016) 14789-14794.

[41] T. Li, L. Yao, Q. Liu, J. Gu, R. Luo, J. Li, X. Yan, W. Wang, P. Liu, B. Chen, W. Zhang, W. Abbas, R. Naz, D. Zhang, Fluorine-Free Synthesis of High-Purity $Ti_3C_2T_x$ (T=OH, O) via Alkali Treatment, Angew. Chem. Int. Ed. Engl. 57 (2018) 6115-6119.

[42] X. Xiao, H. Yu, H. Jin, M. Wu, Y. Fang, J. Sun, Z. Hu, T. Li, J. Wu, L. Huang, Y. Gogotsi, J. Zhou, Salt-Templated Synthesis of 2D Metallic MoN and Other Nitrides, ACS Nano 11 (2017) 2180-2186.

[43] C. Xu, L. Wang, Z. Liu, L. Chen, J. Guo, N. Kang, X.L. Ma, H.M. Cheng, W. Ren, Large-area high-quality 2D ultrathin Mo_2C superconducting crystals, Nat Mater 14 (2015) 1135-1141.

[44] J. Jyoti, B.P. Singh, M. Sandhu, S.K. Tripathi, New insights on MXene and its advanced hybrid materials for lithium-ion batteries, Sustainable Energy & Fuels 6 (2022) 971-1013.

[45] H.T. Mathew, K. Abhisek, S.S. Vhatkar, R. Oraon, Headway towards contemporary 2D MXene-based hybrid electrodes for alkali-ion batteries, Energy Advances 1 (2022) 950-979.

[46] M. Naguib, J. Come, B. Dyatkin, V. Presser, P.-L. Taberna, P. Simon, M.W. Barsoum, Y. Gogotsi, MXene: a promising transition metal carbide anode for lithium-ion batteries, Electrochem. Commun. 16 (2012) 61-64

[47] C. Li, X. Zhang, K. Wang, X. Sun, Y. Ma, Accordion-like titanium carbide (MXene) with high crystallinity as fast intercalative anode for high-rate lithium-ion capacitors, Chin. Chem. Lett. 31 (2020) 1009-1013.

[48] H. Li, A. Li, D. Zhang, Q. Wu, P. Mao, Y. Qiu, Z. Zhao, P. Yu, X. Su, M. Bai, First-Principles Study on the Structural, Electronic, and Lithium Storage Properties of $Ti_3C_2T_2$ (T = O, F, H, OH) MXene, ACS Omega 7 (2022) 40578-40585.

[49] N. Xue, X. Li, M. Zhang, L. Han, Y. Liu, X. Tao, Chemical-Combined Ball-Milling Synthesis of Fluorine-Free Porous MXene for High-Performance Lithium Ion Batteries, ACS Applied Energy Materials 3 (2020) 10234-10241.

[50] F. Kong, X. He, Q. Liu, X. Qi, Y. Zheng, R. Wang, Y. Bai, Improving the electrochemical properties of MXene Ti_3C_2 multilayer for Li-ion batteries by vacuum calcination, Electrochim. Acta 265 (2018) 140-150.

[51] M. Lu, H. Li, W. Han, J. Chen, W. Shi, J. Wang, X.-M. Meng, J. Qi, H. Li, B. Zhang, W. Zhang, W. Zheng, 2D titanium carbide (MXene) electrodes with lower-F surface for high performance lithium-ion batteries, Journal of Energy Chemistry 31 (2019) 148-153.

[52] M. Naguib, J. Halim, J. Lu, K.M. Cook, L. Hultman, Y. Gogotsi, M.W. Barsoum, New two-dimensional niobium and vanadium carbides as promising materials for Li-ion batteries, J. Am. Chem. Soc. 135 (2013) 15966-15969.

[53] H. Aghamohammadi, R. Eslami-Farsani, E. Castillo-Martinez, Recent trends in the development of MXenes and MXene-based composites as anode materials for Li-ion batteries, Journal of Energy Storage 47 (2022).

[54] Y. Wang, Y. Li, Z. Qiu, X. Wu, P. Zhou, T. Zhou, J. Zhao, Z. Miao, J. Zhou, S. Zhuo, Fe_3O_4@Ti_3C_2 MXene hybrids with ultrahigh volumetric capacity as an anode material for lithium-ion batteries, J. Mater. Chem. A 6 (2018) 11189-11197.

[55] Z. Zhang, L. Weng, Q. Rao, S. Yang, J. Hu, J. Cai, Y. Min, Highly-dispersed iron oxide nanoparticles anchored on crumpled nitrogen-doped MXene nanosheets as anode for Li-ion batteries with enhanced cyclic and rate performance, J. Power Sources 439 (2019).

[56] J. Yao, W. Jiang, L. Pan, J. Xiong, T. Wang, T. Qiu, J. Yang, Hierarchical structure of in-situ Fe_2O_3 nanoparticles decorated on crumpled $Ti_3C_2T_x$ nanosheets with enhanced cycle performance as anode for lithium ion battery, Ceram. Int. 47 (2021) 21807-21814.

[57] A. Ali, K. Hantanasirisakul, A. Abdala, P. Urbankowski, M.Q. Zhao, B. Anasori, Y. Gogotsi, B. Aissa, K.A. Mahmoud, Effect of Synthesis on Performance of MXene/Iron Oxide Anode Material for Lithium-Ion Batteries, Langmuir 34 (2018) 11325-11334.

[58] Q. Li, J. Zhou, F. Li, Z. Sun, Spring-roll-like Ti_3C_2 MXene/carbon-coated Fe_3O_4 composite as a long-life Li-ion storage material, Inorganic Chemistry Frontiers 7 (2020) 3491-3499.

[59] M. Zheng, R. Guo, Z. Liu, B. Wang, L. Meng, F. Li, T. Li, Y. Luo, MoS_2 intercalated p-Ti_3C_2 anode materials with sandwich-like three dimensional conductive networks for lithium-ion batteries, J. Alloys Compd. 735 (2018) 1262-1270.

[60] C. Chen, X. Xie, B. Anasori, A. Sarycheva, T. Makaryan, M. Zhao, P. Urbankowski, L. Miao, J. Jiang, Y. Gogotsi, MoS_2-on-MXene Heterostructures as Highly Reversible Anode Materials for Lithium-Ion Batteries, Angew. Chem. Int. Ed. Engl. 57 (2018) 1846-1850.

[61] T. Bashir, X. Li, S. Yang, Y. Song, S. Zhou, J. Wang, W. Zhu, J. Yang, J. Zhao, L. Gao, Enhancing role of structurally integrated V_2C MXene nanosheets on silicon anode for lithium storage, J. Alloys Compd. 922 (2022).

[62] Y. Zhang, Z. Mu, J. Lai, Y. Chao, Y. Yang, P. Zhou, Y. Li, W. Yang, Z. Xia, S. Guo, MXene/Si@SiO_x@C Layer-by-Layer Superstructure with Autoadjustable Function for Superior Stable Lithium Storage, ACS Nano 13 (2019) 2167-2175.

[63] S.H. Yu, S.H. Lee, D.J. Lee, Y.E. Sung, T. Hyeon, Conversion Reaction-Based Oxide Nanomaterials for Lithium Ion Battery Anodes, Small 12 (2016) 2146-2172.

[64] D. Puthusseri, M. Wahid, S. Ogale, Conversion-type Anode Materials for Alkali-Ion Batteries: State of the Art and Possible Research Directions, ACS Omega 3 (2018) 4591-4601.

[65] Y. Lu, L. Yu, X.W. Lou, Nanostructured Conversion-type Anode Materials for Advanced Lithium-Ion Batteries, Chem 4 (2018) 972-996.

[66] Y. Xiao, M. Jiang, M. Cao, Developing WO_3 as high-performance anode material for lithium-ion batteries, Mater. Lett. 285 (2021).

[67] M. Zheng, H. Tang, Q. Hu, S. Zheng, L. Li, J. Xu, H. Pang, Tungsten-Based Materials for Lithium-Ion Batteries, Adv. Funct. Mater. 28 (2018).

[68] J. Yin, H. Cao, J. Zhang, M. Qu, Z. Zhou, Synthesis and Applications of γ-Tungsten Oxide Hierarchical Nanostructures, Crystal Growth & Design 13 (2013) 759-769.

[69] Y. Qiu, G.-L. Xu, Q. Kuang, S.-G. Sun, S. Yang, Hierarchical WO_3 flowers comprising porous single-crystalline nanoplates show enhanced lithium storage and photocatalysis, Nano Research 5 (2012) 826-832.

[70] C.M. Sim, Y.J. Hong, Y.C. Kang, Electrochemical properties of yolk-shell, hollow, and dense WO_3 particles prepared by using spray pyrolysis, ChemSusChem 6 (2013) 1320-1325.

[71] H. Tong, Y. Xu, X. Cheng, X. Zhang, S. Gao, H. Zhao, L. Huo, One-pot solvothermal synthesis of hierarchical WO_3 hollow microspheres with superior lithium ion battery anode performance, Electrochim. Acta 210 (2016) 147-154.

[72] Y. Zhang, L. Tao, C. Xie, D. Wang, Y. Zou, R. Chen, Y. Wang, C. Jia, S. Wang, Defect Engineering on Electrode Materials for Rechargeable Batteries, Adv. Mater. 32 (2020) e1905923.

[73] W. Li, P. Da, Y. Zhang, Y. Wang, X. Lin, X. Gong, G.J.A.n. Zheng, WO_3 nanoflakes for enhanced photoelectrochemical conversion, ACS Nano 8 (2014) 11770-11777.

[74] C. Di Valentin, G. Pacchioni, Spectroscopic properties of doped and defective semiconducting oxides from hybrid density functional calculations, Acc. Chem. Res. 47 (2014) 3233-3241.

[75] J. Yan, T. Wang, G. Wu, W. Dai, N. Guan, L. Li, J. Gong, Tungsten oxide single crystal nanosheets for enhanced multichannel solar light harvesting, Adv. Mater. 27 (2015) 1580-1586.

[76] Y. Sun, W. Wang, J. Qin, D. Zhao, B. Mao, Y. Xiao, M. Cao, Oxygen vacancy-rich mesoporous $W_{18}O_{49}$ nanobelts with ultrahigh initial Coulombic efficiency toward high-performance lithium storage, Electrochim. Acta 187 (2016) 329-339.

[77] F. Zeng, Y. Ren, L. Chen, Y. Yang, Q. Li, G. Gu, Hierarchical sandwich-type tungsten trioxide nanoplates/graphene anode for high-performance lithium-ion batteries with long cycle life, Electrochim. Acta 190 (2016) 964-971.

[78] X. Gu, F. Wu, B. Lei, J. Wang, Z. Chen, K. Xie, Y. Song, D. Sun, L. Sun, H. Zhou, F. Fang, Three-dimensional nitrogen-doped graphene frameworks anchored with bamboo-like tungsten

oxide nanorods as high performance anode materials for lithium ion batteries, J. Power Sources 320 (2016) 231-238.

[79] S.K. Park, H.J. Lee, M.H. Lee, H.S. Park, Hierarchically structured reduced graphene oxide/WO_3 frameworks for an application into lithium ion battery anodes, Chem. Eng. J. 281 (2015) 724-729.

[80] K. Tang, S.A. Farooqi, X. Wang, C. Yan, Recent Progress on Molybdenum Oxides for Rechargeable Batteries, ChemSusChem. 12 (2019) 755-771.

[81] G.S. Zakharova, C. Schmidt, A. Ottmann, E. Mijowska, R. Klingeler, Microwave-assisted hydrothermal synthesis and electrochemical studies of α- and h-MoO_3, J. Solid State Electrochem. 22 (2018) 3651-3661.

[82] Q. Xia, H. Zhao, Z. Du, J. Wang, T. Zhang, J. Wang, P. Lv, Synthesis and electrochemical properties of MoO_3/C composite as anode material for lithium-ion batteries, J. Power Sources 226 (2013) 107-111.

[83] R. Nadimicherla, R. Zha, L. Wei, X. Guo, Single crystalline flowerlike α-MoO_3 nanorods and their application as anode material for lithium-ion batteries, J. Alloys Compd. 687 (2016) 79-86.

[84] H. Zhang, X. Liu, R. Wang, R. Mi, S. Li, Y. Cui, Y. Deng, J. Mei, H. Liu, Coating of α-MoO_3 on nitrogen-doped carbon nanotubes by electrodeposition as a high-performance cathode material for lithium-ion batteries, J. Power Sources 274 (2015) 1063-1069.

[85] G. Xia, D. Liu, F. Zheng, Y. Yang, J. Su, Q. Chen, Preparation of porous MoO_2@C nano-octahedrons from a polyoxometalate-based metal–organic framework for highly reversible lithium storage, J. Mater. Chem. A 4 (2016) 12434-12441.

[86] B. Guo, X. Fang, B. Li, Y. Shi, C. Ouyang, Y.-S. Hu, Z. Wang, G.D. Stucky, L. Chen, Synthesis and Lithium Storage Mechanism of Ultrafine MoO_2 Nanorods, Chem. Mater. 24 (2012) 457-463.

[87] G.S. Zakharova, L. Singer, Z.A. Fattakhova, S. Wegener, E. Thauer, Q. Zhu, E.V. Shalaeva, R. Klingeler, MoO_2/C composites prepared by tartaric acid and glucose-assisted sol-gel processes as anode materials for lithium-ion batteries, J. Alloys Compd. 863 (2021).

[88] Y. Wang, L. Yu, X.W. Lou, Formation of Triple-Shelled Molybdenum-Polydopamine Hollow Spheres and Their Conversion into MoO_2/Carbon Composite Hollow Spheres for Lithium-Ion Batteries, Angew. Chem. Int. Ed. Engl. 55 (2016) 14668-14672.

[89] P. Zhang, L. Zou, H. Hu, M. Wang, J. Fang, Y. Lai, J. Li, 3D Hierarchical Carbon Microflowers decorated with MoO_2 Nanoparticles for lithium ion batteries, Electrochim. Acta 250 (2017) 219-227.

[90] Y. Sun, X. Hu, W. Luo, Y.J.A.n. Huang, Self-assembled hierarchical MoO_2/graphene

nanoarchitectures and their application as a high-performance anode material for lithium-ion batteries, ACS Nano 5 (2011) 7100-7107.

[91] L.C. Yang, W. Sun, Z.W. Zhong, J.W. Liu, Q.S. Gao, R.Z. Hu, M. Zhu, Hierarchical MoO_2/N-doped carbon heteronanowires with high rate and improved long-term performance for lithium-ion batteries, J. Power Sources 306 (2016) 78-84.

[92] H. Liu, D. Su, G. Wang, S.Z. Qiao, An ordered mesoporous WS_2 anode material with superior electrochemical performance for lithium ion batteries, J. Mater. Chem. 22 (2012).

[93] I. Kim, S.-W. Park, D.-W. Kim, Onion-like crystalline WS_2 nanoparticles anchored on graphene sheets as high-performance anode materials for lithium-ion batteries, Chem. Eng. J. 375 (2019).

[94] Y. Wang, D. Kong, W. Shi, B. Liu, G.J. Sim, Q. Ge, H.Y. Yang, Ice Templated Free-Standing Hierarchically WS_2/CNT-rGO Aerogel for High-Performance Rechargeable Lithium and Sodium Ion Batteries, Advanced Energy Materials 6 (2016).

[95] L. Zhang, W. Fan, T. Liu, Flexible hierarchical membranes of WS_2 nanosheets grown on graphene-wrapped electrospun carbon nanofibers as advanced anodes for highly reversible lithium storage, Nanoscale 8 (2016) 16387-16394.

[96] C.G. Pope, X-ray diffraction and the Bragg equation, J. Chem. Educ. 74 (1997) 129.

[97] Clarke, A. R. (2002) Microscopy techniques for materials science. CRC Press (electronic resource)

[98] Egerton, R. F. (2005) Physical principles of electron microscopy: an introduction to TEM, SEM, and AEM. Springer, 202.

[99] F.A. Stevie, C.L. Donley, Introduction to x-ray photoelectron spectroscopy, J. Vac. Sci. Technol., A 38 (2020).

[100] T. Kim, W. Choi, H.-C. Shin, J.-Y. Choi, J.M. Kim, M.-S. Park, W.-S. Yoon, Applications of Voltammetry in Lithium Ion Battery Research, J. Electro-chem. Sci. Technol. 11 (2020) 14-25.

[101] C. Liu, M. Wu, Y. Liu, Z. Lu, Y. Yang, S. Shi, G. Yang, Effect of ball milling conditions on microstructure and lithium storage properties of $LiNi_{0.5}Mn_{1.5}O_4$ as cathode for lithium-ion batteries, Mater. Res. Bull. 99 (2018) 436-443.

[102] C. Henriksen, J.K. Mathiesen, D.B. Ravnsbæk, Improving capacity and rate capability of Li-ion cathode materials through ball milling and carbon coating – Best practice for research purposes, Solid State Ionics 344 (2020).

[103] H. Liu, S. Zhang, Q. Zhu, B. Cao, P. Zhang, N. Sun, B. Xu, F. Wu, R. Chen, Fluffy carbon-coated red phosphorus as a highly stable and high-rate anode for lithium-ion batteries, J. Mater. Chem. A 7 (2019) 11205-11213.

[104] S. Fang, D. Bresser, S. Passerini, Transition Metal Oxide Anodes for Electrochemical Energy Storage in Lithium- and Sodium-Ion Batteries, Adv. Energy Mater. 10 (2019).

[105] L. Kong, Y. Liu, H. Huang, M. Liu, W. Xu, B. Li, X.-H. Bu, Interconnected CoS_2/NC-CNTs network as high-performance anode materials for lithium-ion batteries, Science China Materials 64 (2020) 820-829.

[106] T. Stephenson, Z. Li, B. Olsen, D. Mitlin, Lithium ion battery applications of molybdenum disulfide (MoS_2) nanocomposites, Energy Environ. Sci. 7 (2014) 209-231.

[107] X. Xu, Y. Zhou, H. You, H. Min, X. Wu, W. Zang, J. Hao, Z. Feng, X. Liu, H. Yang, Engineering nano-NiS_2 embedded in graphitized carbon skeleton in hollow spherical structure as stable anode material for reversible Li^+ storage, Appl. Surf. Sci. 605 (2022).

[108] D. Ma, Z. Cao, A. Hu, Si-Based Anode Materials for Li-Ion Batteries: A Mini Review, Nanomicro Lett 6 (2014) 347-358.

[109] Z. Yu, H. Jiang, D. Gu, J. Li, L. Wang, L. Shen, A New Way to Prepare MoO_3/C as Anode of Lithium ion Battery for Enhancing the Electrochemical Performance at Room Temperature, J. Electrochemical Science and Technology 7 (2016) 170-178.

[110] M.F. Hassan, Z.P. Guo, Z. Chen, H.K. Liu, Carbon-coated MoO_3 nanobelts as anode materials for lithium-ion batteries, J. Power Sources 195 (2010) 2372-2376.

[111] Q. Tang, Z. Shan, L. Wang, X. Qin, MoO_2–graphene nanocomposite as anode material for lithium-ion batteries, Electrochim. Acta 79 (2012) 148-153.

[112] L. Zhou, H.B. Wu, Z. Wang, X.W. Lou, Interconnected MoO_2 nanocrystals with carbon nanocoating as high-capacity anode materials for lithium-ion batteries, ACS Appl Mater Interfaces 3 (2011) 4853-4857.

[113] L.A. Riley, S.-H. Lee, L. Gedvilias, A.C. Dillon, Optimization of MoO_3 nanoparticles as negative-electrode material in high-energy lithium ion batteries, J. Power Sources 195 (2010) 588-592.

[114] C.-L. Liu, Y. Wang, C. Zhang, X.-S. Li, W.-S. Dong, In situ synthesis of α-MoO_3/graphene composites as anode materials for lithium ion battery, Mater. Chem. Phys. 143 (2014) 1111-1118.

[115] Y. Zhou, Q. Liu, D. Liu, H. Xie, G. Wu, W. Huang, Y. Tian, Q. He, A. Khalil, Y.A. Haleem, T. Xiang, W. Chu, C. Zou, L. Song, Carbon-coated MoO_2 dispersed in three-dimensional graphene aerogel for lithium-ion battery, Electrochim. Acta 174 (2015) 8-14

[116] A. Bhaskar, M. Deepa, T. Narasinga Rao, MoO_2/multiwalled carbon nanotubes (MWCNT) hybrid for use as a Li-ion battery anode, ACS Appl Mater Interfaces 5 (2013) 2555-2566.

[117] K. Palanisamy, Y. Kim, H. Kim, J.M. Kim, W.-S. Yoon, Self-assembled porous MoO_2/graphene microspheres towards high performance anodes for lithium ion batteries, J. Power Sources 275 (2015) 351-361.

[118] S.H. Choi, Y.C. Kang, Crumpled graphene-molybdenum oxide composite powders: preparation and application in lithium-ion batteries, ChemSusChem 7 (2014) 523-528

[119] J. Pang, R.G. Mendes, A. Bachmatiuk, L. Zhao, H.Q. Ta, T. Gemming, H. Liu, Z. Liu, M.H. Rummeli, Applications of 2D MXenes in energy conversion and storage systems, Chem. Soc. Rev. 48 (2019) 72-133.

[120] V.M. Hong Ng, H. Huang, K. Zhou, P.S. Lee, W. Que, J.Z. Xu, L.B. Kong, Recent progress in layered transition metal carbides and/or nitrides (MXenes) and their composites: synthesis and applications, J. Mater. Chem. A 5 (2017) 3039-3068.

[121] D. Xiong, X. Li, Z. Bai, S. Lu, Recent Advances in Layered $Ti_3C_2T_x$ MXene for Electrochemical Energy Storage, Small 14 (2018) e1703419.

[122] B.-M. Jun, S. Kim, J. Heo, C.M. Park, N. Her, M. Jang, Y. Huang, J. Han, Y. Yoon, Review of MXenes as new nanomaterials for energy storage/delivery and selected environmental applications, Nano Research 12 (2018) 471-487.

[123] X. Tang, X. Guo, W. Wu, G. Wang, 2D Metal Carbides and Nitrides (MXenes) as High‐Performance Electrode Materials for Lithium‐Based Batteries, Adv. Energy Mater. 8 (2018).

[124] J. Ai, Y. Lei, S. Yang, C. Lai, Q. Xu, SnS nanoparticles anchored on Ti_3C_2 nanosheets matrix via electrostatic attraction method as novel anode for lithium ion batteries, Chem. Eng. J. 357 (2019) 150-158.

[125] Felix Lulay, MXene as Novel Anode Materials for Li-ion Batteries, Report (2020).

[126] E. Wu, J. Wang, H. Zhang, Y. Zhou, K. Sun, Y. Xue, Neutron diffraction studies of $Ti_3Si_{0.9}Al_{0.1}C_2$ compound, Mater. Lett. 59 (2005) 2715-2719.

[127] Y. Wei, P. Zhang, R.A. Soomro, Q. Zhu, B. Xu, Advances in the Synthesis of 2D MXenes, Adv. Mater. 33 (2021) e2103148.

[128] M. Alhabeb, K. Maleski, B. Anasori, P. Lelyukh, L. Clark, S. Sin, Y. Gogotsi, Guidelines for Synthesis and Processing of Two-Dimensional Titanium Carbide ($Ti_3C_2T_x$ MXene), Chem. Mater. 29 (2017) 7633-7644

[129] A. Feng, Y. Yu, F. Jiang, Y. Wang, L. Mi, Y. Yu, L. Song, Fabrication and thermal stability of NH_4HF_2-etched Ti_3C_2 MXene, Ceram. Int. 43 (2017) 6322-6328.

[130] C. Lu, L. Yang, B. Yan, L. Sun, P. Zhang, W. Zhang, Z. Sun, Nitrogen-Doped Ti_3C_2 MXene: Mechanism Investigation and Electrochemical Analysis, Adv. Funct. Mater. 30 (2020).

[131] L. Huang, T. Li, Q. Liu, J. Gu, Fluorine-free $Ti_3C_2T_x$ as anode materials for Li-ion batteries, Electrochem. Commun. 104 (2019).

[132] D. Sun, M. Wang, Z. Li, G. Fan, L.-Z. Fan, A. Zhou, Two-dimensional Ti_3C_2 as anode material for Li-ion batteries, Electrochem. Commun. 47 (2014) 80-83.

[133] J. Schuster, H. Nowotny, C. Vaccaro, The ternary systems: CrAlC, VAlC, and TiAlC and the behavior of H-phases (M_2AlC), J. Solid State Chem. 32 (1980) 213-219.

[134] A. Tyagi, J. Köhler, Preparation and rietveld refinement of the structure of β-Li_3AlF_6, Mater. Res. Bull. 32 (1997) 1683-1689.

[135] A. Garg, A. Goel, S. Prasher, R. Kumar, R. Moulick, MXene nanocomposites for microwave absorption, Journal of Physics: Conference Series 2267 (2022).

[136] Q. Tang, Z. Zhou, P. Shen, Are MXenes promising anode materials for Li ion batteries? Computational studies on electronic properties and Li storage capability of Ti_3C_2 and $Ti_3C_2X_2$ (X = F, OH) monolayer, J. Am. Chem. Soc. 134 (2012) 16909-16916.

[137] Y. Xie, M. Naguib, V.N. Mochalin, M.W. Barsoum, Y. Gogotsi, X. Yu, K.W. Nam, X.Q. Yang, A.I. Kolesnikov, P.R. Kent, Role of surface structure on Li-ion energy storage capacity of two-dimensional transition-metal carbides, J. Am. Chem. Soc. 136 (2014) 6385-6394.

[138] Yannis Riedel, Investigation of TMO/MXene nanocomposite via a ball-milling method as anode material in Lithium-ion batteries, Bachelor Thesis (2021).

[139] R. Cheng, T. Hu, Z. Wang, J. Yang, R. Dai, W. Wang, C. Cui, Y. Liang, C. Zhang, C. Li, H. Wang, H. Lu, Z. Yang, H. Zhang, X. Wang, Understanding charge storage in Nb_2CT_x MXene as an anode material for lithium ion batteries, Phys. Chem. Chem. Phys. 23 (2021) 23173-23183.

[140] M.C. Liu, B.M. Zhang, Y.S. Zhang, D.T. Zhang, C.Y. Tian, L.B. Kong, Y.X. Hu, Interlayer Engineering Construction of 2D Nb_2CT_x with Enlarged Interlayer Spacing Towards High Capacity and Rate Capability for Lithium ‐ Ion Storage, Batteries & Supercaps 4 (2021) 1473-1481.

[141] O. Mashtalir, M.R. Lukatskaya, M.Q. Zhao, M.W. Barsoum, Y. Gogotsi, Amine-Assisted Delamination of Nb_2C MXene for Li-Ion Energy Storage Devices, Adv. Mater. 27 (2015) 3501-3506.

[142] D.D. Sun, Q.K. Hu, J.F. Chen, A.G. Zhou, First Principles Calculations of the Relative Stability, Structure and Electronic Properties of Two Dimensional Metal Carbides and Nitrides, Key Eng. Mater. 602-603 (2014) 527-531.

[143] F. Liu, J. Zhou, S. Wang, B. Wang, C. Shen, L. Wang, Q. Hu, Q. Huang, A. Zhou, Preparation of High-Purity V_2C MXene and Electrochemical Properties as Li-Ion Batteries, J. Electrochem. Soc. 164 (2017) A709-A713.

[144] H. Sitepu, Texture and structural refinement using neutron diffraction data from molybdite (MoO_3) and calcite ($CaCO_3$) powders and a Ni-rich $Ni_{50.7}Ti_{49.30}$ alloy, Powder Diffr. 24 (2009) 315-326.

[145] X. Cheng, Y. Li, L. Sang, J. Ma, H. Shi, X. Liu, J. Lu, Y. Zhang, Boosting the electrochemical performance of MoO_3 anode for long-life lithium ion batteries: Dominated by an ultrathin TiO_2 passivation layer, Electrochim. Acta 269 (2018) 241-249.

[146] G.D. Park, J.H. Kim, Y.J. Choi, Y.C. Kang, Large-Scale Production of MoO_3-Reduced Graphene Oxide Powders with Superior Lithium Storage Properties by Spray-Drying Process, Electrochim. Acta 173 (2015) 581-587.

[147] W. Wang, J. Qin, Z. Yin, M. Cao, Achieving Fully Reversible Conversion in MoO_3 for Lithium Ion Batteries by Rational Introduction of $CoMoO_4$, ACS Nano 10 (2016) 10106-10116.

[148] T. Herdt, M. Bruns, J.J. Schneider, A 3D MoO_x/carbon composite array as a binder-free anode in lithium-ion batteries, Dalton Trans 47 (2018) 14897-14907.

[149] Y.S. Jung, S. Lee, D. Ahn, A.C. Dillon, S.-H. Lee, Electrochemical reactivity of ball-milled MoO_{3-y} as anode materials for lithium-ion batteries, J. Power Sources 188 (2009) 286-291

[150] O. Delmer, P. Balaya, L. Kienle, J. Maier, Enhanced Potential of Amorphous Electrode Materials: Case Study of RuO_2, Adv. Mater. 20 (2008) 501-505.

[151] Brian Hinz, Investigation of MoO_x/MXene and WO_x/MXene composites as anode material for lithium-ion batteries, Bachelor Thesis (2022).

[152] G. Liu, T. Zhang, X. Li, J. Li, N. Wu, A. Cao, W. Yuan, K. Pan, D. Guo, X. Liu, MoS_2@C with S vacancies vertically anchored on V_2C-MXene for efficient lithium and sodium storage, Inorganic Chemistry Frontiers 10 (2023) 1587-1602.

[153] A.A. Bolzan, B.J. Kennedy, C.J. Howard, Neutron powder diffraction study of molybdenum and tungsten dioxides, Aust. J. Chem. 48 (1995) 1473-1477.

[154] M. Ghedira, H. Vincent, M. Marezio, J. Marcus, G. Furcaudot, Structure cristalline du conducteur metallique bidimensionnel Mo_4O_{11}-γ, J. Solid State Chem. 56 (1985) 66-73.

[155] J. Guo, P. Zavalij, M.S. Whittingham, Metastable hexagonal molybdates: hydrothermal preparation, structure, and reactivity, J. Solid State Chem. 117 (1995) 323-332.

[156] P. Xiong, R. Ma, N. Sakai, T. Sasaki, Genuine Unilamellar Metal Oxide Nanosheets Confined in a Superlattice-like Structure for Superior Energy Storage, ACS Nano 12 (2018) 1768-1777.

[157] H. Xu, L. Yang, Amorphous MoO_2/C Nanospheres–Porous Graphene Composites for Pseudocapacitive Li Storage, ACS Applied Nano Materials 5 (2022) 13463-13472.

[158] S. Petnikota, K.W. Teo, L. Chen, A. Sim, S.K. Marka, M.V. Reddy, V.V. Srikanth, S. Adams, B.V. Chowdari, Exfoliated Graphene Oxide/MoO_2 Composites as Anode Materials in Lithium-Ion Batteries: An Insight into Intercalation of Li and Conversion Mechanism of MoO_2, ACS Appl Mater Interfaces 8 (2016) 10884-10896.

[159] K. Palanisamy, Y. Kim, H. Kim, J.M. Kim, W.-S. Yoon, Self-assembled porous MoO_2/graphene microspheres towards high performance anodes for lithium ion batteries, J. Power Sources 275 (2015) 351-361.

[160] Y. Wang, Z. Huang, Y. Wang, A new approach to synthesize MoO_2@C for high-rate lithium ion batteries, J. Mater. Chem. A 3 (2015) 21314-21320.

[161] W. Tang, C.X. Peng, C.T. Nai, J. Su, Y.P. Liu, M.V. Reddy, M. Lin, K.P. Loh, Ultrahigh Capacity Due to Multi-Electron Conversion Reaction in Reduced Graphene Oxide-Wrapped MoO_2 Porous Nanobelts, Small 11 (2015) 2446-2453.

[162] H. Tang, R. Guo, M. Jiang, Y. Zhang, X. Lai, C. Cui, H. Xiao, S. Jiang, E. Ren, Q. Qin, Construction of Ti_3C_2 MXene@C@SnS with layered rock stratum structure for high-performance lithium storage, J. Power Sources 462 (2020).

[163] P. Guo, L. Singer, Z. Zhao, W. Kukułka, F. Sebastian, E. Mijowska, M. Zharnikov, P. Comba, R. Klingeler, A facile preparation method and proof of cycle-stability of carbon-coated metal oxide and disulfide battery materials, Electrochim. Acta (2023).

[164] P. Li, X. Li, Z. Zhao, M. Wang, T. Fox, Q. Zhang, Y. Zhou, Correlations among structure, composition and electrochemical performances of WO_3 anode materials for lithium ion batteries, Electrochim. Acta 192 (2016) 148-157.

[165] J. Ren, R.-P. Ren, Y.-K. Lv, WS_2-decorated graphene foam@CNTs hybrid anode for enhanced lithium-ion storage, J. Alloys Compd. 784 (2019) 697-703.

[166] J. Ren, Z. Wang, F. Yang, R.-P. Ren, Y.-K. Lv, Freestanding 3D single-wall carbon nanotubes/WS_2 nanosheets foams as ultra-long-life anodes for rechargeable lithium ion batteries, Electrochim. Acta 267 (2018) 133-140.

[167] H. Xu, L. Sun, W. Li, M. Gao, Q. Zhou, P. Li, S. Yang, J. Lin, Facile synthesis of hierarchical g-C_3N_4@WS_2 composite as Lithium-ion battery anode, Chem. Eng. J. 435 (2022).

[168] J. Yang, S. Du, L. Ao, J. Zhang, C. Jin, M. Han, K. Jiang, L. Shang, Y. Li, J. Zhang, L. Zhu, Z. Hu, J. Chu, Embedded Double One - Dimensional Composites of WO_3@N - Doped Carbon Nanofibers for Superior and Stabilized Lithium Storage, ChemElectroChem 9 (2022).

[169] X. Yu, C. Pei, W. Chen, L. Feng, 2 dimensional WS_2 tailored nitrogen-doped carbon nanofiber as a highly pseudocapacitive anode material for lithium-ion battery, Electrochim. Acta 272 (2018) 119-126.

[170] J. Li, X. Shi, J. Fang, J. Li, Z. Zhang, Facile Synthesis of WS_2 Nanosheets-Carbon Composites Anodes for Sodium and Lithium Ion Batteries, ChemNanoMat 2 (2016) 997-1002.

[171] W. Dang, W. Wang, Y. Yang, Y. Wang, J. Huang, X. Fang, L. Wu, Z. Rong, X. Chen, X. Li, L. Huang, X. Tang, One-step hydrothermal synthesis of 2D WO_3 nanoplates@graphene nanocomposite with superior anode performance for lithium ion battery, Electrochim. Acta 313 (2019) 99-108.

[172] K. Bao, W. Mao, G. Liu, L. Ye, H. Xie, S. Ji, D. Wang, C. Chen, Y. Li, Preparation and electrochemical characterization of ultrathin WO_{3-x} /C nanosheets as anode materials in lithium ion batteries, Nano Research 10 (2016) 1903-1911.

[173] C. Jo, W.-G. Lim, A.H. Dao, S. Kim, S. Kim, S. Yoon, J. Lee, Tracking the confinement effect of highly dispersive carbon in a tungsten oxide/carbon nanocomposite: conversion anode materials in lithium ion batteries, J. Mater. Chem. A 5 (2017) 24782-24789.

[174] K. Shiva, H.S.S. Ramakrishna Matte, H.B. Rajendra, A.J. Bhattacharyya, C.N.R. Rao, Employing synergistic interactions between few-layer WS_2 and reduced graphene oxide to improve lithium storage, cyclability and rate capability of Li-ion batteries, Nano Energy 2 (2013) 787-793.

[175] R. Chen, T. Zhao, W. Wu, F. Wu, L. Li, J. Qian, R. Xu, H. Wu, H.M. Albishri, A.S. Al-Bogami, D.A. El-Hady, J. Lu, K. Amine, Free-standing hierarchically sandwich-type tungsten disulfide nanotubes/graphene anode for lithium-ion batteries, Nano Lett 14 (2014) 5899-5904.

[176] D.H. Youn, C. Jo, J.Y. Kim, J. Lee, J.S. Lee, Ultrafast synthesis of MoS_2 or WS_2-reduced graphene oxide composites via hybrid microwave annealing for anode materials of lithium ion batteries, J. Power Sources 295 (2015) 228-234.

[177] T. Li, R. Guo, Y. Luo, F. Li, L. Meng, X. Sun, Z. Yang, H. Luo, Y. Wan, Improved lithium and sodium ion storage properties of WS_2 anode with three-layer shell structure, Electrochim. Acta 331 (2020).

[178] Y. Liu, W. Wang, Y. Wang, X. Peng, Homogeneously assembling like-charged WS_2 and GO nanosheets lamellar composite films by filtration for highly efficient lithium ion batteries, Nano Energy 7 (2014) 25-32.

[179] S. Zhou, J. Chen, L. Gan, Q. Zhang, Z. Zheng, H. Li, T. Zhai, Scalable production of self-supported WS_2/CNFs by electrospinning as the anode for high-performance lithium-ion batteries, Sci. Bull. 61 (2016) 227-235.

[180] Q. Pang, Y. Gao, Y. Zhao, Y. Ju, H. Qiu, Y. Wei, B. Liu, B. Zou, F. Du, G. Chen, Improved Lithium-Ion and Sodium-Ion Storage Properties from Few-Layered WS_2 Nanosheets Embedded in a Mesoporous CMK-3 Matrix, Chemistry 23 (2017) 7074-7080.

[181] Finn Sebastian, Investigation of WO_3 and WS_2 carbon composites as anode materials for lithium ion batteries, Research report (2021).

[182] B. Gerand, G. Nowogrocki, J. Guenot, M. Figlarz, Structural study of a new hexagonal form of tungsten trioxide, J. Solid State Chem. 29 (1979) 429-434.

[183] K. Viswanathan, K. Brandt, E. Salje, Crystal structure and charge carrier concentration of $W_{18}O_{49}$, J. Solid State Chem. 36 (1981) 45-51.

[184] W. Zhang, L. Yue, F. Zhang, Q. Zhang, X. Gui, R. Guan, G. Hou, N. Xu, One-step in situ synthesis of ultrathin tungsten oxide@carbon nanowire webs as an anode material for high performance, J. Mater. Chem. A 3 (2015) 6102-6109.

[185] B. Zhang, C. Luo, Y. Deng, Z. Huang, G. Zhou, W. Lv, Y.B. He, Y. Wan, F. Kang, Q.H. Yang, Optimized Catalytic WS_2–WO_3 Heterostructure Design for Accelerated Polysulfide Conversion in Lithium–Sulfur Batteries, Adv. Energy. Mater. 10 (2020).

[186] W. Schutte, J. De Boer, F. Jellinek, Crystal structures of tungsten disulfide and diselenide, J. Solid State Chem. 70 (1987) 207-209.

[187] L. Yin, D. Pham-Cong, I. Jeon, J.-P. Kim, J. Cho, S.-Y. Jeong, H. Woo Lee, C.-R. Cho, Electrochemical performance of vertically grown WS_2 layers on $TiNb_2O_7$ nanostructures for lithium-ion battery anodes, Chem. Eng. J. 382 (2020).

[188] C. Zhu, S. Zheng, T. Cao, C. Lin, Z. Xie, Surface oxygen vacancies induced peroxidase-like activity for $W_{18}O_{49}$ nanospheres and their application in degradation of methylene blue, J. Nanopart. Res. 20 (2018).

[189] L. Sinha, P.M. Shirage, Surface Oxygen Vacancy Formulated Energy Storage Application: Pseudocapacitor-Battery Trait of $W_{18}O_{49}$ Nanorods, J. Electrochem. Soc. 166 (2019) A3496-A3503.

[190] J. Li, H. Yan, W. Wei, X. Li, L. Meng, Enhanced Lithium Storage Performance of Liquid-Phase Exfoliated Graphene Supported WS_2 Heterojunctions, ChemElectroChem 5 (2018) 3222-3228.

[191] Z. Chen, K. Ye, M. Li, S. Zhao, J. Luo, B. Wu, Lithiation mechanism of $W_{18}O_{49}$ anode material for lithium-ion batteries: Experiment and first-principles calculations, J. Electroanal. Chem. 880 (2021).

[192] S. Liu, B. Shen, Y. Niu, M. Xu, Fabrication of WS_2-nanoflowers@rGO composite as an anode material for enhanced electrode performance in lithium-ion batteries, J. Colloid Interface Sci. 488 (2017) 20-25.

[193] H.T. Huu, H.T.T. Le, V.P. Nguyen, T.T. Huong Nguyen, T.X. Dieu Nguyen, V.T. Nguyen, S.-J. Kim, V. Vo, Facile one-step synthesis of g–C_3N_4–supported WS_2 with enhanced lithium storage properties, Electrochim. Acta 341 (2020).

[194] W. Sun, Z. Hu, C. Wang, Z. Tao, S.L. Chou, Y.M. Kang, H.K. Liu, Effects of Carbon Content on the Electrochemical Performances of MoS_2-C Nanocomposites for Li-Ion Batteries, ACS Appl Mater Interfaces 8 (2016) 22168-22174.

[195] X.L. Xu, Y. Chen, S.Y. Ma, S.H. Yan, Y.Z. Mao, T. Wang, H.Q. Bian, CTAB-assisted synthesis of unique 3D ZnO and the acetone sensing performances, Mater. Lett. 151 (2015) 5-8.

[196] J. Li, L. Han, Y. Li, J. Li, G. Zhu, X. Zhang, T. Lu, L. Pan, MXene-decorated SnS_2/Sn_3S_4 hybrid as anode material for high-rate lithium-ion batteries, Chem. Eng. J. 380 (2020).

[197] H. Liu, X. Zhang, Y. Zhu, B. Cao, Q. Zhu, P. Zhang, B. Xu, F. Wu, R. Chen, Electrostatic Self-assembly of 0D-2D SnO_2 Quantum Dots/Ti_3C_2Tx MXene Hybrids as Anode for Lithium-Ion Batteries, Nanomicro Lett 11 (2019) 65.

[198] S. Yoon, S.-G. Woo, K.-N. Jung, H. Song, Conductive surface modification of cauliflower-like WO_3 and its electrochemical properties for lithium-ion batteries, J. Alloys Compd. 613 (2014) 187-192.

[199] Y. Dong, S. Chen, J. Liu, J. Lei, F. Liu, W. Yang, J. Wang, Polygonal WS_2-decorated-graphene multilayer films with microcavities prepared from a cheap precursor as anode materials for lithium-ion batteries, Mater. Lett. 254 (2019) 73-76.

[200] J. Huang, X. Wang, J. Li, L. Cao, Z. Xu, H. Wei, WS_2-Super P nanocomposites anode material with enhanced cycling stability for lithium ion batteries, J. Alloys Compd. 673 (2016) 60-66.

[201] X. Li, J. Zhang, Z. Liu, C. Fu, C. Niu, WS_2 nanoflowers on carbon nanotube vines with enhanced electrochemical performances for lithium and sodium-ion batteries, J. Alloys Compd. 766 (2018) 656-662.

[202] J. Li, X. Shi, J. Fang, J. Li, Z. Zhang, Facile Synthesis of WS_2 Nanosheets-Carbon Composites Anodes for Sodium and Lithium Ion Batteries, ChemNanoMat 2 (2016) 997-1002.

GESAMTFAKULTÄT FÜR MATHEMATIK, INGENIEUR- UND NATURWISSENSCHAFTEN

COMBINED FACULTY OF MATHEMATICS, ENGINEERING AND NATURAL SCIENCES

RUPRECHT-KARLS-
UNIVERSITÄT
HEIDELBERG

Eidesstattliche Versicherung gemäß § 8 der Promotionsordnung für die Gesamtfakultät für Mathematik, Ingenieur- und Naturwissenschaften der Universität Heidelberg /
Sworn Affidavit according to § 8 of the doctoral degree regulations of the Combined Faculty of Mathematics, Engineering and Natural Sciences at Heidelberg University

1. Bei der eingereichten Dissertation zu dem Thema / The thesis I have submitted entitled

   Advanced Transition Metal-Based Anode Materials and their Composites for Lithium Ion Battery Application
   ………

   ………

   handelt es sich um meine eigenständig erbrachte Leistung / is my own work.

2. Ich habe nur die angegebenen Quellen und Hilfsmittel benutzt und mich keiner unzulässigen Hilfe Dritter bedient. Insbesondere habe ich wörtlich oder sinngemäß aus anderen Werken übernommene Inhalte als solche kenntlich gemacht. / I have only used the sources indicated and have not made unauthorised use of services of a third party. Where the work of others has been quoted or reproduced, the source is always given.

3. Die Arbeit oder Teile davon habe ich wie folgt/bislang nicht[1)] an einer Hochschule des In- oder Auslands als Bestandteil einer Prüfungs- oder Qualifikationsleistung vorgelegt. / I have not yet/~~have already~~[1)] presented this thesis or parts thereof to a university as part of an examination or degree.

   Titel der Arbeit / Title of the thesis: ……………………………………………………………………………

   Hochschule und Jahr / University and year: …………………..…………………………………………......

   Art der Prüfungs- oder Qualifikationsleistung / Type of examination or degree: …………………………

4. Die Richtigkeit der vorstehenden Erklärungen bestätige ich. / I confirm that the declarations made above are correct.

5. Die Bedeutung der eidesstattlichen Versicherung und die strafrechtlichen Folgen einer unrichtigen oder unvollständigen eidesstattlichen Versicherung sind mir bekannt. / I am aware of the importance of a sworn affidavit and the criminal prosecution in case of a false or incomplete affidavit.

Ich versichere an Eides statt, dass ich nach bestem Wissen die reine Wahrheit erklärt und nichts verschwiegen habe. / I affirm that the above is the absolute truth to the best of my knowledge and that I have not concealed anything.

……………………………………….. ……………………………..………………………..

Ort und Datum / Place and date Unterschrift / Signature

[1)] Nicht Zutreffendes streichen. Bei Bejahung sind anzugeben: der Titel der andernorts vorgelegten Arbeit, die Hochschule, das Jahr der Vorlage und die Art der Prüfungs- oder Qualifikationsleistung. / Please cross out what is not applicable. If applicable, please provide: the title of the thesis that was presented elsewhere, the name of the university, the year of presentation and the type of examination or degree.

The German text is legally binding.